TRANSLATING CLINICAL CHEMISTRY TO THE POINT-OF-CARE USING SURFACE-ENHANCED RAMAN SPECTROSCOPY

A Dissertation

by

HALEY LYNN MARKS

Submitted to the Office of Graduate and Professional Studies of
Texas A&M University
in partial fulfillment of the requirements for the degree of

DOCTOR OF PHILOSOPHY

Chair of Committee,	Gerard L. Coté
Committee Members,	Michael McShane
	Kenith Meissner
	Jun Kameoka
Head of Department,	Anthony Guiseppi-Elie

December 2016

Major Subject: Biomedical Engineering

ABSTRACT

Disease-identifying proteins, toxins and carcinogens, bacteria, viruses, cancerous cells, and many other biomarkers can all be found in the circulatory system, making the blood and other bodily fluids a diagnostic goldmine. Clinical chemistry: the analysis of bodily fluid components by pathologists, remains the most commonly used diagnostic tool, with the CDC estimating 6.8 billion various in-vitro laboratory tests performed per year by clinical pathologists. Conversely a staggering 87% of patient samples are sent to centralized laboratories. Lab-on-a-chip devices allow for low sample/reagent volumes, portability, and disposability, thereby automating sample preparation and analysis. Utilizing surface enhanced Raman spectroscopy (SERS) as the signal transduction method, ultra-low limits of detection can be achieved while also providing opportunities for high-throughput multiplexed assays.

Several SERS-on-a-chip sensor platforms were investigated, initially looking at both direct and indirect analysis of various biomarkers ranging from small molecules and single nucleotides, to labeled and unlabeled proteins. Finally, investigating deeply into the detection and isolation of non-immunogenic small molecule biomarkers from complex media, a competitive binding assay for detection of the small endocrine-disrupting toxin bisphenol-A (BPA) was developed. This assay has the potential to be translated to virtually any biomarker by utilizing aptamers: short synthetic ssDNA strands capable of binding to non-DNA targets. Specifically, this “turn off” competitive binding assay relies on aptamer-mediated assembly of SERRS active plasmonic and magnetic nanoparticles. Additionally, a magneto-fluidic SERS analysis chip for automated sample processing and quantification of BPA (0.2 pg/mL - 0.2 µg/mL) was developed. Last, this magnetic chip was attached to a blood filtration chip and the feasibility of the assay’s resilience in whole blood was analyzed.

This technology can potentially be made sensitive to other analytes by simply exchanging the aptamer - making the platform “programmable” The enablement of technologies like this help push medicine to become increasingly personalized, predictive, and preventative by moving away from initial symptom based diagnostics and towards fast, quantifiable monitoring.

DEDICATION

To Mom, Dad, and Connor, for your unconditional love and for always keeping up with my never-ending excursion that is life. Thank you all so much for all your support despite my always being so far away from home, and for every rejuvenating visit between the chaos. Your encouragement is truly what has kept me going through this process.

ACKNOWLEDGEMENTS

First I would like to thank my advisor Gerard Coté, for his guidance throughout the course of my graduate degree, and for the opportunity to explore such an engaging area of science. Thank you for the endless networking and travel opportunities that have launched my career, for your patience with my stubbornness, and for facilitating this journey which has allowed me to grow not only as a researcher but also as a teacher, a negotiator, and as a person. I am also thankful for the support and counsel of my committee members- Michael McShane, Kenith Meissner, and Jun Kameoka.

I am so very grateful for my labmates in the Optical BioSensing Lab and Biomedical Optics Laboratory, both past and present, for their friendships, guidance, the late nights brainstorming and collecting data, and for being there through all the ups and downs of grad school. I am forever indebted to my mentor Melodie Benford for teaching me to be as meticulous in lab as I am in life, for giving me the mindset of a true analyst, and for her voice in the back of my head always reminding "there is no such thing as 'bad' data." Words cannot describe my appreciation and admiration towards Andrea Locke, who is our mother hen, our rock, and without whom the lab would surely collapse.

Sláinte to all the wee cheeky 'Ramanators' in the Strathclyde group up in Glasgow, for all the laughs and without whom this work could not have been possible. Special thanks to Duncan Graham who granted me open access to his wonderland of Raman instruments, and to Sam Mabbott for the courage to accept the results I cannot change, the strength to stop planning and 'just do it', and the wisdom to know the difference. #RIPDreadnought.

Und herzlichen dank zu Dr. Wasser, ich bin inspiriert von dich!

NOMENCLATURE

BADGE	Bisphenol-A diglycidyl ether
bp	Base pair
BPA	Bisphenol-A
CDC	Center for Disease Control
CV	Coefficient of Variation
CSA	Core-satellite assembly
CSF	Cerebrospinal fluid
DLS	Dynamic light scattering
ds	Double stranded
EF	Enhancement factor
GCS	Glasgow Coma Scale
HPLC	High Performance Liquid Chromatography
IR	Infrared radiation
IVD	*In-vitro* Diagnostic
Laser	Light Amplification by Stimulated Emission of Radiation
LOC	Lab-on-a-Chip
MBA	Mercaptobenzoic acid
MGITC	Malachite green isothiocyanate
MNP	Magnetic nanoparticle
MS	Mass spectroscopy
MST	Microscale Thermophoresis

MYO	Myoglobin
NP	Nanoparticle
NSE	Neuron specific enolase
nt	Nucleotide
NTA	Nanoparticle tracking analysis
PEG	Poly(ethylene) glycol
PDMS	Polydimethylsiloxane
POC	Point-of-care
R6G	Rhodamine-6G
SEM/TEM	Scanning/transmission electron microscopy
SERRS	Surface enhanced resonance Raman scattering
SERS	Surface enhanced Raman spectroscopy
ss	Single stranded
TBI	Traumatic Brain Injury
TRITC	Tetramethylrhodamine isothiocyanate
UCH-L1	Ubiquitin carboxy-terminal hydrolase L1
UV-vis	Ultraviolet -visible spectrophotometry
WHO	World Health Organization

TABLE OF CONTENTS

Page

LIST OF FIGURES

Page

LIST OF TABLES

Page

CHAPTER I

INTRODUCTION

With the CDC estimating over 13 billion *in-vitro* diagnostic tests run annually, disease-identifying proteins, toxins and carcinogens, bacteria, viruses, cancerous cells, and many other biomarkers found in bodily fluids are analyzed using various forms of in-vitro diagnostic (IVD) testing, making them the most frequently performed medical tests in the United States.[5] Personalized patient care and preventive diagnosis revolve around a clinical chemist's understanding of each patient's unique and complex physiology, and historically this has been monitored through the through the collection and analysis of bodily fluids. Blood, urine, and sweat (BUS) are the most common biological samples though other bodily fluids provide useful insights into human physiology such as cerebral spinal fluid or sputum, but are much more difficult to obtain due to complex sample collection or required patient participation.[6]

Remarkably IVDs tests make up only 2.3% of all healthcare expenditures in the United States[7]. Yet despite their low cost and frequency of use, and despite the fact that 66% of all medical decisions are based on the result of an IVD[8], in the United States 86% of all IVDs are performed off-site at independent labs or centralized facilities[7]. Patients are typically referred to a separate location where biological samples can be collected by a phlebotomist and analyzed by a trained technician. Laboratory testing of patients in developing countries present even greater challenges due to the limited access to laboratory equipment, clean water, and consistent electricity. Patient samples are typically sent to off-site locations capable of performing such tests, which runs the risk of samples being contaminated, lost, or mislabeled [9] along the way. Many patients in remote settings are unable to return to city clinics for multiple

appointments and often never receive results, only the initial medication, further prolonging proper diagnosis and treatment [10].

I.1 Translating clinical chemistry to the point-of-care

Recent developments in point-of-care technology focus on creating rapid diagnostic testing platforms (RDTs) where patient samples can be tested and results obtained minutes after collection. The development of POC technologies that involve automated sample preparation, such as lab-on-a-chip (LOC) devices, remove the need for complex laboratories and experienced personal by automating mixing and filtration with microlfuidics[11]. While improving overall healthcare quality by bringing BUS test results to the patient's bedside, into the home, the ambulance, the field, and more, point-of-care technology can achieve and maintains the gold standard of testing set by centralized clinical chemistry laboratories [12].

As tests often must be sent to a centralized hospital or independent laboratory, getting the result to the patient can require hours or even days due to delays caused by sample preparation, assay design, and/or logistic holdups[5]. This wait is often enough to warrant the patient being treated *before* the doctor is actually able to confirm their diagnoses. A POC technology solves these problems by providing a user-friendly interface, without the need of expert technician support or complex analysis, whilst still meeting the current clinical chemistry standards for IVDs as set by the AACC.[13-14] Moving towards integrated lab-on-a-chip systems for blood, urine, and other fluid testing offers many advantages such as automated measurement, low sample and reagent volumes, minimal sample preparation, portability, disposability, and user-friendly interfaces. Point-of-care blood diagnostic sensors utilizing disposable chip platforms have already been successfully implemented for a number of

common clinical chemistry tests, for example: to quantify panels of electrolytes, metabolites, cardiac biomarkers, blood gases, and hematocrits (i-STAT[15]); to detect HIV, syphilis and other infectious diseases (mChip[16]); and to perform up to 25 blood tests with one device by combining optical light scatter, colorimetric and electrochemical methods (Ativa). However there has yet to be a fully translatable sensing methodology for detecting and isolating emerging small molecule, bacterial, viral *and* protein biomarkers. Ergo, it is proposed that a surface enhanced Raman spectroscopy nanoparticle based detection mechanism will be developed towards the realization of a universal biosensing platform.

Separation of small non-immunogenic biomarkers from larger cellular components in biological fluids is particularly critical for accuracy in *in-vitro* diagnostic testing.[17] *By developing a platform analysis chip using microfluidics, nanoparticles, and SERS, IVD results could be analysed at the patient's side, removing many of the sources of human error associated with diagnostic blood testing, such as mislabelling of samples and improper sample preparation and transportation*.[18] The implementation of an on-chip SERS analysis method could significantly enhance a number of developing POC devices for a variety of applications such as remote and emergency health monitoring, pharmaceutical testing, or medical and academic research.

To facilitate the translation of IVDs to the point-of-care, the investigated SERS technologies should ideally be accurate, portable, simple to use, easy to read a positive or negative result, require little or no sample preparation, provide timely results, and be cost-effective.[19] The World Health Organization (WHO) has specifically defined the criteria defining a POC device in the form of an easy to remember acronym: ASSURED[20] as defined in Table 1.

Table 1. ASSURED criteria set by the WHO for classification of POC devices.

Affordable	Cost of test 1-2 day salary for developed world <$0.10 for developing countries
Sensitive	Low false negatives/high true positive rate Ensures patients not infected are not treated
Specific	Low false positives/high true positive rate Identifies only patients needing treatment
User friendly	User friendly, easy to use, requires only a few simple steps and minimal operator training
Rapid & **R**obust	Result time ~30 min, reagent shelf life >1 year → diagnose & treat in same day
Equipment-free	Equipment-free, little user input required, compact, battery powered unit, readily transportable
Deliverable	Deliverable where needed, portable, hand-held, cloud-enabled, few consumables, little waste

I.2 What is Raman scattering?

Raman scattering techniques have emerged as a unique tool in the development of blood biomarker assays as they provide characteristic chemical fingerprints, low limits of detection and capability for multiplexing due to narrow spectral band widths[21]. A number of electromagnetic interactions can occur when a biological sample is hit with an incident excitation source, the most common being elastic Rayleigh scattering (Figure 1).[22] However the Raman signal stems from the *inelastic* scattering of photons caused by a loss or gain in the incident photon's energy due to vibrations of a molecule's electric cloud. These inelastic scattered photons exhibit this shift (for Stokes Raman, gain for anti-Stokes) in energy as a result of a shift in the molecules dipole moment, where each 'Raman shifted' frequency returned is related to the polarizability of the molecule probed and the chemical structure of the molecule. Each vibrational mode corresponds to a recorded peak in the Raman spectra and can be matched to a specific bond, thereby providing an incredibly specific chemical fingerprint of the analyte. Only about 1 in 10^8 incident photons undergoes spontaneous Raman

scattering, consequently causing the technique's intrinsically weak signal. Strong Raman bands are attributed to Raman reporter molecules (RRMs) with a high Raman cross-section, meaning the molecule's electron cloud is easily distorted by the excitation laser and thus is highly polarizable.[23-24]

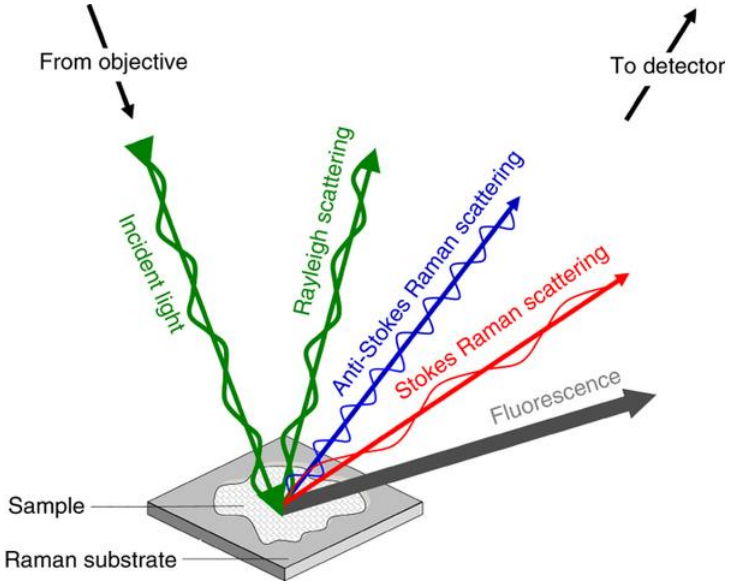

Figure 1. Schematic identifying light scattering after laser exposure on a sample surface. Reprinted with permission from Butler et al.[22] Copyright 2016 Nature Publishing Group.

I.2.i Colloidal surface enhanced Raman spectroscopy (SERS)

In surface enhanced Raman spectroscopy (SERS) extreme electromagnetic enhancements are observed when the analyte is in close proximity to a plasmonic surface such as metallic colloidal nanoparticles.[25-28] In colloidal SERS, the incident Raman excitation laser is used to generate an electric field at the dielectric interface between the particle and surrounding medium, leading to signal enhancements of up to 10^{11} when the analyte is sandwiched within 1 nm of two gold spherical particles[29-30]. Nevertheless, SERS techniques often lack reproducibility and specificity due to the random nature of particle aggregation and

the adsorption of molecules onto the metal surface[26], making it difficult to obtain quantitative information. The integration of SERS detection with biomolecular assays has been recently implemented through the design of SERS nanoprobes: metallic nanoparticles conjugated to molecules with specific optical and biochemical functionalities[31-33].

The plasmonic nano-rough structures required to facilitate SERS can be synthesized using a variety of complex photolithographic techniques borrowed from the silicon wafer industry, however colloidal plasmonic nanoparticles are arguably the simplest SERS substrate to fabricate without the need for any complex equipment or extensive training. Starting from the 1980s onward colloidal nanoparticle suspensions have served as one of the most popular SERS substrates to date, due to their relatively basic synthesis process requiring only a silver salt and a reducing agent to produce a metallic sol, with submicromolar detection limits first demonstrated by Lee and Meisel using silver nanoparticles and carbocyanine dyes in 1982 [34]. In this work they also observed the extra enhancements achievable when combining SERS with resonance Raman (SERRS). Not long after in 1989, Rohr, Cotton, et al. revealed the first SERRS immunoassay capable of monitoring antibody/antigen interactions for the biomarker human thyroid stimulating hormone (TSH) [35]. Their one-step, no wash, sandwich-type assay used a resonant dye to indirectly monitor TSH in the physiological range, thus validating the potential of SERS to enhance and improve diagnostic assays. A decade and a half later, Nie and Emory were famously able to achieve SERRS enhancements of up to 10^{15} when probing individual rhodamine 6G molecules on single silver nanoparticles [36], thus inviting future investigators to utilize this technique for point-of-care applications requiring ultra-low limits of detection.

I.3 System requirements for facilitating colloidal SERS

Colloidal SERS is most commonly achieved using silver and/or gold nanoparticles between 20-200 nm, as they exhibit unique and tunable optical properties to facilitate the plasmonic coupling event required in SERS sensing. The nanoparticle size [37], shape [38], dispersant [39], and particularly the dielectric properties of the metal all strongly effect a colloid's extinction spectra and SERS capabilities. To ensure a colloid's SERS enhancement factor is uniform throughout the suspension, it is also required that the nanoparticles be somewhat monodisperse (PDI < 0.300) [40]. Spheroids exhibit LSPRs that are typically within a ± 120 nm window of the most commonly used laser sources: 532 nm, 633 nm, and 785 nm (Figure 2).[31]

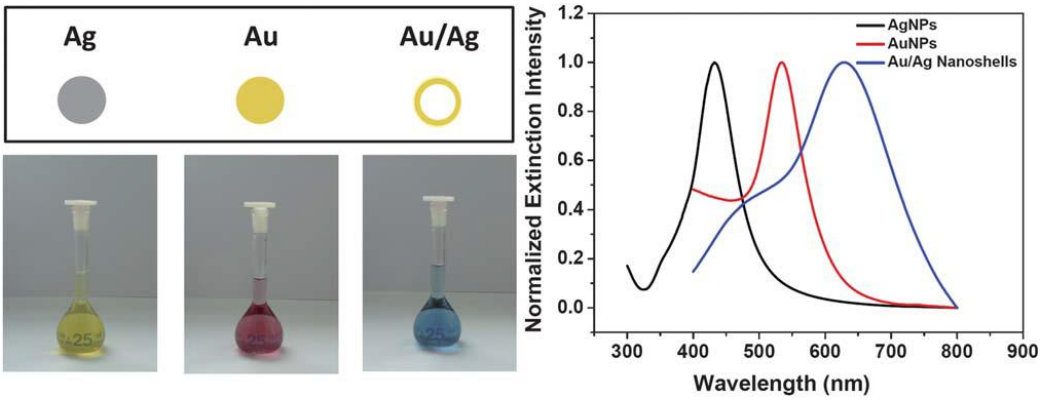

Figure 2. Photographs (left) and extinction spectra (right) of various 60 nm metal nanoparticles (AgNPs, AuNPs and Au/Ag nanoshells) in water. LSPR peaks are observed at 430 nm, 540 nm and 630 nm, respectively. Reprinted with permission from Wang et al.[31] Copyright 2013 Royal Society of Chemistry.

Maximal SERS enhancements are achieved by tuning the Raman excitation wavelength close to the intrinsic LSPR peak of the colloid, or by causing the colloid's LSPR to shift even closer into resonance with the laser by altering the particles surface interactions or aggregation state. This is commonly realized using controlled salt-based aggregation, mechanical trapping

or centrifuging of particles, or a binding event that results in nanoparticle assembly formation, for example using DNA hybridization to template core-satellite formation as described extensively by Mirkin and colleagues [41-43]. From the extinction profiles and electric field intensity models derived from their work as shown in Figure 3, it can be seen that the precise control of nanoparticle cluster formation can serve as a foundation for on/off parameters for SERS sensing.[44]

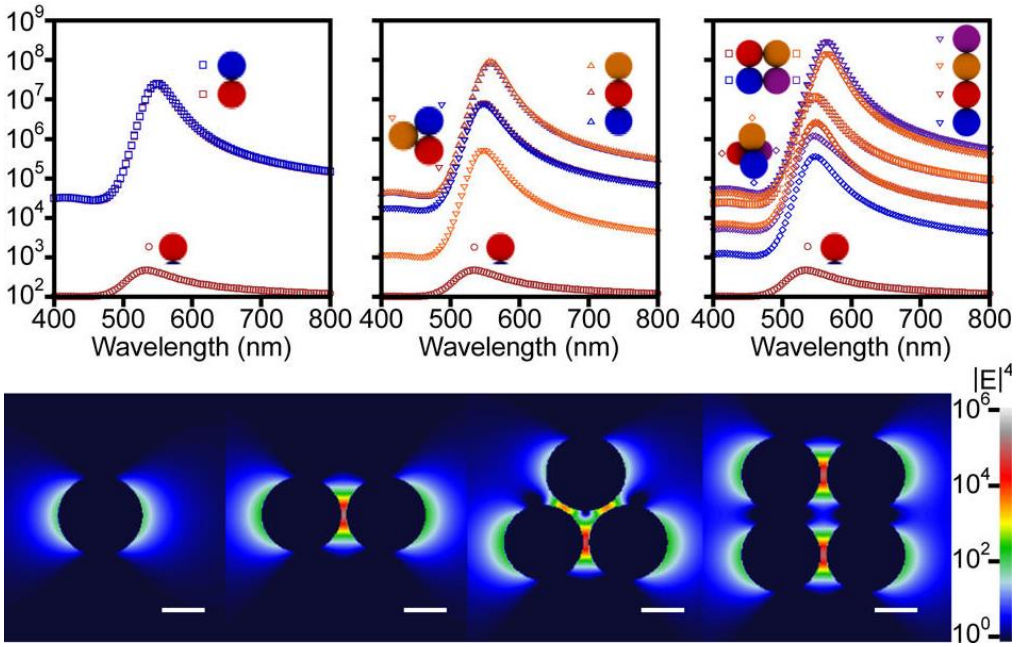

Figure 3. Dependence of plasmonic enhancement on nanoclustering extent. *Top:* Extinction profiles calculated using generalized Mie theory for 20 nm diameter particles separated by 1 nm for each differently shaped plasmonic clusters. The shapes correspond to differently organized clusters and the colors correspond to the different particles within a single cluster. *Bottom:* Electric field $|E|^4$ intensity distribution for each cluster type; in each image, the light is polarized from left to right. Scale bars are 10 nm. Reprinted with permission from Ross et al.[44] Copyright 2016 American Chemical Society.

The separation of a desired biomarker from complex biological samples is a key factor for translating SERS technologies to the point-of-care. For label-free methods monitoring the

intrinsic spontaneous Raman (SR) or resonant Raman (RR) modes of the analyte, the biomarker must be either pure or isolated from the media using extraction techniques such as HPLC or an immunoassay, or the biomarker itself must exhibit vibrational modes that contrast those from the background media.[45] Bringing these purification steps to the point-of-care often requires immobilization of affinity ligands such as antibodies or DNA aptamers onto wellplates, scintillation vials, or on glass slides using basic click chemistry.[46] The only downside of these ELISA or extraction kit-style designs is the required user-intervention for washing steps to remove optically or biochemically interferent components of the sample prior to SERS analysis.

SERS-active nanoprobes integrate the requirements discussed above in order to improve the speed of test results, reduce reagent costs, and to enhance the specificity and dynamic range of existing assays [47]. In general they involve one or more nanoparticles conjugated to 1) a highly polarizable Raman reporter molecule, 2) an affinity ligand such as an aptamer or antibody, and 3) a steric or electrostatic capping agent for stabilization in high salt environments [1, 3].

I.3.i Label-free colloidal SERS

Since Raman provides a chemical fingerprint of the probed sample, it may seem intuitive to detect disease identifying changes in an isolated biomarker's conformational structure by looking at the Raman modes coming from the analyte itself. In one example, our group was able to observed structure changes in the SERS spectra of for the biomarker β-amyloid absorbed onto aggregated gold nanospheres [48] that could be suggestive of Alzheimer's disease.

One particularly promising example was conducted by first by Fang [49] and later Wang [50] from Rong Chen's group using two abundant serum proteins, albumin and globulin, to detect colorectal cancer using real clinical samples. In Wang's work the two serum proteins were first purified from over 200 healthy and cancerous human serum samples. Protein samples were then added directly to hydroxylamine silver nanoparticles and acetic acid was used to aggregate silver nanoparticles to increase the magnitude of the SERS enhancement. SERS bands were assigned to verify specific biomolecular contents of the proteins, and to predict protein secondary structural changes that occurs with colorectal cancer progression using the difference of the SERS spectra between healthy and cancerous samples (aka SERDS). Principal component analysis and linear discriminant analysis were used to assess the capability of this approach for identifying colorectal cancer, demonstrating a diagnostic accuracy of 100% for albumin monitoring and 99.5% for globulin SERDS analysis. Additionally both the albumin and globulin partial lease squares (PLS) models successfully predicted the unidentified subjects with a diagnostic accuracy of 93.5%.

These results suggest that SERS analysis of serum proteins can be a sensitive and clinically powerful means for disease detection. However, simple direct sensing efforts like these still struggle to fully translate to the point-of-care, as they require complex sample preparation to be performed before SERS analysis. Thus these methods are not user friendly, are time consuming, involve complex statistical analysis or peak assignments, and require too many separate pieces of laboratory equipment to be fully implemented at the patient bedside. Integrating these techniques with lab-on-chip devices could overcome these hurdles, as discussed later.

I.3.ii Molecularly-mediated SERS

Indirect sensing using an assay whose SERS response is facilitated by a molecular binding event, particularity one that involves the biomarker itself, has emerged as an efficient approach to colloidal SERS. Oligonucleotides, antibodies, protein antigens, small molecules and dyes can all be immobilized onto metallic nanoparticles using thiol end groups, bifunctional PEG linkers, or sequential click chemistry [51-54]. Extensive work has been done by Duncan Graham and Karen Faulds' groups utilizing various oligonucleotide and resonant dye coated nanoprobes to form SERRS active nanoassembly complexes for multiplexed DNA detection [55]. In most cases, the nanoassembly detection modality involves the SERRS active particles' LSPR shifting in or out of resonance with the excitation source caused by hybridized DNA linking nanoparticles in close enough proximity to share conduction band electrons and red-shift their extinction spectra, and thereby a jump in SERS intensity, without causing irreversible aggregation. The group has translated their 'SERS-on' techniques for a variety of DNA, protein, and small molecule sensing applications, most recently by Mabbott et al. for monitoring four fungal probes in a multiplexed fashion [56], by Simpson et al. using a biomimetic glyconanoparticle assay for ultrasensitive (ng/mL) quantification of cholera toxin B-subunit [57], and by Gracie et al. for the simultaneous detection of two meningitis bacterial DNA biomarkers extracted from cerebral spinal fluid (CSF) clinical samples [58-59].

I.3.iii Magnetic micro- and nanoparticles for colloidal SERS

A major obstacle preventing the translation of DNA and aptamer-based molecular diagnostics at the point-of-care is the lack of sensitive yet also practical SERS methods that can be seamlessly integrated into portable platforms, again mainly due to some sample washing

required. Magnetic microbeads and superparamagnetic nanoparticles (SPIONS) [60] are easy to manipulate with small permanent neodymium magnets held at the side of a vial, wellplates, capillary tube, microfluidic channels or even inside cells [61]. When functionalized with sensing ligands, this allowing for faster, more automated washing steps while also preventing sample sedimentation often seen with repeated centrifugation [62-63]. Magnetic nanoparticles can also provide a plasmonic response when coated in gold or silver [64] , therefore improving SERS enhancement capabilities [65-67].

Many groups have facilitated this technique for improving clinical chemistry techniques recently, such as Wang et al., who used aptamers immobilized onto silver coated magnetic nanoparticles with a secondary SERS active gold nanoprobe coated in another aptamer to capture and quantify down to 10 bacterial cells/mL [68]. Ge et al. used a similar sandwich binding approach, but with antibodies in lei of aptamers for the detection of the ovarian cancer serum biomarker human epididymis protein 4 (HE4). They were not only able to demonstrate fg/mL limits of detection and a dynamic range of 1 pg/mL to 10 ng/mL, but also demonstrated that the assay particles could be washed and reused at least 5 times in their efforts towards developing easy to use diagnostic kits [69].

Tuan Vo-Dihn's group has also developed a sandwich-type SERS assay, relying on specific DNA hybridization to capture ultrabright SERS nanorattles onto magnetic microbeads [70]. Nanorattles are core-shell silver particles with resonance Raman reporters loaded in the gap space between the core and the shell, with DNA probes coated on the shell surface, thus acting as the SERS tags for signal detection. After hybridization, a magnet was applied to the bottom of the well to both remove unbound nanorattles and to concentrate the hybridization sandwiches at a localized detection area for SERS measurements. Probing for two specific

DNA sequence of the malaria parasite *Plasmodium falciparum*, one mutated and the other wild-type, it was found that SERS could detect malaria DNA down to 100 attomoles. Since the mutant sequence translates for resistance to artemisinin drugs, single nucleotide polymorphism (SNP) discrimination of wild type malaria DNA and mutant malaria DNA was also demonstrated. Their results show the potential for molecularly mediate SERS to differentiate small mutations in infections pathogens with far greater sensitivity than current methods, an important factor for global health applications.

I.3.iv SERS-based immunoassays challenge ELISA

SERS nanoprobes have recently be used to improve detection capabilities of immunoassays and potentially rival the ever popular enzyme-linked immunosorbent assay (ELISA) techniques. Combining SERS and ELISA, aka "SLISA', has proven to be an effective method for improving the limits of detection due to the intrinctic enhancement capabilities of SERS, speeding up assay reaction times due to the 3D architecture of functionalized colloidal nanoparticles, and capitalizing on the narrow spectra bands obtained with Raman for improving the multiplexing capabilities of traditional immunoassays [71]. Bhardwaj et al. directly compared the capabilities of SLISA and ELISA assays for the measuring RAD54 stress-marker protiens. They found SLISA has similar accuracy as ELISA, but improves upon the indirect enzyme based method by being reusable, faster, more direct, and easy-to-use. SLISA was also 5x more sensitive than ELISA while providing qualitative information on immuno-sensor's chemical characterization and antigen-antibody binding. This thereby allows direct detection with less uncertainty, which is a stringent limitation of all label-based biosensor technologies, including ELISA [72].

One example of an excellent biomarker candidate for SLISA is the hormone estradiol (17β-estradiol, E2) a critical serum protein in sexual development. Specifically, it's noteworthy that E2 levels are especially low (<10 pg/mL) in prepubertal girls, and unfortunately current clinical detection methods are insufficient for accurate assessment of E2 at these ultralow pg/mL concentrations. In a study conducted by Jaebum Choo's group, a new E2 sensor was introduced using a magnetic capture bead SERS immunoassay detection platform based on their previous work that validated the technique for use with clinical samples for the early diagnosis of arthritis[73]. The system involves a competitive binding assay with reagents immobilized onto magnetic beads to assist with automated wash steps and also to enhance the SERS response through magnetic aggregation in a glass capillary tube (Figure 4). Their SERS assay was tested with 30 blood samples to assess its clinical feasibility and their prediction results were compared those obtained using a commercially available chemiluminescence immunoassay. The commercial immunoassay failed to quantify E2 serum levels lower than 10 pg/mL, but the limit of detection of E2 using the novel SERS-based assay described in this study was an order of magnitude lower at 0.65 pg/mL. This verifies that SLISA-based methods have a strong potential in the early identification of biomarkers due to its exceptional analytical sensitivity.

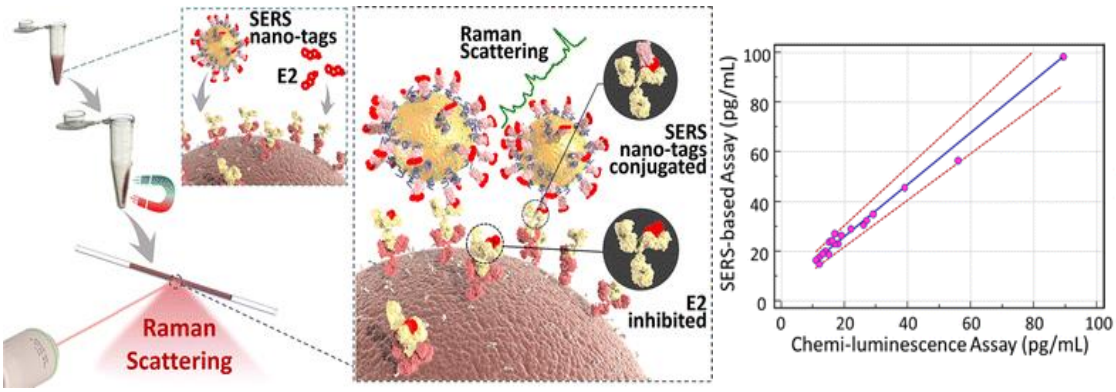

Figure 4. Schematic illustration of the SERS-based competitive immunoassay for quantification of E2- target where E2 and E2-conjugated SERS nanotags competitively react with anti-E2 antibody on magnetic beads. Right: Passing-Boblok regression plot for the determination of the bias and compatibility between chemiluminescence and SERS. Reprinted with permission from Chon et al [73].

I.4 Small molecule biomarker sensing, aptamers, & SERS

I.4.i A brief introduction to bisphenol-A as an endocrine disruptor

The underlying goal of the latter half of the research presented herein is to develop a new point-of-care (POC) detection platform and methodology for assessment of biological exposure to harmful foreign chemical compounds. In contrast to most prior approaches which attempt to measure the amount of such manmade compounds in the environment, the technology developed here will have the sensitivity and specificity to detect toxic agents in human blood samples directly and thereby determine the toxicological "load" within the patient. The end-product of this research is expected to have considerable impact allowing toxicologists, environmental health professionals, and clinicians the ability to correlate the effects of toxic chemicals to disease states.

A number of setbacks arise when designing sensing platforms for detecting foreign blood toxins with low immunogenicity, such as environmental agents/stressors. Though

environmental monitoring in air, water, and food and beverage packaging is well-established and regulated, there is still a need for reliable *human biomonitoring* methods in order to determine the body's burden with foreign toxins and their possible metabolites in the blood. Bisphenol A (BPA) is the monomer of an epoxy resin commonly used in plastic food and beverage packaging, a building block of polycarbonate plastic, and can be toxic to the endocrine system when exposed to humans. Though environmental monitoring of BPA in drinking water, and inside the food and packaging products themselves is well-established and strictly regulated by the FDA, a recent CDC study found BPA detected in 92.6% of the 2500 Americans participants,[74] demonstrating that there is still a need for reliable methods to determine how exactly BPA disrupts the endocrine control system.

BPA is used as an inner coating to protect metal food cans, water bottles, and other polycarbonate reusable containers from rusting and corrosion. The coatings are synthesized by the condensation of BPA with epichlorhydrin to produce BPA diglycidyl ether (BADGE). BPA leaches into food and beverage products from the coating, an epoxy resin, when incomplete polymerization occurs or after damaging UV exposure. The maximum tolerated dose for BPA is 1000 mg/kg body weight as determined by toxicology studies.[74] BADGE is a type of peroxisome proliferator-activated receptor- antagonist, which means it may activate or inhibit ion channel activity in vessel walls directly, though this claim requires further investigation and much remains unknown about the mechanisms involved in humans exposed to BPA and its derivatives.[75]

I.4.ii Aptamers for all

Biological assays for blood biomarker detection are most commonly realized using antibodies[76]. However, for sensing small molecules with low immunogenicity, raising antibodies would require complicated synthesis of a hapten–target carrier before animals can be immunized with that conjugate[76]. Recently, *aptamers*, highly specific and sensitive affinity molecules derived from nucleic acids, have been used as assay recognition ligands in lieu of typical antibodies[77-83]. An aptamer is typically a single short (<100 bp) oligonucleotide that has been folded into a tertiary structure ao that it has with both ds and ss portions, where the ss parts act as 'lassos' selective to binding to a specific antigen as depicted in Figure 5. Aptamers are specifically advantageous for sensing small molecules with low immunogenicity, where raising antibodies would require synthesis of a hapten–target carrier before animals can be immunized with that conjugate[76]. Selection of aptamers is an entirely *in vitro* process with the ability to perform counter selection steps and/or selection under non-blood conditions. This provides the potential for greater ligand specificity and affinity, and once identified, aptamers are readily produced by scalable chemical synthesis. Last, aptamer terminal functional groups are readily incorporated during synthesis for conjugation to nanoparticles, or other immobilization assay steps[84].

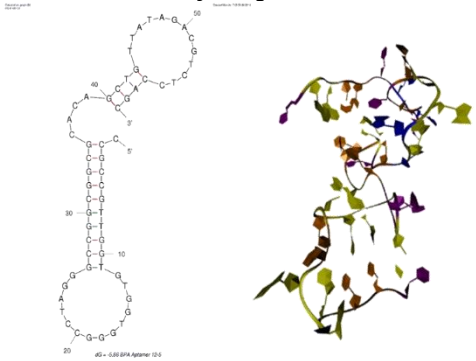

Figure 5. The secondary (left) and tertiary (right) structure of a ssDNA aptamer selected against BPA, drawn using Mfold and Rosetta Commons freeware, respectively.

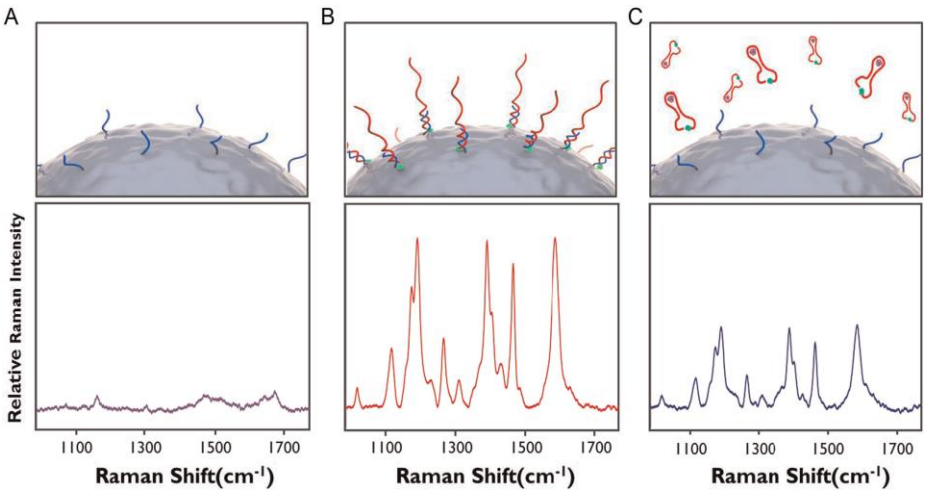

Figure 6. SERS spectra for (A) single strand probe DNA-embedded Au/Ag core–shell NPs, (B) cy3-labeled aptamer double strand DNA-embedded Au/Ag core–shell NPs and (C) aptamer-detached Au/Ag core–shell NPs in the presence of 100 nM BPA. Reprinted with permission from Chung et al. [85] Copyright 2015 Elsevier.

In one example combining aptamers and SERS for small toxin detection, Chung, Choo, et al. described a 'SERS-off' molecularly mediated SERS methodology using only aggregated silver colloid, relying solely on small molecule competitive binding to displace an aptamer tagged with a Raman dye molecule.[85] This method is detailed in Figure 6 and uses a partial complimentary sequence to immobilize a ssDNA aptamer onto Au/Ag core–shell nanoparticles. This method proved to be sensitive down to the 10 fM range for BPA-spiked tapwater, over a total dynamic range of 10 fM - 100 nM. The authors of this work acknowledged that this LOD is two or three orders of magnitude lower than that reported for other BPA sensing techniques, but may possibly be shifted higher if the samples were in complex biological media. Additionally, it is noteworthy that the total detection time was estimated to only be about 40 min including both the reaction between aptamer and BPA (30 min) and detection (10 min), making this option ideal for supplementing rapid diagnostic tests (RDTs).

CHAPTER II

CHARACTERIZATION OF MULTIPLE MICROFLUIDIC MODALITIES FOR "SERS ON" TYPE ASSAYS

II.1 Introduction to SERS-on-a-chip design requirements

The enhancement factor (EF) for each SERS-on-a-chip device was defined as shown in Eq. 1, and used to compare their sensing capabilities. While there are numerous methods for calculating SERS EFs and various rationales behind them, here we report the EF as a ratio of values with the units 'photons/mole'. For each EF calculation experiment, control scans of the RRM or analyte probed were collected using the same Raman microscope settings as the SERS-on-a-chip device at the lowest detectable concentration. Looking at the same peak intensity for the SERS and Raman setups, the maximum intensities at each limit of detection were divided by the concentration in *moles* (Eq. 1). Using this equation, a higher EF implies a lower limit of detection (LOD), but does not necessarily confirm or correlate to the lowest quantifiable (LOQ) concentration.

$$EF = \frac{\frac{I_{SERS}}{[C]_{SERS} \cdot V_{SERS}}}{\frac{I_{Raman}}{[C]_{Raman} \cdot V_{Raman}}} = \frac{I_{SERS} \cdot moles_{Raman}}{moles_{SERS} \cdot I_{Raman}} \qquad \textbf{Equation 1}$$

The limit of quantification (LOQ) of each chip discussed in this chapter is loosely defined as the lowest concentration at which the chip's average SERS intensity at a specified vibrational mode (typically chosen to be the spectra's sharpest or highest peak) can be statistically differentiated from the next two concentration points around it. Thus, a chip's theoretical LOQ is highly dependent on the intrinsic error within each individual chip (i.e. within each patient sample, or within each concentration on a calibration curve). The intrinsic

error of each chip tested is reported as a range of coefficient of variations, where each individual chip %CV is defined in Eq. 2 as the standard deviation over the mean for each chip at a specified SERS peak. This value can be thought of as the sensor's error or tolerance, i.e. if a chip has a CV=0.21 then the average SERS intensity for that concentration varies across the substrate surface by 21%.

$$\%\boldsymbol{CV} = \mathbf{100}\% \cdot \frac{\boldsymbol{STDev}\left(\boldsymbol{I_{SERS}}(\boldsymbol{\upsilon_{peak}})\right)}{\boldsymbol{Average}\left(\boldsymbol{I_{SERS}}(\boldsymbol{\upsilon_{peak}})\right)} \qquad \textbf{Equation 2}$$

II.2 Direct sensing of assay products on a SERS substrate

As an initial approach to improve upon the slow environment of current large scale blood analysis labs, we aim to eliminate the need for multiple devices in order to analyze multiple biological transduction methods. Specifically, LabCorp currently has the capabilities for analyzing assays with different output signal types such as spectrophotometric (UV-Vis, fluorescence, etc), enzymatic, electrochemical, mass spec, various types of size-exclusion chromatography, etc. However this type of multifaceted laboratory requires either 1) multiple designated personnel for each machine, or 2) a strong team of long-term employees who are able to endure lengthy training to master all bioanalytical equipment in the facilities. We propose to use SERS as an alternative method to eliminate the need for such numerous and large scale lab equipment. Given its capabilities to be tuned to virtually any desired analytical range and the fact that any molecule with a polarizable bond has a detectable Raman signal, we are able to sense an endless variety of analytes.

In the remainder of this sub-chapter II.2, two SERS-on-a-chip devices are presented for the analysis of three common analyte types: 1) Small Molecule- Adenine (nucleotide used for

DNA-nanoparticle binding confirmation), 2) Unlabeled Protein – UCH-L1 (traumatic brain injury biomarker found in the optically-clear CSF), and 3) Dye-labelled Protein – Myoglobin*Rhodamine-6G (Myo*R6G, emulates a cardiac biomarker immunoassay product in that R6G is also a fluorophore). Both designs utilize *mechanical* trapping and aggregation of 60 nm commercially available gold nanoparticles (Polysciences) at a micro- to nano-fluidic junction. This allows for a high density of aggregated nanoparticles at a defined region for more reproducible formation of SERS active sites (aka 'hot spots') located between aggregated nanoparticles: where the analyte is to be trapped. Schematics of the two SERS-on-a-chip devices characterized in this subsection are compared in Figure 7.

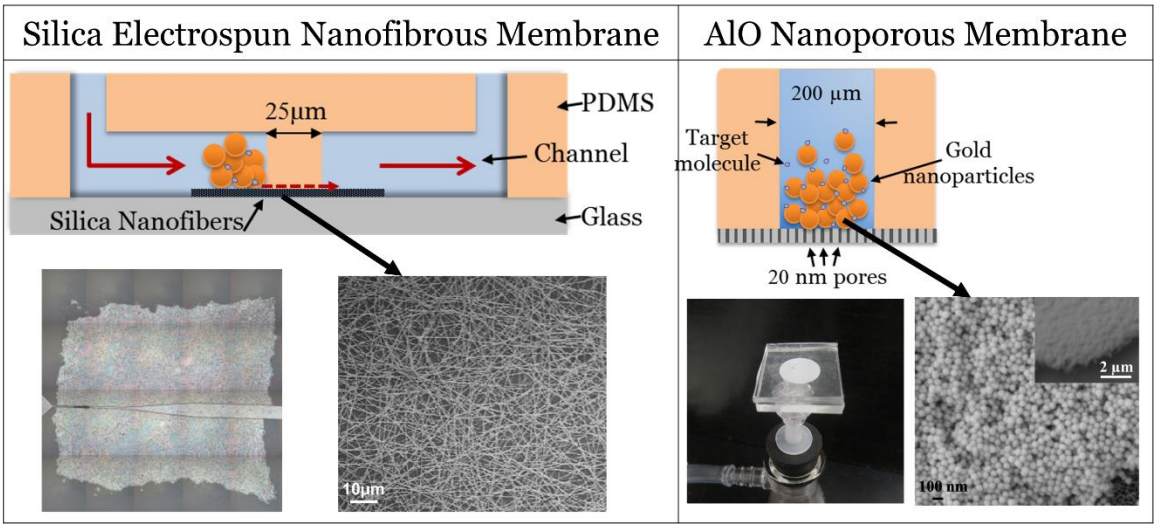

Figure 7. Comparison of the mechanical aggregation based SERS-on-a-chip devices for direct sensing of analytes.

II.2.i Silica electrospun nanofibrous membrane

With the goal of generating reproducible SERS hot spots on chip, this device exhibits a micro-to-nano junction for mechanical aggregation with a silica electrospun nanofiber membrane sandwiched between inlet and outlet microfluidic channels, where gold

nanoparticles and the analyte can then be trapped sequentially. The nanofibrous membrane was constructed by electrospinning a polymeric-silica composite onto a glass slide, followed by high temperature disintegration of the polymer. PDMS microfluidic channels were fabricated via an SU-8 mold and bonded with the glass slide patterned with the silica nanofiber membrane bottom layer. The small pores created by the deposited nanofiber membrane enabled flow through the 25-µm channel region. A schematic of the assembled device and flow chart detailing this fabrication process can be found in Figure 8). This chip's fabrication is relatively simple in that it does not require the use of a cleanroom or special training, only a fume hood, high voltage power supply and high temperature oven (>500°C).

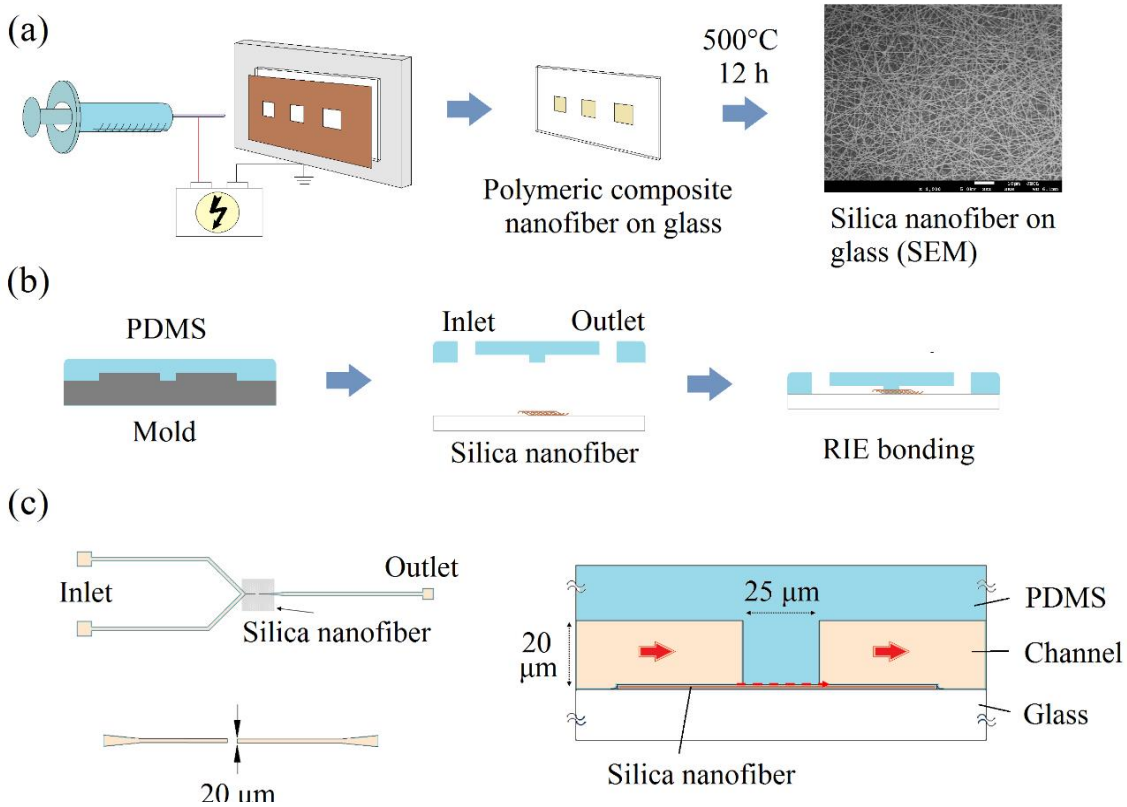

Figure 8. Fabrication process for SERS chip facilitating mechanical aggregation of gold NPs at the entrance of a nanoporous membrane. (a) Fibers are electrospun onto glass slide, polymer is removed in high temperature bake step (b) PDMS microfluidic channel is lifted from SU-8 mold and bonded to glass slide with the indentation over the nanofibers. (c) Schematic of the assembled device. *Left:* top view of the device *Right*: side view of the chip.

The nanofibrous structures were designed to exhibit ~10 nm pores and, when vacuum is applied at the chip outlet; the particles aggregate at the junction while the buffer solution passes through. To verify that the silica fibers formed a mesh that provides pores on the nanoscale, 20 µl of commercially available 1 µm polystyrene (PS) beads (diluted 1000:1 from Sigma stock) placed at the channel inlet followed by syringe-vacuuming with 1/3 of 1 mL possible full extraction. Brightfield images were collected over time until particle aggregation became visible at the channel entrance to the nanofiber mesh (Figure 9, left). No visible leaking of the 1 µm beads after 40 min implies the nanofibers provide pores on the nanoscale.

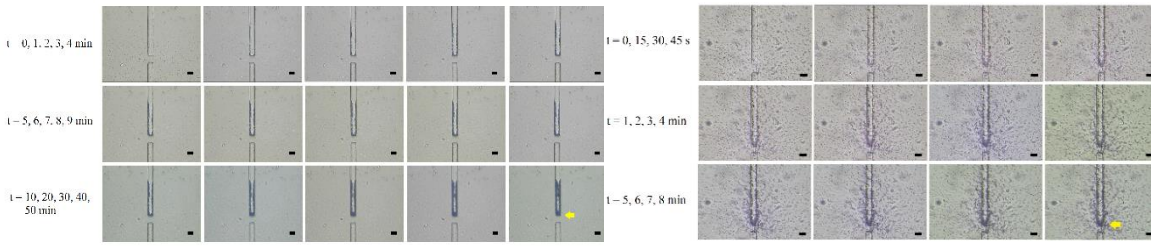

Figure 9. Brightfield images of particles aggregating at the entrance to the nanofiber mesh, scale bar is 20 µm. *Left:* 1 µm polystyrene beads in nanofibrous channel for verification of nano-pore formation. *Right:* 60 nm gold nanoparticles, chip outlet under vacuum for 8 min until adenine SERS signal saturation.

Next, a similar experiment was conducted using 20 µL of commercially available 60-nm gold nanoparticles (Unconjugated PolyGold, Polysciences, Inc.) and a syringe-vacuum system using the full 1 mL air extraction. Images were taken during the process of aggregation until particle aggregation appeared to reach a steady state (~ 5 min, Figure 9, right). Unfortunately from the brightfield images it can be seen that a significant portion of the nanoparticles leaked out into the nanofibrous membrane rather than remaining concentrated at the junction as was seen with the polystyrene microbeads. Looking at the two images in Figure

9 together, it can be inferred that the nanofibrous membrane must provide a membrane of pores somewhere on the order of ~70-900 nm.

To determine the limit of detection and quantification capabilities of the nanofibrous SERS chip, a 20 µL solution of the nucleotide adenine at concentrations from 100 nM to 100 µM was pulled through 4 separate nanofibrous channels (where all 4 fibrous regions were patterned at the same time on the same glass slide) preloaded with gold nanoparticles. It is assumed that the adenine is oriented on the gold surface as predicted by Juewen Liu,[86] as shown in the schematic in Figure 10. Adenine's major Raman vibrational mode (aromatic ring breathing[86] located at 735 cm^{-1}) was observable after 16 minutes, and the signal at the junction between the microchannel and nanofibers reached a steady state after ~ 2 h (Figure 11a). It can be observed in Figure 11b that the limit of detection of this design was 1 µM, as the

Figure 10. Chemical structure and assumed orientation of the nucleotide adenine on gold

735 cm^{-1} peak from the 100 nM chip was difficult to distinguish from the noise.

Finally, the enhancement factor (EF) for this SERS-on-a-chip device was determined using the spectra shown in Figure 11c to be ~10^6. While these initial proof of concept experiments seemed somewhat promising, it was discovered that there was extreme inter-chip variability (>100%) due to difficulties in repeatability with the 'homemade' electrospinning process. Keeping in mind there are 4 replicate channels per chip, this means each chip would

need to be calibrated to the first channel and only 3 samples could be run before a new calibration was necessary. Additionally, the limit of detection of 1µM was far too high to be relevant for physiologic concentrations, and the degree of gold nanoparticles leaking into the nanofibrous mesh proved inconsistent from chip to chip. However this chip may still be of value as a potential option for fluid filtration, for example, in the removal of large cellular components (>1 µm) form blood or other bodily fluids, and allowing protein and small molecule components (< 60 nm) to pass through to a second analysis chip.

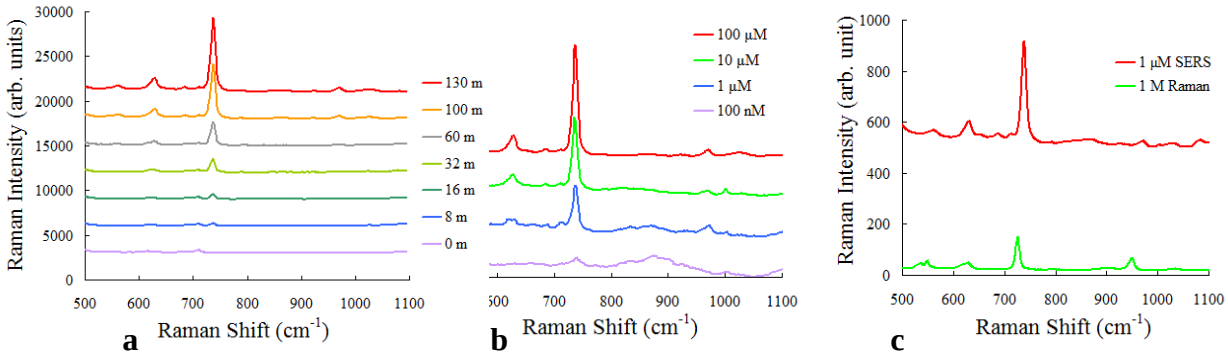

Figure 11. a) 100 µM Adenine collecting in the nanofiber channel over ~2 h. b) Concentration dependent adenine SERS spectra. c) SERS spectra of 1 µM adenine compared to spontaneous Raman spectra of adenine at 1M for EF calculations.

II.2.ii Aluminum-Oxide nanoporous membrane

To overcome repeatability issues faced with the nanofiber design, for the next mechanical aggregation based SERS-on-a-chip device a commercially available aluminum oxide (AlO) nanomembrane (20 nm pore size – Whatman Inc.) was sandwiched between two slabs of PDMS. The top PDMS layer, i.e. the inlet, includes an embedded 200 µm glass capillary tube to encourage capillary flow with hope of eliminating the need for the syringe. However it was discovered that the small pore size would not allow for capillary action across the nanomembrane as anticipated. Therefore light vacuum suction was applied at the channel outlet (PDMS slab with 1 mm hole made with a biopsy punch), as depicted in Table 1 and Figure 12 below.

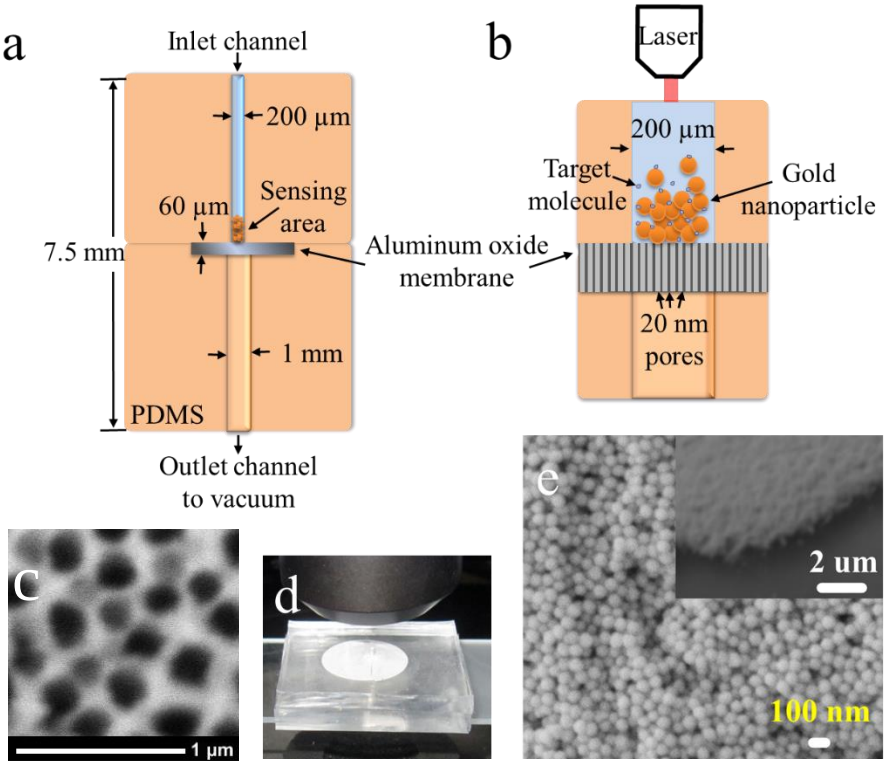

Figure 12. a) Side profile of the nanomembrane SERS-on-a-chip device b) Magnified schematic of the sensing region c) SEM images of the AlO nanomembrane d) Brightfield image of the assembled chip e) SEM images of 60 nm gold on the surface of the nanomembranes.

Initially this nanomembrane-based device demonstrated significant improvement when tested with adenine. Just as with the nanofibrous chip testing in the previous subsection, 20 µL of commercially available 60-nm gold nanoparticles were preloaded into the chip with vacuum suction, followed by 20 µL of adenine at various concentrations. The nanomembrane SERS-on-a-chip demonstrated an enhancement factor of 10^9, three orders of magnitude higher than the nanofibrous chip as shown by their comparative 1 µM adenine SERS signals in Figure 13a. Additionally, the limit of detection for the nanomembrane was 1pM, six orders of magnitude lower than the nanofibrous chip, with an intra-chip variability of 18% as shown in Figure 13b.

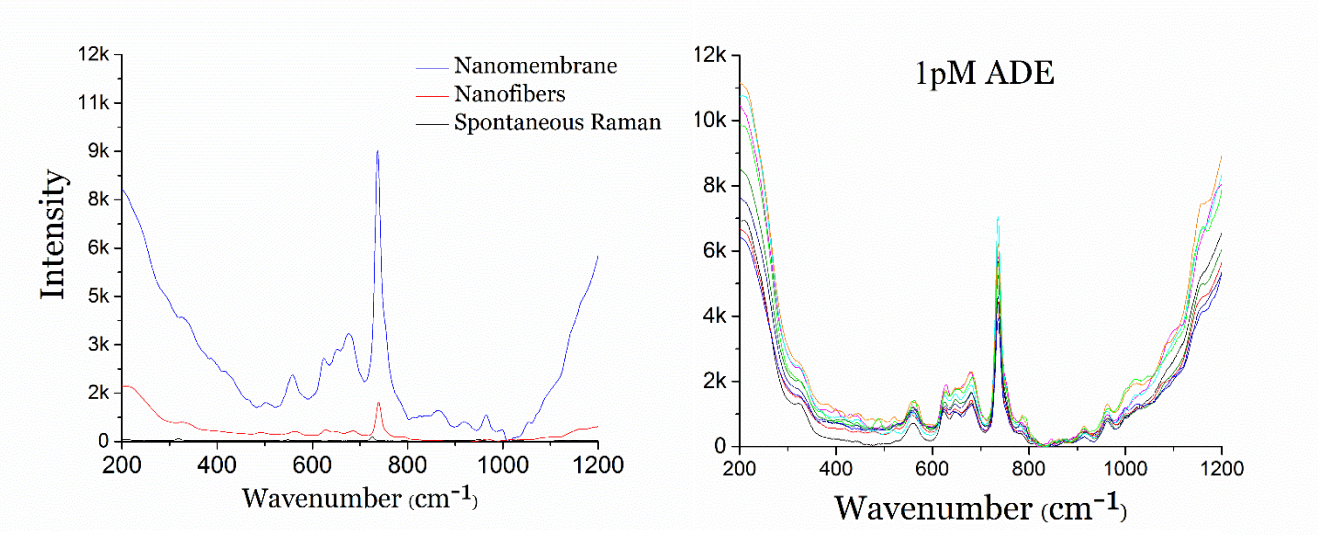

Figure 13. a) Comparison of nanofiber (design 1) and nanomembrane (design 2) SERS-on-a-chip devices at 1 µM adenine compared to 1 M spontaneous Raman. b) 9 scans taken at random points across the 200 µm sensing region.

II.2.ii.a Amino acid (citrulline)

Next, the nanomembranes chip's ability to quantify a more clinically relevant analyte, the amino acid citrulline, which has recently emerged as a blood biomarker indicative of gut function after radiation exposure (Figure 14)[87] was investigated. The current gold standard for

radiation biodosimetry is the dicentric chromosome assay (DCA). This technique is based on detecting the abnormal fusion of two chromosomes and is very reliable, however, also extremely time consuming (tests take several days) and expensive.[88] There are a number of developed assays for radiation exposure, most of which are based on gene expression and at the benchtop phase, but have the potential for microfluidic integration.[88-91] Brengues et al. report monitoring gene expression indicative of radiation exposure has integrated their quantitative nuclease protection assay (qNPA) into a microfluidic "front-end" platform chip. However their "back-end" chemiluminescent detection chip and blood filtration portions have not been developed yet.[92] Therefore, this biomarker would be a suitable candidate for analysis with the developed SERS-on-a-chip device.

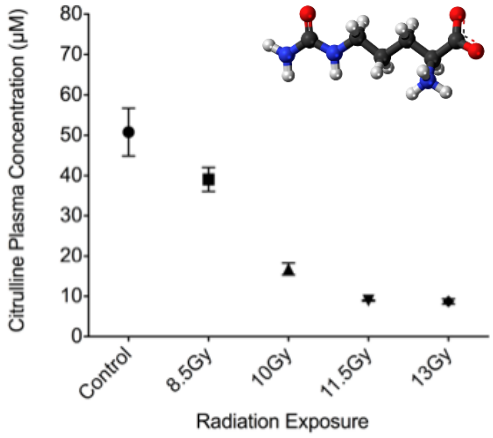

Figure 14. Effects of ionizing radiation on blood citrulline concentration in mice (inset: molecular structure of citrulline).

Citrulline was detectable by Raman in its powder form, highly concentrated liquid form, and using SERS at twice the average physiological concentration (

Figure 15). Since there were an unusually large number of peaks detected for a weakly polarizable molecule, it was confirmed that the peaks detected did indeed corresponded to the

citrulline molecule's vibrational modes as assigned in Table 2 by comparing the SERS spectra to spontaneous Raman spectra in powder and liquid forms. Finally, the experiment was repeated for six concentrations encompassing the physiological range from 1 μM → 100 μM. As shown in Figure 16, the SERS-on-a-chip device was able to detect across the full range, however the sensor was not quantitative.

Table 2. Raman vibration mode assignments for citrulline.

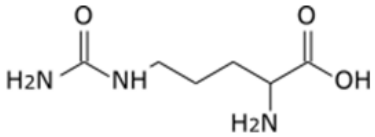

Assignment	Spontaneous Raman		SERS
	Powder	Solution	
	490	468	478
	527	526	521
	654	658	631
	671		692
β(CH), oop	754	753	761
C-C ν	855	856	844
C-C ν	940	930	930
	993		999
C-C ν	1018	1008	1013
C-N ν	1070	1100	1076
NH3+ δ	1140	1117	1141
NH2+ γ	1176	1147	1176
γ(NH) / δ(NH)	1258	1212	1238
ν(C-C/C-N) / C-C-C def with N-H ip wag	1297	1328	1280
C-H γ	1353	1351	1356
COO ν	1399	1415	1383
β CH3 asym	1479	1444	1481
COO ν	1582	1556	1586

δ = in-plane deformation, β = bending, γ = out-of-plane deformation, ν = stretching, oop = out-of-plane, ip = in-plane, asym = asymmetrical

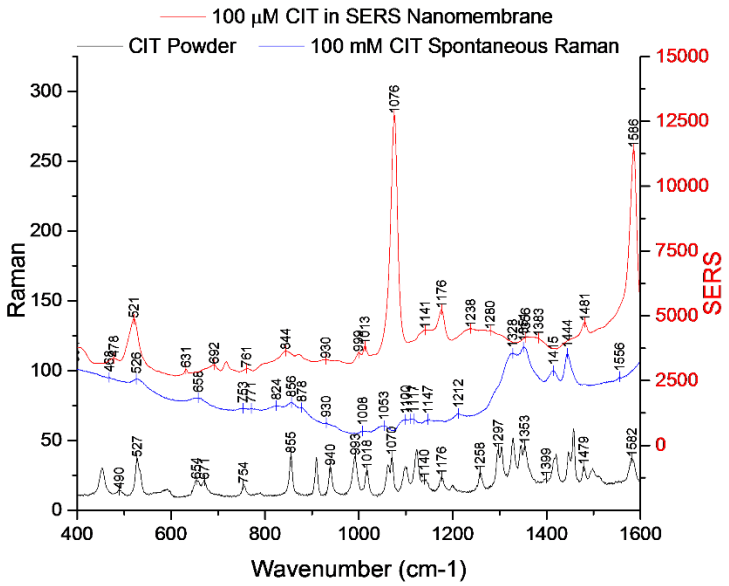

Figure 15. Raman and SERS spectra of citrulline with peak assignments labelled.

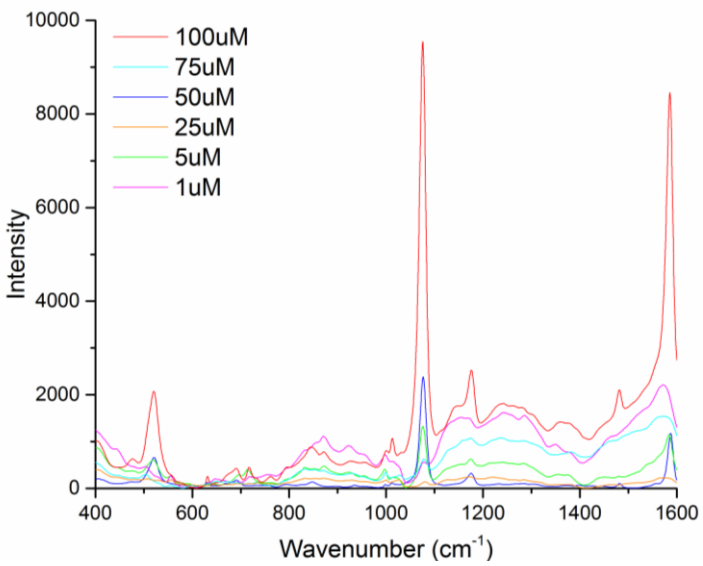

Figure 16. Limit of quantification experiment for citrulline in the nanomembrane SERS-on-a-chip device.

The variability across concentrations is likely due to the fact that the citrulline molecule is allowed to adsorb onto the gold nanoparticles at any random orientation and at any packing density across the chip. In other words, since the analyte concentration is directly related to the packing density and orientation of the molecules on the surface of the gold it also has a significant effect on which Raman bands are enhanced and to what degree depending on how polarizable the molecule is at a given orientation/packing density.

To determine if citrulline's intrinsic Raman spectra was capable of being isolated from complex media for true direct sensing, citrulline at the average 'healthy' physiological concentration of 50 µM was doped into fetal bovine serum. Next 100 µL of the sample was pulled over the gold particles on the nanomembranes, and this experiment was repeated in a control experiment using 50 µM bovine serum albumin (BSA). The average SERS spectra across the nanomembrane for each is shown in Figure 17. Though citrulline's dominate 1076 cm^{-1} peak is still significantly stronger in the doped sample than in control, when observing

their full spectra the citrulline profile still mirrors that of BSA, and given that it is an amino acid, this is expected.

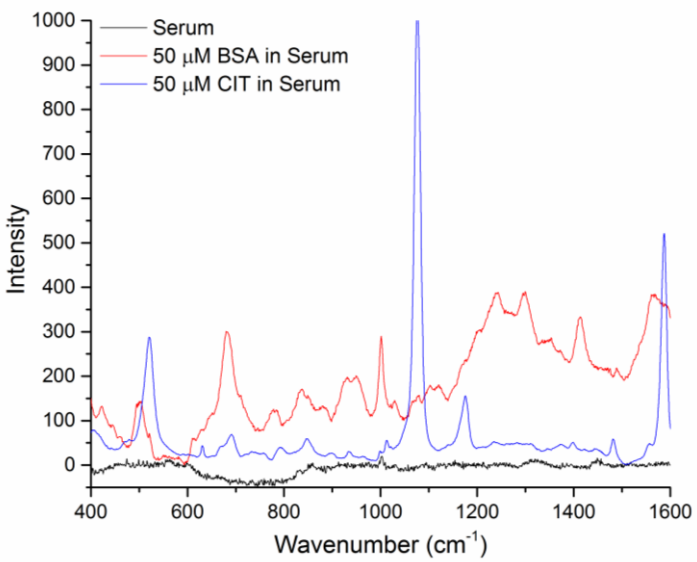

Figure 17. Comparison of SERS spectra on the nanomembranes chip of bovine serum samples doped with citrulline (blue) and albumin (red).

II.2.ii.b TBI biomarker proteins (UCH-L1 & NSE)

Since it was determined in the previous subchapter that quantitative analysis by direct sensing of an amino acid was not possible, but that the amino acids spectra was differentiable from a complex biological media, the next aim was to determine if instead the chip could be used to simply identify protein biomarkers by their structure. In this subchapter, we aim to identify two traumatic brain injury biomarkers: ubiquitin C-terminal hydrolase – L1 (UCH-L1) and neuron specific enolase (NSE), both found at elevated levels in the CSF as recently discovered by Banyan Bio.[93]

After traumatic brain injury occurs, medical and military professions use the Glasgow Coma Scale (GCS) determines the intensity and duration of loss of consciousness and coma.

The score is based on "motor responsiveness, verbal performance, and eye opening".[94] The score ranges between 3 and 15 points, 3 being the most severe case.[95] The *GCS* score then places the patients' outcome into loose treatment categories*:* dead, vegetative state, lower severe disability, upper severe disability, lower moderate disability, upper moderate disability, lower good recovery, and upper good recovery. Although widely used, the results may vary between individual assessors due to the need for personal judgment, a basis on social roles and need for a verbal response from the patient.[96] A SERS-on-a-chip device for detecting the biomarkers discovered by Banyan (UCH-L1 & NSE shown in Figure 18) at the point-of-care could provide a less symptom-based diagnostic approach for TBI patients.

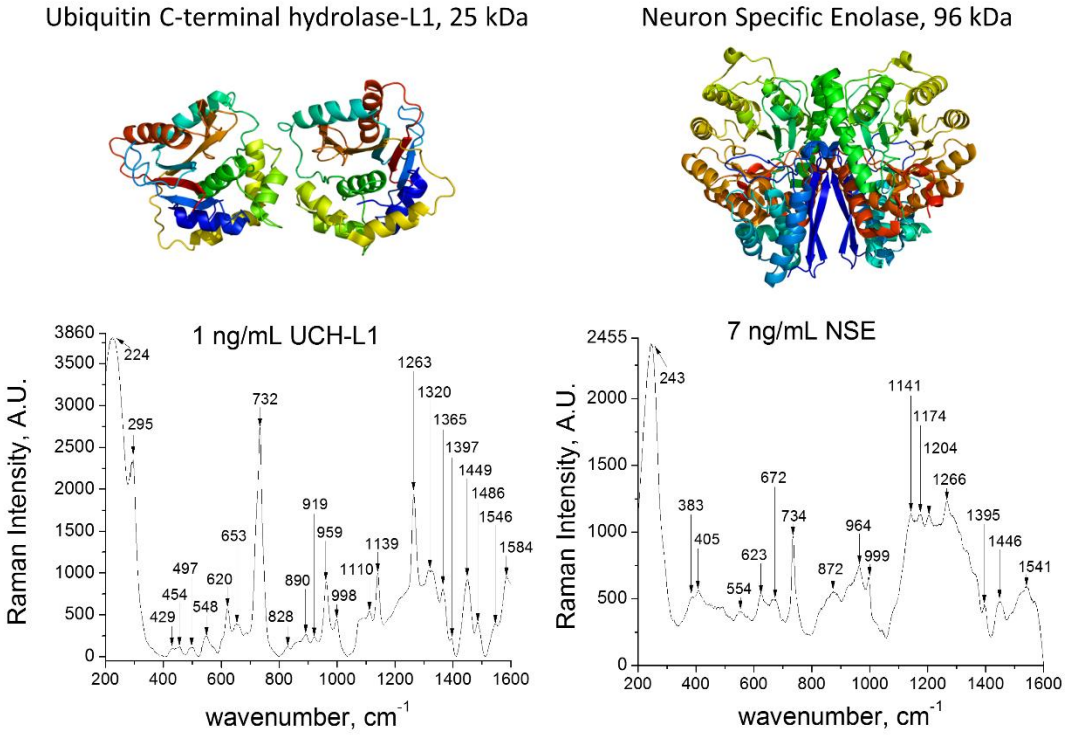

Figure 18. Structures and SERS spectra with peak assignments for TBI biomarkers UCH-L1 (left) and NSE (right) at physiological concentrations on the nanomembranes chip.

Concentrations in the physiological range of the traumatic brain injury biomarkers found in the CSF were pulled over 200 µL of gold nanoparticles. There was 100 x more gold used in these experiments than previously due to the fact that we are less concerned about creating a uniform field of enhancement and more concerned with the visualization of as many peaks as possible in order to predict protein structure. The SERS Raman bands were assigned as shown in Figure 18 alongside the structures of the proteins on the basis of existing literature pertaining to the spectra of amino acids and proteins. As expected, aromatic rings (828, 872, 1000, 1110, 1204, 1546), methylene vibrational modes (1266, 1320, 1365, 1449 cm^{-1}), carboxylic group vibrations (620, 964, 1397, 1584 cm^{-1}), stretching of disulfide bonds (500 – 550 cm^{-1} and 650 – 675 cm^{-1}) and the α-helical secondary structure (890-960 cm^{-1}) dominate the SERS spectra. The UCH-L1 Raman bands are sharper than NSE likely due to its smaller, simpler structure as the protein randomly adsorbs to the gold surface. However, previous studies of label-free detection of proteins[48, 97-98] have shown similar Raman modes to these, therefore the ability to measure these trace proteins in a complex media such as whole blood or plasma is not feasible.

*II.2.ii.c Labelled protein (Myo*R6G)*

At this point there is a realization that unlabeled protein biomarkers are too similar in structure to differentiate or quantify using their intrinsic Raman spectra. However, since many diagnostic immunoassays already exist and typically output proteins tagged with fluorescent probes, we make one more attempt to utilize the nanomembranes chip in an effort to quantify these types of assay products. Since fluorescent molecules are highly polarizable in nature, they also make for excellent Raman reporter molecules, especially when using a near-IR 780

nm diode laser for excitation. This laser line will not excite most fluorophores, therefore avoiding the dreaded fluorescent background signal and signal quenching observed when using a 532 nm laser, which would be closer to the plasmon resonance of 60 nm gold (λ=522 nm). In this chapter, we attempt to quantify myoglobin, a well-known cardiac biomarker, tagged with the fluorescent probe rhodamine-6G (conjugate referred to as MYO-R6G) at physiological concentration range found in the blood plasma of 20 ng/mL – 500 ng/mL (1.2 nM – 30 nM). Myoglobin is the earliest sensitive marker of cardiac injury with levels elevated within 2-3 hours of myocardial infarction, where the mean delay of onset of symptoms to first blood sample is four hours, too early for positive cTn results alone.[99-100] Myoglobin has a negative predictive value of virtually 100% for excluding early infarction within 4 hours of admission,[101] demonstrating a critical need for monitoring cardiac biomarkers at the patient's side.

It is noted that for these experiments, the PDMS slab was replaced by plastic and rubber bearings to hold the nanomembranes in place (Figure 19), with the hopes that the more ridged chip would result in more even vacuuming suction when preloading gold particles onto the chip. First, the spectra for MYO-R6G was compared to that of R6G alone to identify if the conjugate's peaks belong to the dye or to the protein (Figure 20). From this figure it was also

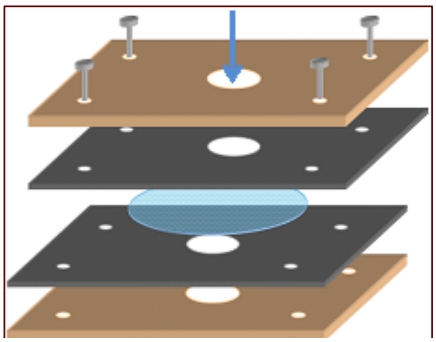

Figure 19. The modified nanomembrane SERS-on-a-chip sensor is composed of plastic plates, rubbers layers, and the nanoporous membrane with the arrows showing the direction of sample flow.

calculated that the EF of the sensor for the R6G dye alone was 10^8, one order of magnitude below the EF for adenine of the same chip, likely due to adenine's tendency to adsorb onto the gold surface, yet R6G provides significantly more peaks available for analysis, as the molecule is significantly more polarizable than adenine.

SERS spectra were collected for the physiologically relevant detection range of myoglobin (20 ng/mL → 500 ng/mL), and a monotonic concentration dependence was

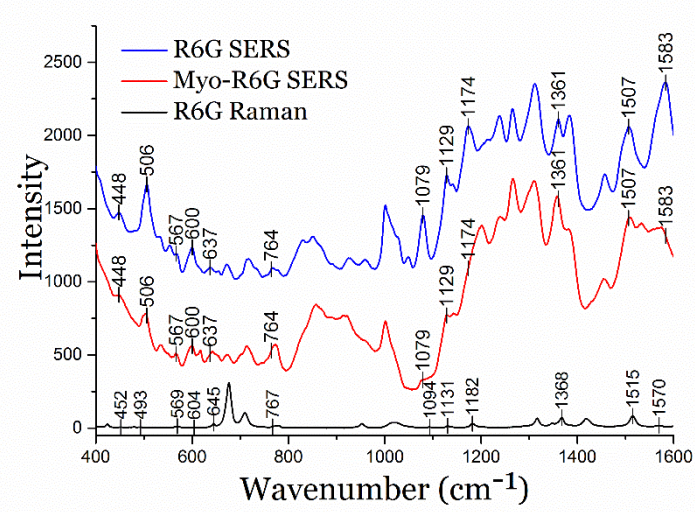

Figure 20. Comparison of the SERS spectra and Raman band assignments for R6G with MYO-R6G in the nanomebrane SERS-on-a-chip device.

observed for two MYO-R6G peaks at 567 cm^{-1} and 600 cm^{-1}as shown in Figure 21a. Next the same concentration range of MYO-R6G was doped into a solution of 10 µM BSA, the largest and most abundance protein in plasma, as an interferent protein demonstrated that concentration information is obtainable in complex media. Though the EF was reduced by a factor of 10 in a protein rich media, the same monotonic trend was still observable for both peaks when normalized (Figure 21b). The variability of nine scans taken across the nanomembrane area of aggregation was 8.5% - 15.3% in water and increased to 14.7% - 35.2% in BSA for all peaks of interest, likely due to steric hindrance from the protein rich media preventing MYO-R6G from being as close the gold surface as possible. It is hypothesized that

an even more complex medium, like undiluted plasma, would render even more interferent proteins nonspecifically adsorbing to the surface. This was tested by doping the highest physiological concentration of MYO-R6G (500 ng/mL) into plasma, and indeed the R6G peaks were no longer distinguishable from the background noise.

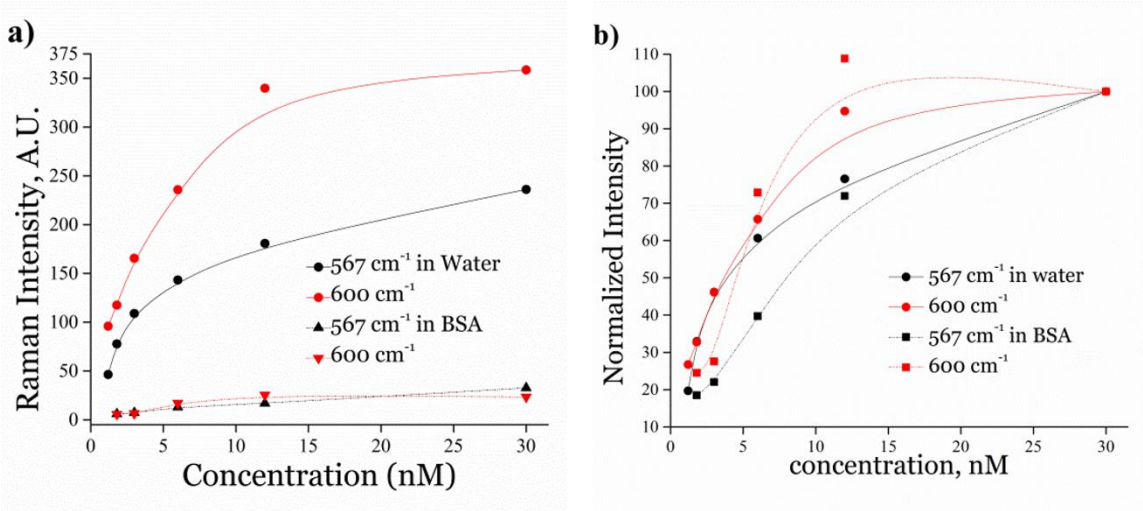

Figure 21. SERS intensity of myoglobin-R6G in water and BSA. (a) Monitoring the 567 and 600 cm-1 range yields quantitative information over the physiological range of myoglobin and in a complex media. (b) Intensity normalized to [0 100] for each data set.

II.2.iii Final thoughts on direct SERS sensing

Based on the previous sections, it can be said that direct SERS sensing of clinical chemistry analytes cannot be used for quantitative analysis using mechanically aggregated gold, which is the commercially available 'gold-standard' type of enhancement for SERS-on-a-chip devices. While using a Raman active dye demonstrate semi-quantifiable results, the chip failed to detect the target when in complex media. All chips presented in this section determined the analytes concentration by isolating its peaks from those in complex media, rather than physically isolating the molecule as is done in traditional assays. However, it is determined from these experiments that there are too many similar Raman modes in biological

fluids, giving rise to too many sources of error. Additionally, allowing analytes to randomly adsorb onto the gold surface prevented the sensor from obtaining quantifiable results as with the citrulline experiment, while molecules known to preferentially bind to gold like adenine or predicted to lie flat on the surface in a repeatable manner when analyzing concentrations across a narrow range, as with the MYO-R6G experiments in ideal conditions. Therefore, it is concluded here that an assay involving nanoparticles conjugated to known Raman reporter molecules must be developed for SERS-on-a-chip type sensors to be realized at the point-of-care.

II.3 Indirect sensing of SERS nanoprobe assay products

In this section, a "SERS On" aptameric competitive assay is presented for the target analyte bisphenol-A. The proposed point of care blood diagnostic device will require a microfluidic cartridge-based biosensing system in order to provide an appropriate environment for the aptamer assay and to house and aggregate SERS active nanoparticles for detection. This chapter will discuss a competitive-binding sensing chemistry using functionalized SERS nanoprobes with target aptamer specificity, with the goal of significant and quantifiable SERS enhancements of the assay product at a known location in a channel and deposited on a dry surface. The reproducibility of the spectra, specificity of the SERS nanoprobe to the target aptamer, and an ability to integrate the sensor platform and assay into one lab-on-a-chip device will be investigated.

A schematic of the proposed assay in shown in Figure 22. Aptamers will be immobilized upstream of a nanochannel constriction, where they will subsequently be pre-bound to the toxin-conjugated nanoprobes described in section II.3.i. When free BPA toxins are added, they should compete with the pre-bound nanoprobes for aptamer binding sites, releasing the nanoparticles for detection. To elaborate, in the absence of analyte, all functionalized nanoparticles are bound to aptamers in the upstream portion of the microchannel and are prevented from aggregating at the entrance to the nanochannel constriction. No gold would be at the entrance to the nanochannel beforehand as in previous SER-on-a-cip designs, and therefore regardless of the complexity of the sample, virtually no signal should be detected. In the presence of analyte, the target biomarker competitively binds with the immobilized aptamer, thus releasing the functionalized nanoparticles, and allowing them to flow downstream for detection at the entrance to the nanochannel. The RRM has a unique SERS signature and is located closer to the nanoparticle surface and is more concentrated than everything else in the overall sample volume, and thus should be is easily distinguishable from any potential confounding signals from colloid buffers, serum proteins, or other interferents from whole blood.

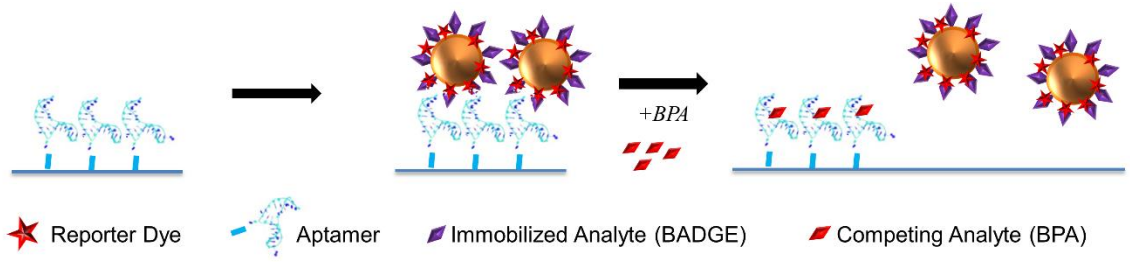

Figure 22. Proposed "SERS On" competitive binding assay schematic. Nanoparticles are competitively freed from aptamer tethers by competing free BPA from patient serum, then collected in a nanochannel or dried for analysis.

In this chapter a functional SERS nanoprobe with specific affinity to a BPA-binding aptamer is characterized. The binding affinity of the nanoprobe and its specificity to the BPA aptamer is quantified using microscale thermophoresis (MST). This approach monitors the signal depletion of a fluorescently labeled aptamer as it moves along an induced temperature gradient[102-103]. The thermophoresis of molecules is size dependent, and thus titration experiments are used to quantify the aptamer-nanoparticle binding and determine the dissociation constant K_d. The plasmonic properties of these capture nanoprobes and their capabilities for quantitative SERS detection are also investigated. It was demonstrated that the described SERS nanoprobes are capable of acting as both a capture and detecting element for BPA assay development.

II.3.i Conjugating BPA to a SERS active nanoprobe

SERS nanoprobes require three key conjugated elements: (1) a Raman reporter molecule (RRM) for quantitative identification, (2) a protective element for particle stabilization, and (3) a ligand for assay-specific biorecognition[31]. In order to reduce the *number* of Raman bands for simplified spectral multiplexing, the RRM should also have a low atom count and/or be highly symmetrical[53, 59, 104-105]. Furthermore the RRM must provide a functional 'head' group for chemisorption to the nanoparticle, most commonly chosen as a thiol (R-SH) for its well-defined covalent attachment to gold[106-107]. Formation of a self-assembled monolayer (SAM) of RRMs on the nanoparticle surface allows for dense packing of molecules with uniform orientation, improving the reproducibility of the SERS signal[105, 108-110]. The RRM's terminal 'tail' group type also contributes to the dynamics of the nanoparticles

as its charge directly affects the total particle surface charge, determining the degree of electrostatic stabilization[111-112].

Though a Raman reporter SAM can independently act as the nanoprobe's stabilizing capping agent, additional *steric* stabilization is often desired for mechanical repulsion between particles. Conjugation of polymers such as poly(ethylene) glycol (PEG)[54, 113-115] or polyvinylpyrrolidone (PVP)[105, 116-117] to the nanoparticle as part of a mixed SAM, to the RRM's 'tail' group, or silica shell encapsulation[52, 105] of the particles drastically improves the colloid's shelf life, even under harsh conditions. Sterically stabilized nanoprobes exhibit minimal non-specific adsorption, and can also provide functionalized surfaces and binding sites for further bioconjugation.

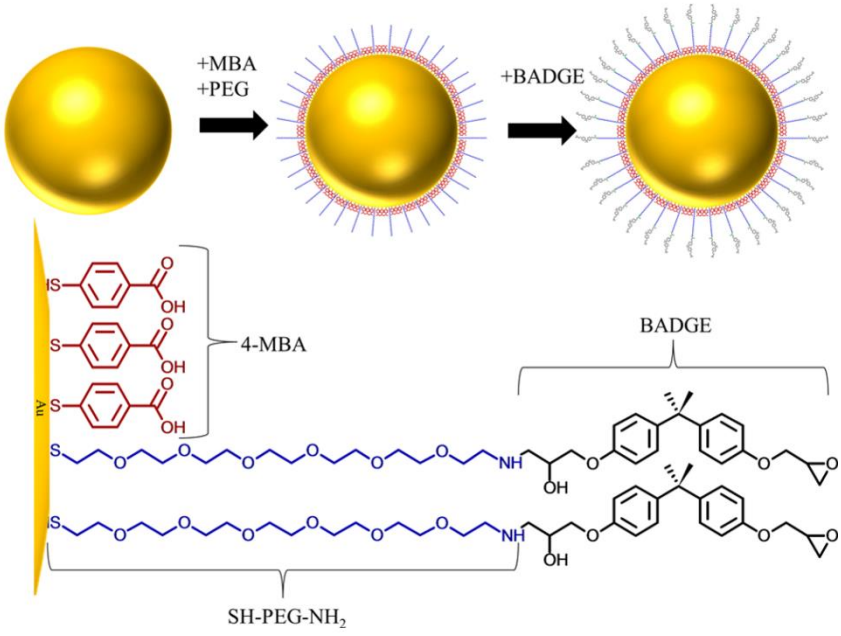

Figure 23. Scheme for the synthesis of BADGE-functionalized SERS nanoprobes. Below: chemical structures of mixed SAM components[3].

The design of the BPA assay SERS nanoprobe, reliable reaction conditions for its repeatable production, and ratios of conjugates have been optimized as detailed in Appendix #. The BADGE functionalized SERS nanoprobes were synthesized according to scheme in Figure 23, and are comprised of (1) mercaptobenzoic acid (4-MBA) acting as the RRM, (2) a hetero-bifunctional PEG linker providing steric stabilization and protection from unwanted adsorption, and (3) the analyte of interest, bisphenol A diglycidyl ether (BADGE). TEM images of the BADGE SERS nanoprobes demonstrate an average particle diameter of ~60 nm and DLS measurements confirmed minimal aggregation after conjugation with an average particle diameter reading of 86.1 nm (Figure 24a,b). The ζ potential of the nanoprobes increased from -41.7 mV to -34.6 mV after the mixed SAM was formed, due to the presence of terminal amines on the PEG linker. After BADGE conjugation, epoxide groups replace the amines and the ζ potential decreased to -44.0 mV, indicating adequate particle stabilization

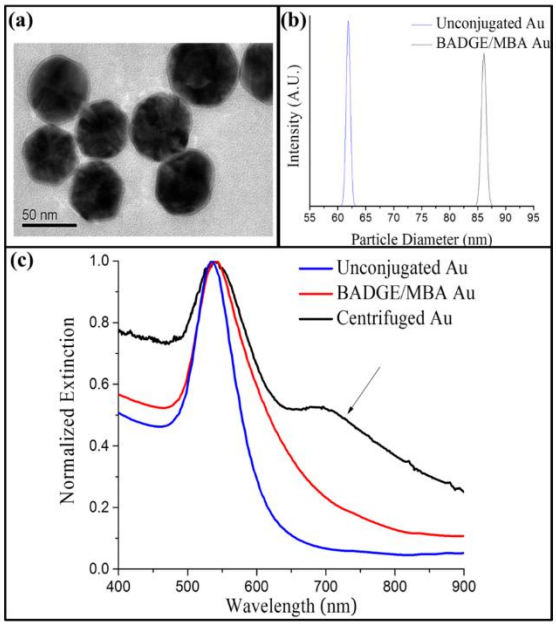

Figure 24. (a) TEM image of the conjugated gold nanoparticles; (b) size distribution of unconjugated gold (blue) and BADGE conjugated nanoprobes (black), measured by dynamic light scattering; (c) extinction spectra plotted versus wave-length for: unconjugated gold (blue), BADGE conjugated gold nanoprobes (red), and centrifugally aggregated nano-probes (black).[3]

was achieved sterically by the PEG, and electrostatically by the 4-MBA's terminal carboxylic acid group.[110, 118]

The intrinsic signal enhancement provided by a SERS substrate relies heavily on the excitation of localized plasmons at the metallic surface by the Raman excitation laser[23]. This excitation of plasmons causes a shift in magnitude in the metallic nanoparticle extinction spectra, dependent on the size and stability of the particles[28, 119]. The extinction profile is representative of the scattered light intensity as a function of excitation wavelength, and therefore serves as a predictor of the magnitude of the relative SERS enhancement. In Figure 24c, the localized surface plasmon resonance (LSPR) extinction band for unconjugated gold nanoparticles is shown to be at 535 nm. After BADGE conjugation, the LSPR of the nanoparticles is slightly red-shifted to 540 nm, which can be attributed to the resultant increased particle diameter. Maximal SERS enhancements are observed when the LSPR falls within a 240 nm window including both the excitation wavelength and Raman-shifted wavelength[25], specifically 780±120 nm for the excitation laser used in this work. To shift their LSPR into this window and achieve the SERS enhancements needed for nanomolar detection, the nanoprobes were aggregated by centrifugation and a secondary plasmon band at 700 nm becomes apparent in the extinction spectra, as indicated in Figure 24c.

The Raman spectra of the reporter molecule 4-mercaptobenzoic acid (4-MBA) in powder form, the SERS spectra of the nanoprobes suspended in solution, and the SERS spectra of the nanoprobes after centrifugal aggregation are compared in Figure 25. The strongest characteristic vibrational modes for 4-MBA occur at ~1075 cm^{-1} and 1586 cm^{-1}, corresponding to the C-H in-plane bending (β_{18b}) and C-C stretching (ν_{8a}) vibrational modes, respectively.[120-122] These bands are evident in the intrinsic Raman and nanoprobe SERS spectra (Figure 4),

and are comparable to those previously reported for 4-MBA bound to gold[52, 105, 109, 121, 123]. Weaker Raman modes seen in the powdered 4-MBA spectrum become visible in the SERS signal when the nanoprobes are aggregated (Figure 25). Though some peaks are shifted or broadened, the strongest peaks in the SERS nanoprobe signature correspond to the published vibrational modes for 4-MBA (Table 3).

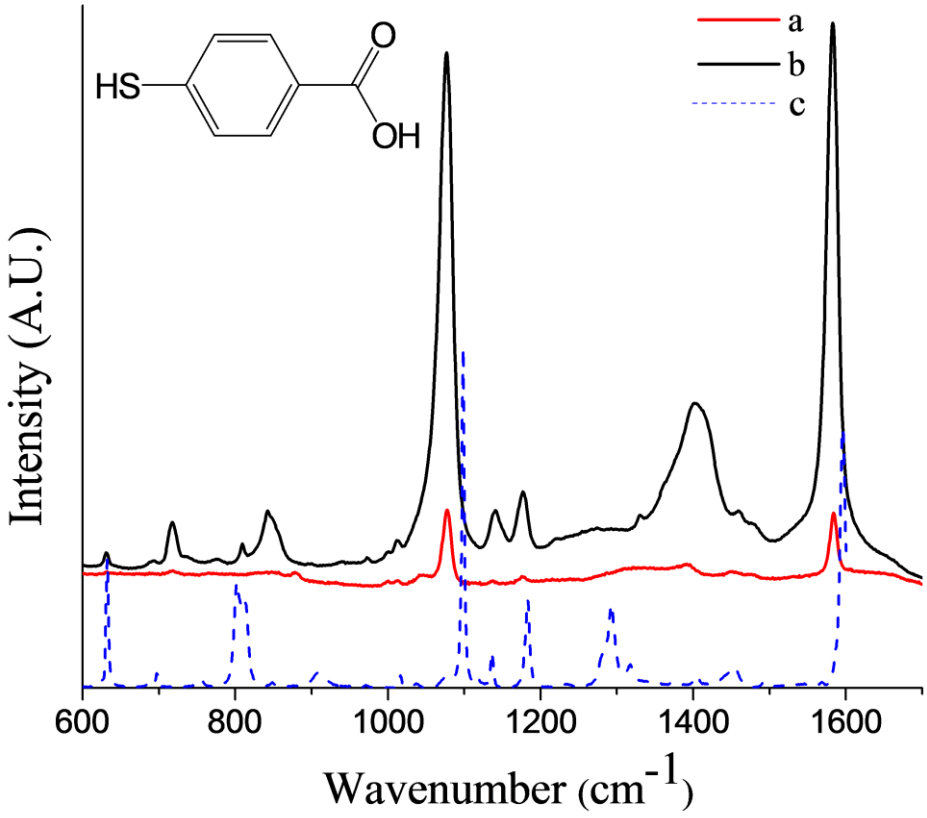

Figure 25. SERS signals of (a) 30 μL of nanoprobes suspended in solution and (b) 30 μL of nanoprobes aggregated by centrifugation, and (c) spontaneous Raman signal of the Raman reporter molecule (4-MBA) in powdered form. Inset: Chemical structure of 4-MBA[3].

Table 3. Assignment of 4-MBA vibrational modes (cm-1) from the BADGE/MBA nanoprobe SERS spectra[3].

Raman (cm^{-1})	SERS (cm^{-1})	Assignment
697	**718**	**γ(CCC)[123]**
812	**843**	**δ(COO-)[123]**
1099	**1075**	**β(C-H)[120-121]**
1136	**1141**	**β(C-H)[121]**
1183	**1177**	**β(C-H)[120-121]**
1318	**1330**	**ν_s(COO-)[123]**
1404	**1402**	**ν_s(COO-)[121]**
1596	**1586**	**ν(C-C)[120]**
δ = in-plane deformation, β = bending, γ = out-of-plane deformation, ν = stretching		

II.3.i.a Verification of competitive binding to aptamer using MST

The binding analytics of the SERS nanoprobe to the BPA aptamer were quantified by the aptamer:target dissociation constant K_d, as determined by microscale thermophoresis. The BPA-specific aptamer: 5'-CCG CCG TTG GTG TGG TGG GCC TAG GGC CGG CGG CGC ACA GCT GTT ATA GAC GTC TCC AGC-3'[124] has a predicted secondary structure as depicted by its M-fold diagram inset in Figure 26. Dilutions of the BADGE SERS nanoprobes, corresponding to 20 pM-800 nM of BADGE, were exposed to a constant 5 nM each of CY5 labeled BPA aptamer and nonspecific aptamer. The aptamer-nanoparticle binding curves are

shown in Figure 26, quantified as the fraction of the total solution concentration of fluorescent aptamer that is bound to SERS nanoprobes, as a function of total BADGE concentration present in the nanoparticle solution. The dissociation constant K_d was determined to be ~54 nM for the BADGE nanoprobes, in comparison to 10 nM reported for free BPA binding to the same aptamer[124]. Additionally, the K_d value for free BPA binding to the BPA aptamer was determined experimentally using MST to be ~100 nM (Figure 26), further validating the usefulness of the capture nanoprobe for future competitive binding assay development. The control experiment using a nonspecific aptamer was negative (Figure 26), demonstrating that the SERS nanoprobes are specific to the BPA aptamer.

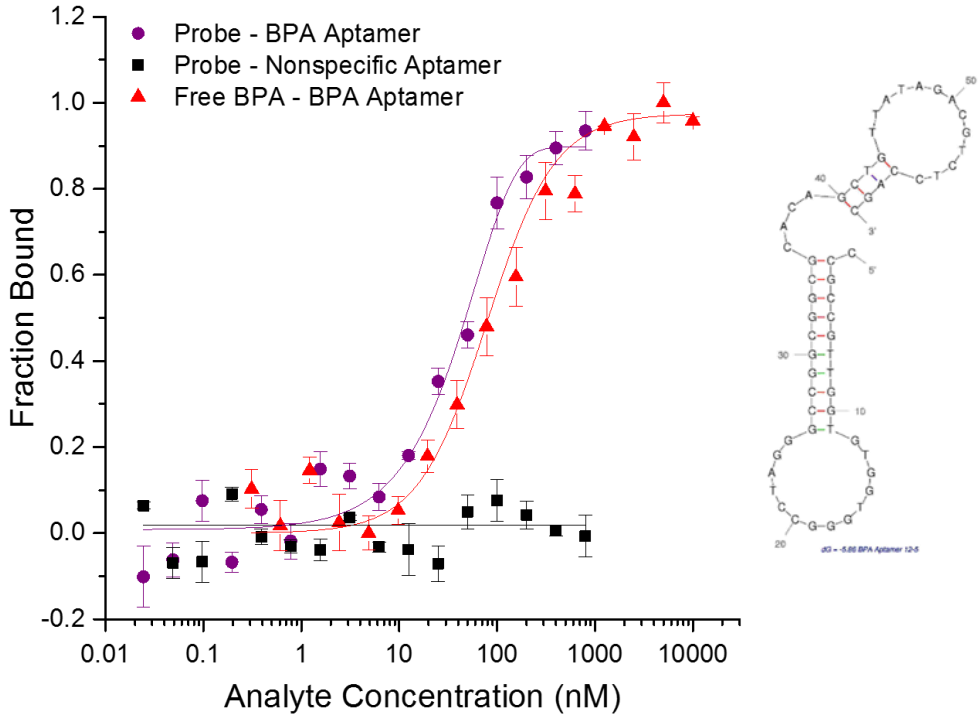

Figure 26. Binding behavior of the SERS nanoprobes to the published BPA-specific aptamer (red, K_d~ 54 nM, r^2=0.96) and a non-BPA specific aptamer (black) as measured by fluorescence microscale thermophoresis (MST). Comparing to binding curve for free aptamer to free BPA (K_d ~100 nM) this demonstrates competitive binding will occur between the probe and free BPA. *Inset:* BPA aptamer predicted secondary structure[3].

This results reveal an important design aspect for assays relying on nanoparticles coated with sensing ligands and/or analytes. The MST aptamer binding curve against free BPA had nearly double the dissociation constant than it did for immobilized BADGE, i.e., the aptamers had a stronger affinity for the probe nanoparticle than for free BPA. By providing multiple binding sites in a small concentrated area, the BADGE coated probe nanoparticle improves upon the relative binding *avidity* of the assay. The 100 nM K_d still describes the binding affinity, or strength, of a single aptamer-BPA interaction, yet condensing these individual binding events in a localized region through nanoparticle immobilization increases the likelihood of other binding interactions to occur. This happens because each aptamer binding event makes the probability of another binding event occurring nearby slightly less favorable (negative cooperativity) as a negatively charged aptamer is less likely to approach an area of the analyte coated particle where there is already a negatively charged aptamer nearby.

The 54 nM avidity describes the binding strength that comes from combined effect of all the affinities occurring in the colloidal suspension, and can be thought of as the functional affinity. This particular avidity is only valid for particles containing a total BADGE concentration of 800nM corresponding to ~80 BADGE molecules per 60 nM gold nanoparticle, and therefore would be shifted to stronger affinities (lower dissociation) by decreasing the number of analytes per probe nanoparticle. This subsequently shifts the dynamic range lower, so if a higher range were required, say for urinalysis rather than plasma, then one would want to increase the number of analytes per probe. Changing the number of analytes per probe is a catch-22 in that it requires a delicate balance between enough PEG-analyte to keep the particle stable in high salt environment and choosing the appropriate number of

ligands for the analytical range of interest. Alternatively, we could substitute mPEG for some portion of the PEG-analyte so that the number of analytes could be adjusted without sacrificing stability. Or one could simply change the size or type of the nanoparticle, though this would affect the net SERS enhancement as well and drastically change the response characteristics, and thus should be carefully considered if only looking for incremental shifts in range.

II.3.ii SERS analysis in micro- to nanochannel

A new SERS-on-a-chip device was developed to analyze the SERS nanoprobes competitively freed by the BPA assay described above. This chip features two microchannels connected by a nanochannel fabricated on a 500 µm thick polished borosilicate wafer (Mark Optics, Inc., Santa Ana, CA) using photolithography according to the scheme in Figure 27. The microfluidic portion of the channel is 150 µm in width and 1.0 µm in depth while the nanochannel is 50µm in width and 40 nm in depth. Therefore, gold nanoparticles greater than 40 nm in diameter will be trapped in the micro- to nanochannel junction, generating a controlled area of aggregation. The microchannel was patterned with wet HF etching and the nanochannel was patterned with a reactive ion etching process. This wafer will be bonded to a blank wafer etched with the nanochannel to seal the trenches and create the channels, with inlet holes created at the ends of the microchannel with a diamond drill bit. The channels were characterized using 5µL dilutions of the stock nanoprobes described in section II.3.i to determine the chips limit of detection in relation to the assay, time required to fill the constriction, and their ability to differentiate between low concentrations of the nanoprobes using SERS.

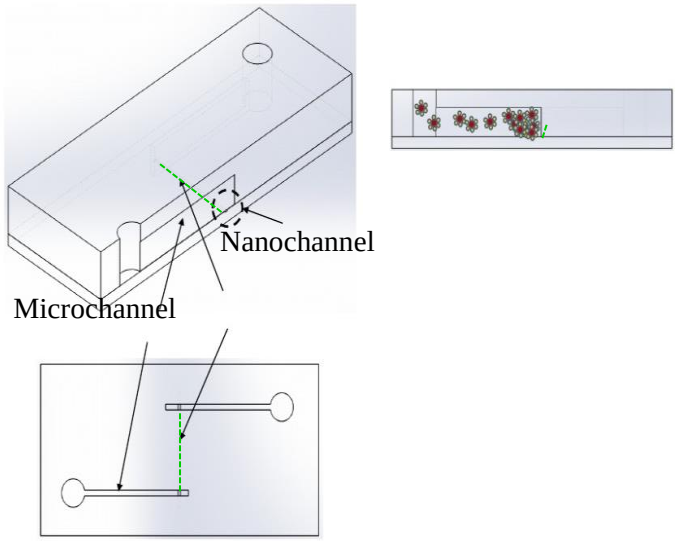

Figure 27. Schematic of the micro- to nano-fluidic SERS-on-a-chip device.

II.3.ii.a Toxin-functionalized Au-nanoprobe

Initial experiments to evaluate substrate variability were conducted using 50 µL of the nanoprobes in three different channels. As seen in Figure 28a there was extreme variability both within a chip and between chips, with inter and intra substrate variability at 20% and 45 % respectively. However examining the bright field images of the micro to nanochannel (Figure 28b) revealed too much gold aggregated in the channel, likely causing randomized hotspots to form. Additionally it took nearly 2 hours for the signal to saturate, far too long to compete with current lab-on-a-chip devices.

Next a second generation micro- to nanofluidic chip was developed, this time with both the micro and nanochannels channel widths set at 20 µm. Additionally only 5 µL of particles were used in the variability experiments. These changes resulted in a significantly improves %CV both with individual chips and across the lot (Figure 29a), and improved the SERS EF by 3x. Additionally the signal at the nano-channel junction was monitored as a function of time

to determine the signal saturation point, which occurred much quicker than the larger channel after only ~45 min (Figure 29c). Promising as this seemed, we were unable to obtain any quantifiable data, and the yield of successfully bonded channels per wafer was often lower than 20%, making fabrication lengthy and difficult with little to no reward. Therefore, it was decided that the assay products instead be analyzed by simply concentration by centrifugation, as discussed further in the next section.

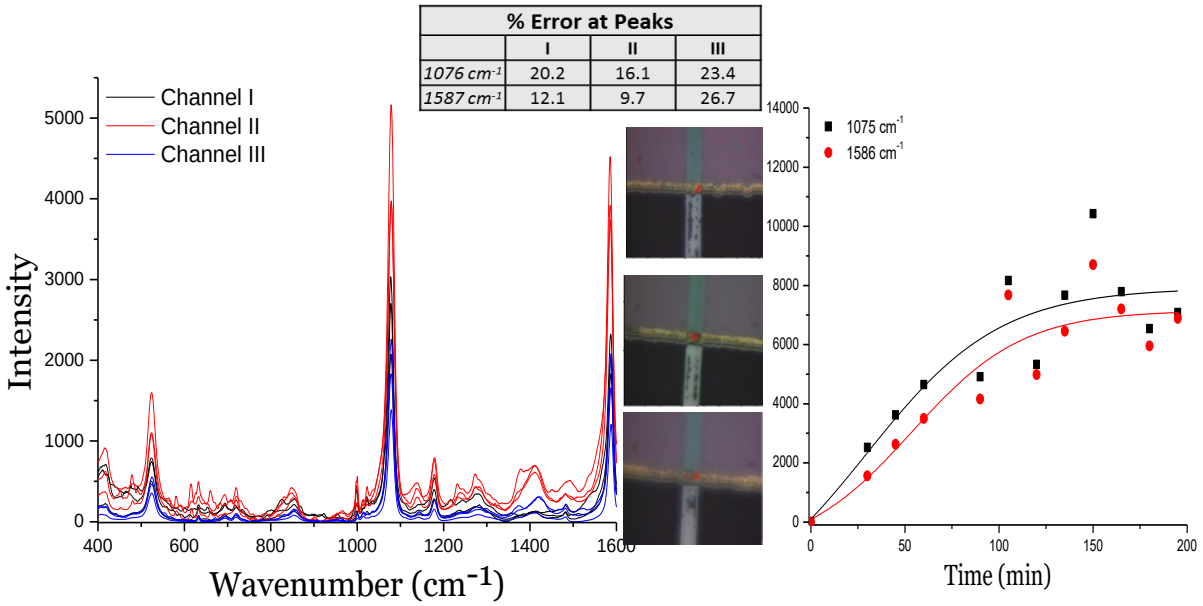

Figure 28. a) Variability across three separate micro- to nanochannel SERS-on-a-chip devices. b) Brightfield images at 50x objective showing particles aggregating far outside the defined sensing region. c)Time to SERS signal saturation determined to be ~2 h.

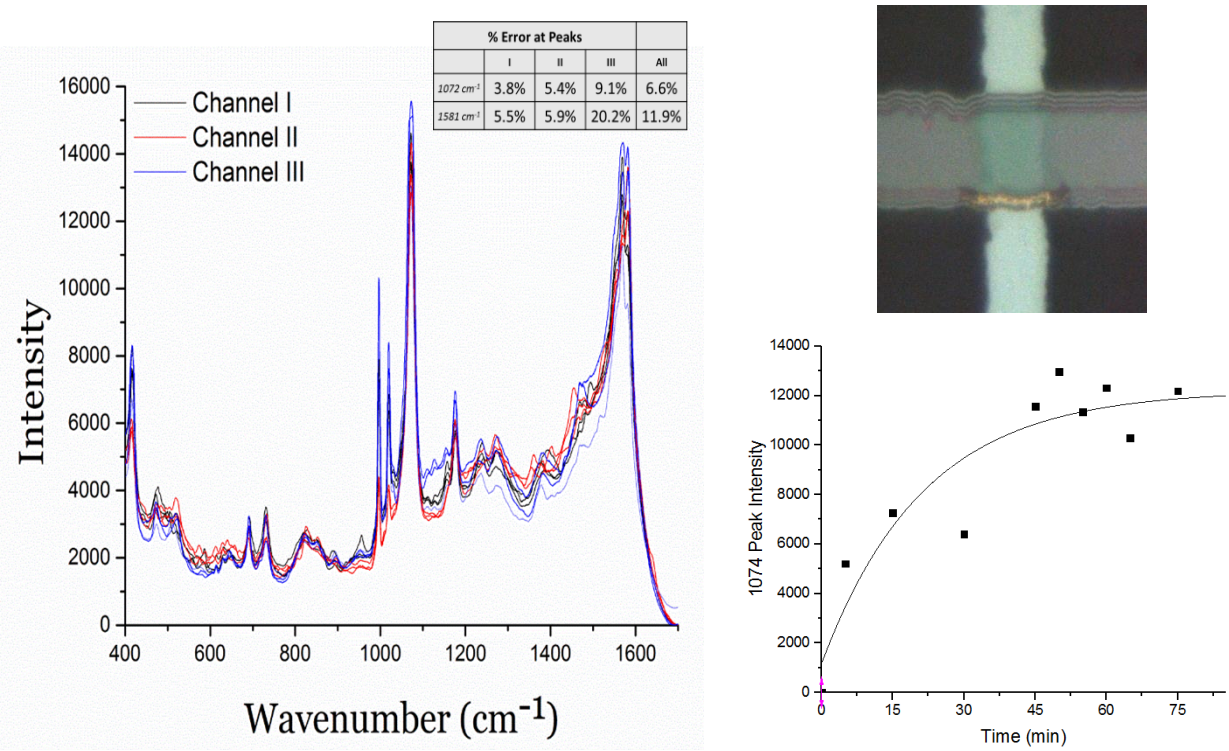

Figure 29. a) Variability across three separate 2nd generation micro- to nanochannel SERS-on-a-chip devices. b) Brightfield images at 50x objective showing particles aggregating within the defined sensing region. c)Time to SERS signal saturation determined to be ~45 min.

II.3.iii SERS analysis of "SERS On" assay using centrifugal aggregation

II.3.iii.a Toxin-functionalized Au-nanoprobe assay product

The stock nanoprobe concentration was the lowest detectable concentration using SERS in solution phase. Therefore, ten serial dilutions of the capture nanoprobes were centrifugally aggregated, dried, and their SERS spectra monitored to investigate the detection capabilities of the nanoprobes at the concentration range of interest. (Figure 30a). Features assigned to the SERS nanoprobes' Raman reporter (4-MBA) dominate the spectra, until the concentration drops below ~10 nM and the area of aggregation becomes smaller than the laser spot size of 3.1 µm. At this point, peaks attributable to the polypropylene centrifuge tube background begin to dominate the spectra, while the SERS nanoprobe characteristic peaks at

~1075 cm^{-1} and 1586 cm^{-1} decrease until they are no longer distinguishable after six serial dilutions (~1.10 nM, Fig 5a). The strongest polypropylene modes can be seen at 809 cm^{-1} and 841 cm^{-1}, corresponding to the C-C-C in-plane ring deformation (α_1)[125-126] and C-H out-of-plane bending (γ_{10a})[126-127] vibrational modes, respectively.

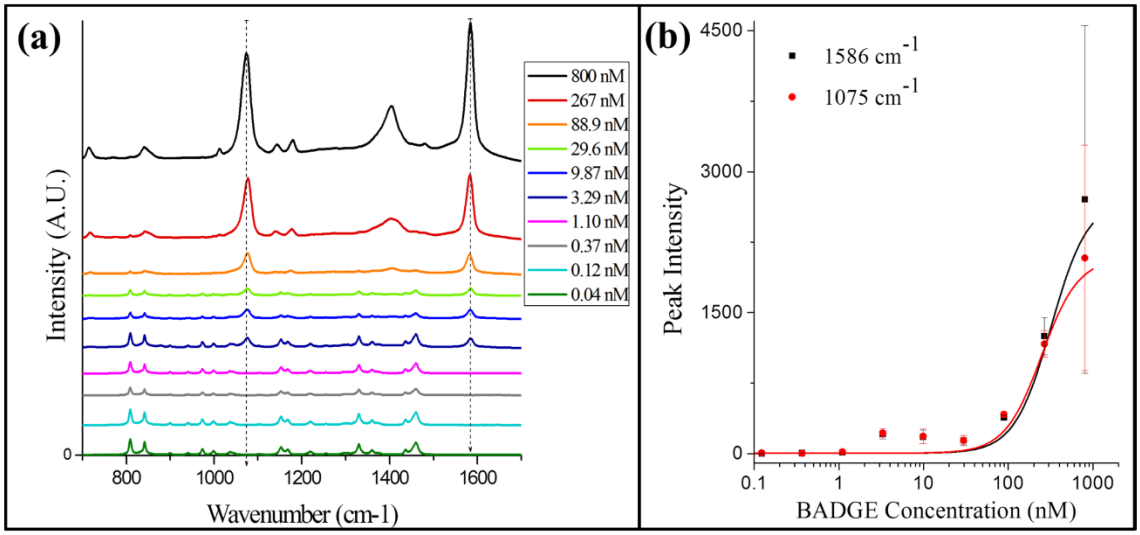

Figure 30. a) SERS signals of 100 µL of centrifugally aggregated nanoprobes at 10 concentrations ranging from 40pM-800 nM, offset for clarity. b) SERS intensity of the vibrational modes at 1075 cm-1 and 1586 cm-1 with increasing volume of nanoprobes[3].

The SERS peak intensities of the vibrational modes at 1075 cm^{-1} and 1586 cm^{-1} as a function of concentration are shown in Figure 30b. The trend follows a typical dose-response curve, where the MBA peaks can be identified with a coefficient of variation < 25%, until the nanoparticle concentration drops below 600 fM (3.29 nM BADGE). This sensitivity is competitive with the quantification limits previously reported for the detection of BPA levels in human blood utilizing LC-tandem mass spectrometry, ranging from 0.43 nM[128] to 64 nM[129]. It is noted that the standard error increases with increasing concentration, likely due to the nonhomogeneous nature of the aggregate formed using this method. For lower concentrations,

centrifugation causes the small volume of particles to distribute evenly on the bottom of the tube. However for higher volumes with a visible precipitate, a higher density of nanoparticle junctions[119] is formed, resulting in more areas of increased SERS enhancements[23].Therefore, the analytical range for this method is ~3-300 nM. Though this detection method for true quantitative analysis is impaired by high error from “hot spots”, this proof of concept study demonstrates that limited concentration information may be obtained using SERS through the controlled aggregation of nanoparticles combined

The limit of detection can be reduced and the analytical range shifted to suit a specific BPA-aptamer assay through altering the ratio and amount of PEG linker and Raman reporter molecule conjugated to each particle. Modifying the amount or type of RRM directly effects the SERS signal intensity, while adjustments made to the PEG linker can be used to modify the distance between the particle and analyte, to reduce charge based interactions with the nanoparticle surface, or to alter the number of target analyte molecules per particle[114]. The binding affinity of the aptamer to the functionalized SERS nanoprobes may also be adjusted by changing the BPA derivative[130], or synthesizing a BADGE derivative with only one epoxy group so that its structure more closely resembles BPA.

II.4 A new potential modality: SERS by magnetic aggregation

As it has become apparent that mechanical aggregation of nanoparticles produces too much variability in the hot spot formation, even then the RRM is evenly coated on the NP surface prior to aggregation. In an attempt to achieve more reproducible, and even reversible, nanoparticle aggregation, this section discusses the potentials of *magnetic* based aggregation. To test this new method Fe3O4 core/SiAu shell functionalized SERS nanoparticles were developed (Figure 31).

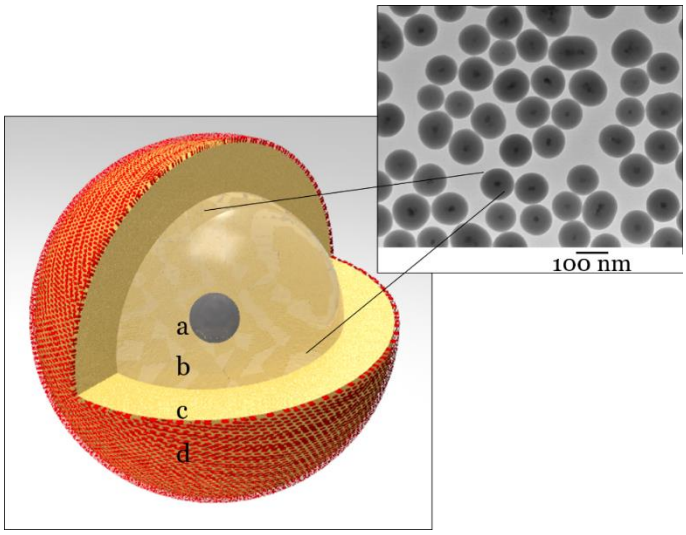

Figure 31. Structure of the AuSiFe SERS nanoprobe: a) 17 nm Fe3O4 Core b) 110nm Silica Shell c) 48 nm Au Shell d) 4-MBA SAM. *Inset:*TEM of silica coated Fe particles before gold shell is applied.

The ~175 nm total diameter magnetite core gold nanoshell particles are composed of four layers: 1) 17 nm Fe3O4 Core 2) 110nm Silica Shell 3) 48 nm Au Shell 4) 4-MBA SAM. The core/shell ratio of the particles was tuned so that their maximum extinction peak shifts towards the laser wavelength 785 nm as depicted in Figure 32a. The Raman reporter molecule, 4-mercaptobenzoic acid (MBA), was bound to the gold shell using a self assembled monolayer (SAM). Uniform orientation of the reporter molecules relative to the surface of the nanoparticle

avoids nonspecific adsorption, while providing increased sensitivity and particle stability. SERS spectra of the particles with MBA suspended in solution indicate uniformity, with a total coefficient of variation of 10.5% across 9 scans (Figure 32b).

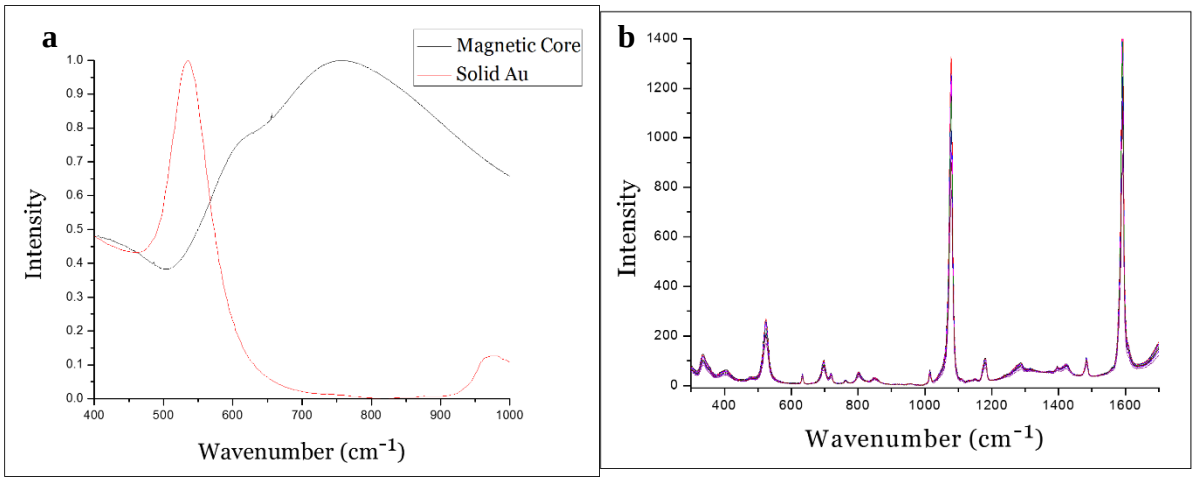

Figure 32. a) Extinction spectra of AuSiFe nanoprobes compared to solid old. b) 9 replicates of the AuSiFe SERS profile taken in a wellplate, displaying peaks indicative of MBA.

In the first magnetic chip design iteration depicted in Figure 33, particles flow down a narrowing channel to a detection region where they are aggregated by a permanent neodymium magnet embedded in PDMS below the sensing region. Channels were treated with a Pluronic F-108 surfactant to promote flow and reduce clogging outside of the detection area.

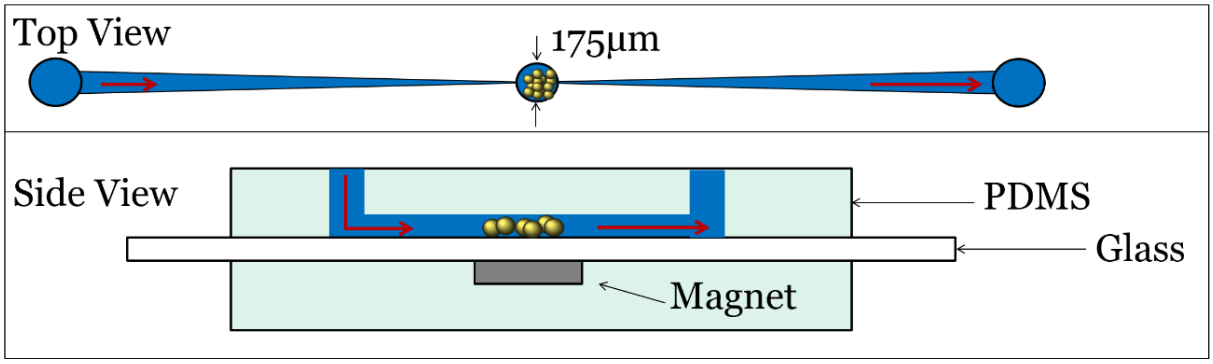

Figure 33. Schematic diagram of the first iteration of magnetic SERS-on-a-chip.

The inset bright field image in Figure 34 shows 25 µL of nanoparticles aggregated in the optofluidic channel over the embedded magnet, at a concentration of $3x10^9$ particles/mL (0.1 mg/mL). The coefficient of variation of the SERS signal between nine scans taken randomly across the area of aggregation was 12.1%, where full spectra are shown in Figure 34. The IR-tuned magnetic core-shell particles provide increased SERS enhancements, can be immobilized magnetically, and demonstrated uniformity in solution with an error <11%. The magnetic SERS platform provides reproducible spectra (12.1 %CV) across the area of particle aggregation at microliter volumes. Next, the target analyte BPA will need to be conjugated to a magnetic nanoparticle using a heterobifunctional polyethylene glycol spacer as was done with the gold nanoprobe. Once characterized, the functionalized particle's binding affinity to BPA aptamers will need to be analyze before magnetic SERS can be validated as a potential aggregation mechanism.

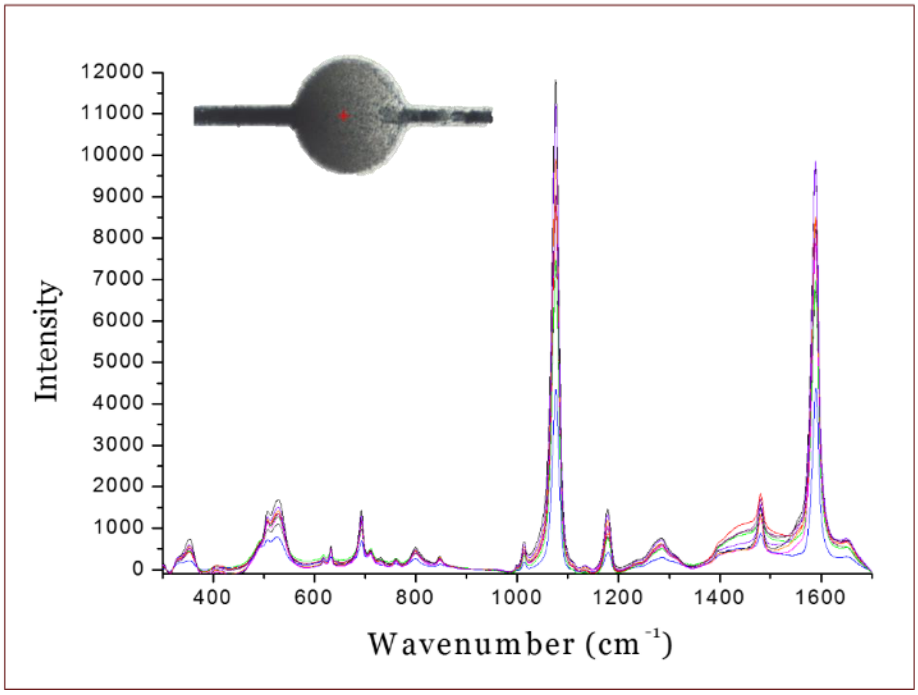

Figure 34. Variability in SERS spectra from the AuSiFe NPs across the magnetic SERS-on-a-chip device using 780 nm excitation.

II.5 Final thoughts on SERS modality selection

This chapter details the first report of the successful design of a functionalized SERS nanoparticle for specific binding to a BPA aptamer with an affinity similar to that of the analyte in free solution. The particles provide a characteristic Raman signature which can be enhanced through nanoparticle aggregation and detected by SERS at concentrations as low as 600 fM. The nanoprobes demonstrate colloidal stability for biological interaction while providing functional conjugation to the BADGE analyte. The aptamer/nanoprobe binding event is characterized through microscale thermophoresis fluorescence measurements and quantified by a dissociation constant of 54 nM. This demonstrates the sensitive aptamer recognition capabilities of capture analytes immobilized onto SERS active nanoparticles with minimal perturbation of the aptamer's native, free-analyte binding. However truly quantitative data was not able to be obtained by mechanical aggregation, as was found earlier in the chapter, and therefore *magnetic* induced aggregation of assay particles will be explored in the next chapter.

CHAPTER III

A NEW SERS COMPETITIVE BINDING ASSAY UTILIZING APTAMER-MEDIATED NANOPARTICLE ASSEMBLY

III.1 Introduction to molecularly-mediated SERS assays

Molecularly mediated surface enhanced Raman spectroscopy (SERS) can be a desirable approach for ultrasensitive blood biomarker detection due to its high sensitivity and capability for multiplexing. As hypothesized in Figure 35 by Chen et al[4] core-satellite assemblies (CSA) formed as a result of molecular recognition event allows for localized SERS hot spots of enhancement that can be controlled without irreversibly aggregating nanoparticles. SERS analysis of DNA-directed nanoparticle assembly using functionalized colloidal nanoparticles has been used extensively as a method to measure and control the degree of enhancement of Raman scattering from a Raman active dye in response to a molecular binding event.[131-132]

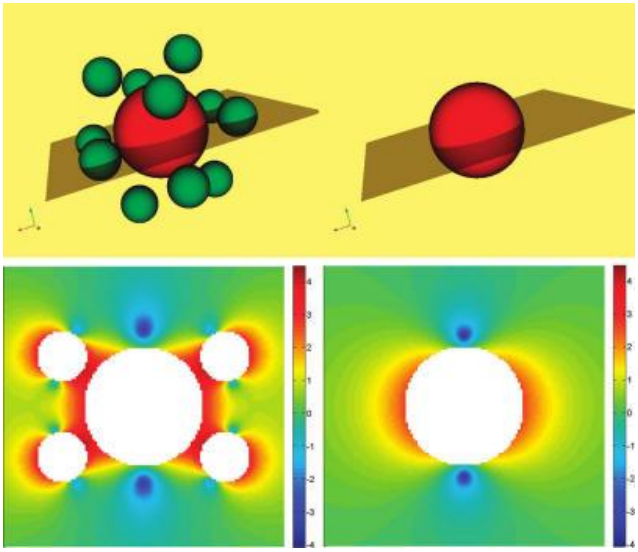

Figure 35. Modeled electromagnetic enhancement of CSA (left) and isolated 50 nm sphere (right). (Top) Planes in 3D views of structures identify location for which enhancements are displayed. (Bottom) E^4 enhancement for CSA and isolated sphere (log scale). The polarization direction of the incident field is parallel to the horizontal coordinate. Reprinted with permission from Chen et al.[4] Copyright 2009 American Chemical Society.

SERS assays in both "turn-on" and "turn-off" formats have been developed using oligonucleotides to detect DNA fragments,[59] as well as with aptamers for the detection of biomarker proteins.[133-134] DNA aptamers are simpler and more economical to produce at large scale, are capable of greater specificity and affinity than antibodies, are easily tailored to specific functional groups, can be used to tune inter-particle distance and shift the LSPR, and their intrinsic negative charge can be utilized for additional particle stability.[135,84]

III.2 Design & fabrication of aptamer-mediated nanoclusters

In this chapter, a "turn-off" competitive binding assay platform involving two different plasmonic nanoparticles for the detection of the toxin bisphenol A (BPA) using SERS is presented. A derivative of the toxin is immobilized onto a silver coated magnetic nanoparticle (Ag@MNP), and a second solid silver nanoparticle (AgNP) is functionalized with the BPA aptamer and a RRM (MGITC) capable of providing SERRS enhancements at 532 nm. The capture (Ag@MNP) and probe (AgNP) particles are mixed and the aptamer binding interaction draws the nanoparticles closer together, forming an assembly that results in an increased SERS signal intensity. This aptamer mediated assembly of the two nanoparticles results in significant enhancement of the SERS signal intensity from MGITC compared with the target particle alone. These pre-bound aptamer/nanoparticle conjugates were then exposed to BPA in free solution and the competitive binding event was monitored by the decrease in SERS intensity. A schematic representation of this aptamer-mediated "SERS-off" assay and preliminary spectral data supporting the assay platform are shown in Figure 36.

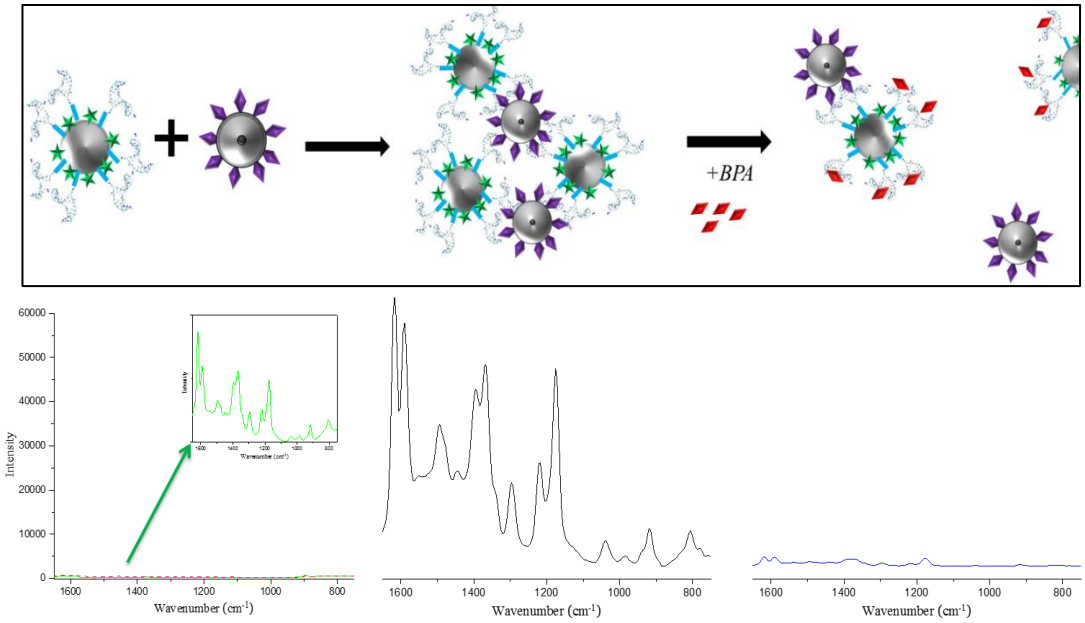

Figure 36. Assay schematic: target nanoparticles exhibit SERRS from MGITC -> when mixed with probe particles, assay nanoclusters form and the SERS signal is 'turned on' -> when BPA is introduced, the SERS signal is 'turned off'.

III.2.i Probe and Target particle conjugation

The target nanoparticle is comprised of silver nanoparticles coated in PEGylated BPA aptamer and the Raman reporter MGITC. The probe particle was functionalized with BADGE using the same conjugation method as described in chapter II, excluding the RRM MBA, where a dye resonant ~532 nm was chosen instead for this configuration and was moved to the non-magnetic silver target. Chemical drawings of the particle conjugation chemistry can be found in Figure 37.

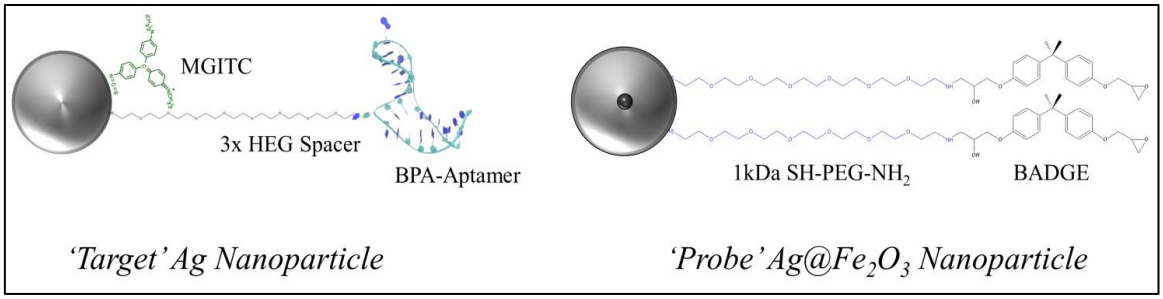

Figure 37. Conjugation chemistry for the target and probe "SERS off" BPA assay nanoparticles.[1]

III.2.i.a Probe: core comparison- Fe_2O_3 vs Fe_2CoO_4

Two different ferrite cores were investigated for the magnetic probe particle. Silver-coated cobalt-ferrite nanoparticles ($Ag@Fe_2CoO_4$) were prepared by first synthesizing a stock solution of the core Fe_2CoO_4 nanoparticles through co-precipitation of iron(III) chloride (0.2 M FeCl3) and cobalt(II) chloride (0.1 M CoCl2) in sodium hydroxide solution at pH ~12 (3.0 M NaOH) using a method modified from Rutirawut *et al.* [136] The cobalt ferrite salt solution was added rapidly into 3.5 M NaOH solution under vigorous stirring, then headed at 80°C for 1 h. The cobalt-iron oxide precipitated colloid was washed with deionized water in triplicate using a permanent neodymium magnet. To coat with silver, 500 µL of these stock MNPs was mixed with 4 mL of 0.35 M glucose and 1.5 mL of 60 µM $AgNO_3$. The solution was sonicated for 10 min then heated to 90 °C for 90 min. Finally, the particles were centrifuged three times to wash, and finally redispersed in 6 mL of 5 mM sodium citrate.

Silver-coated ferrite nanoparticles ($Ag@Fe_2O_3$) were prepared using a co-precipitation method for the synthesis of the particle core and glucose reduction to coat with silver as described by Kumar *et al.*[137] and Mandal *et al.*[138] respectively. Briefly, a stock solution of maghemite (γ-Fe_2O_3) nanoparticles was prepared by adding 25 mL of an acidified iron salt solution (0.4 M Fe^{2+}, 0.8 M Fe^{3+}, 1 M HCl) drop-wise to 250 mL of 1.5 M NaOH at 50 °C

under vigorous non-magnetic stirring. After 20 min the particles were allowed to cool, washed twice with DI water and once with 0.1M HNO_3. An additional 125 mL of HNO_3 was then added to the solution, stirred an additional 40 min at 95 °C, and resuspended in distilled water. To coat with silver, 1 mL of these stock MNPs was mixed with 4 mL of 0.35 M glucose and 1.5 mL of 60 μM $AgNO_3$. The solution was sonicated for 10 min then heated to 90 °C for 90 min. Finally, the particles were centrifuged three times to wash, and redispersed in 6 mL of 5 mM sodium citrate.

To synthesize 1 mL of BADGE functionalized magnetic nanoprobes, the SH-PEG-NH_2 linker was added drop-wise to an excess of the analyte BADGE in 0.3 M PBS buffer (pH 8.5) and left overnight to allow conjugation between their terminal amine and epoxide groups respectfully. The conjugates were then treated with aminoethanol to open unbound epoxide rings and prevent non-specific binding of BADGE to the RRM's amine groups. These SH-PEG-BADGE conjugates were then added at a 5000:1 ratio to 1 mL of silver coated magnetic nanoparticles (stocks diluted to 225 pM). After 1 h three 20 μL aliquots of 250 mM citrate HCl buffer were again added 5 min apart, and the sample was left an additional 30 min before centrifuging and resuspending the BADGE functionalized particles in 1 mL of 0.1 M PBS (pH 7.4).

As shown from the TEM images and DLS plots in Figure 38, the average particle diameter for the Ag@Fe_2CoO_4 particles was 63 nm and final stock concentration was 385 pM as determined by NTA. For the probe 1, Ag@Fe_2O_3, particles the hydrodynamic particle diameter as determined by DLS was ~70 nm and final concentration of 425 pM was determined

by NTA. The extinction profile of plain AgNPs compared to the magnetic core-shell particles (Ag@ Fe_2CoO_4 and Ag@ Fe_2O_3) are shown on the right in Figure 38 for reference.

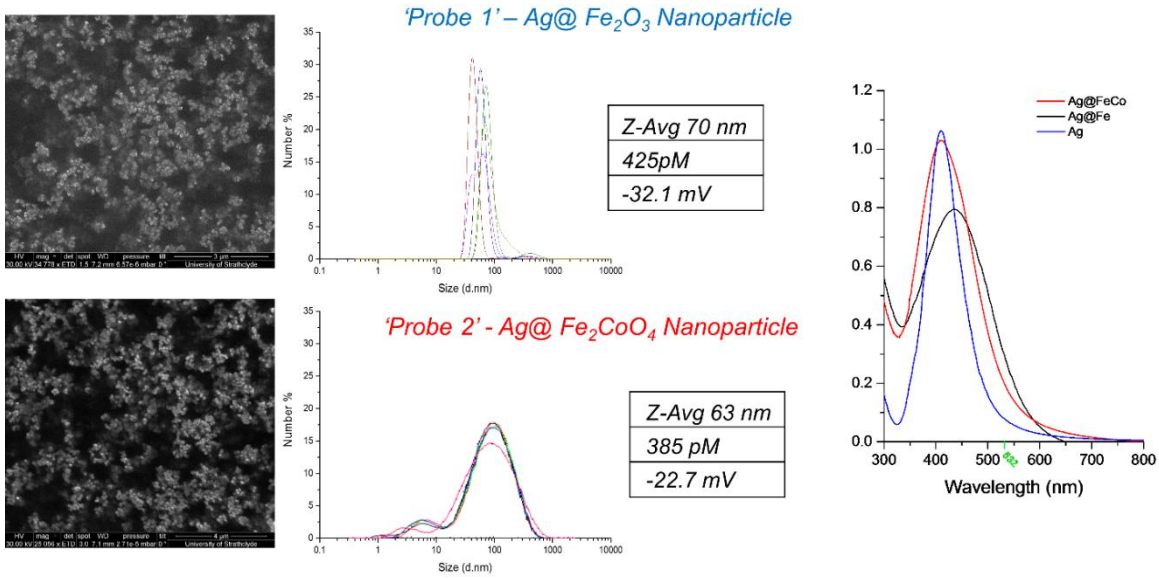

Figure 38. TEM images of the two probe nanoparticles *Center:* DLS size distribution and zeta potential data demonstrating particle size and stability *Right:* Comparison of the extinction profile of Fe (black) and FeCo (red) core nanoparticles after coating with silver. The spectra for plain AgNPs used as the target nanoparticles is shown for reference[2].

A colloid's zeta potential (ζ) is indicative of the relationship between the particles' surface charge and their ionic environment, and thus can be used to predict long term stability. Silver coated probe particles of the Fe_2O_3 and Fe_2CoO_4 varietals coated in PEGylated BADGE were found to have zeta potentials of -32.1 mV and -22.7 mV respectively (Figure 38), indicating that the PEG spacer and the HEG modified aptamer provide adequate particle stabilization in the 0.1 M PBS binding buffer, but that the Co doped particles were slightly less stable.

III.2.i.b Target: utilizing SERRS for colloidal assays

Silver colloid (AgNP) was synthesized using the 'cold' method reported by Leopold and Lendl.[139] Hydroxylamine hydrochloride (1 ml, 150 mM) was added to 89 mL of NaOH (3.33 mM) under vigorous stirring. Silver nitrate ($AgNO_3$) solution (10 mL, 10 mM) was added drop-wise and stirred for 15 min at room temperature. Dynamic light scattering (DLS) measurements revealed an average particle diameter of ~45 nm (not shown) with a PDI index of 0.133. The stock particle concentration was determined to be 225 pM according to Beer's Law using an extinction coefficient of 2.87×10^{10} M^{-1} cm^{-1} at 404 nm.[140]

Prior to immobilization, the BPA aptamers were suspended in a 60 mM phosphate buffer (PBS, pH 8.5) and treated with 15 mg of dithiothreitol (DTT) to reduce their disulfide bonds. After 1 h the aptamers were purified using a Nanoseps 10kDa desalting column to remove residual DTT, washing three times in 0.1 M PBS pH 7.4. The aptamers were then heated to 90 °C for 5 min to allow any cross-linked DNA to dehybridize, then allowed to cool at room temperature for 15 min to allow sufficient time for the aptamers to fold into their tertiary structure at their strongest folding temperature of T = 54.1 °C.

Target AgNPs were functionalized with aptamers using a modified method developed by Zhang et al.[141] The aptamer (80 µM) was added to 1 mL of silver colloid (225 pM) at a molar ratio of 2000:1 and left shaking for 1 h. Three 20 µL aliquots of 250 mM citrate HCl buffer (pH 2.9) were then added 5 min apart, and the sample was left an additional 30 min before centrifuging and resuspending the aptamer functionalized particles in 1 mL of 0.3 M PBS (pH 7.4). The Raman reporter molecule, malachite green isothiocyanate (MGITC, 10 µM in methanol), was then added at a 500:1 ratio and left to react with the aptamer AgNPs under sonication for 1 h, which were then centrifuged and stored in a 0.1 M PBS buffer (pH 7.4).

Malachite green isothiocyanate (532 nm) was chosen as it is a chromophore capable of exhibiting SERRS with a 532 nm excitation source (Figure 39). The Ag target nanoparticles were functionalized with aptamers and MGITC as described and yielded an average ζ of -39.7 mV, where ζ > -20 mV, and as shown in Figure 39 their extinction spectra shifts but is not broadened as a result of aggregation in a high salt environment, indicating sufficient colloidal stability.

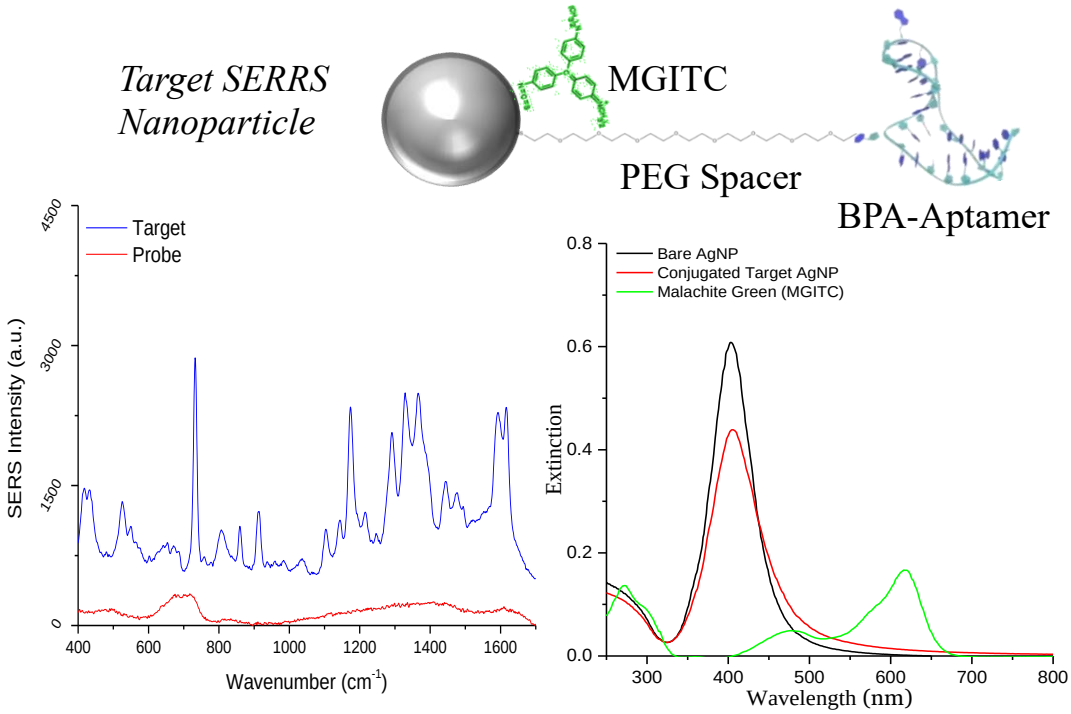

Figure 39. Raman spectra (left) of the silver target nanoparticle compared to the BADGE functionalized magnetic probe. Extinction profile of plain silver colloid compared to functionalized target nanoparticles and malachite green, which is shown to exhibit resonance Raman enhancement for excitation sources from 500-700 nm.

III.2.ii Monitoring the formation of assay nanoclusters

All wellplate measurements were collected using a 384-wellplate the Thermo-Scientific DXR Raman (600 with a spectral range from 400-1800 cm^{-1} in a total volume of 30 µL in 0.1 M PBS (pH 7.4) buffer with a 532 nm laser power of 10 mW and an integration time

of 10 s (10 x 1 s exposures). A solution containing equal volumes of 225 pM of each of the target and probe nanoparticles was monitored with SERS for 5 h to allow complete binding between the immobilized BPA aptamers and BADGE under stagnant conditions. The bound assay particles were then exposed to varying concentrations of BPA, and a second set of assembled nanoparticle clusters were collected using a neodymium magnet held at the side of a glass vial, the supernatant containing any unbound AgNPs was removed, and the assembled nanoparticles were resuspended in 0.1 M PBS (pH 7.4). The assays response was compared for both experimental set ups (wash or no wash) to demonstrate the importance of the magnetic washing steps in determining the dynamic range, and to make a case for using the assay in a microfluidic chip to automate the washing process. Finally the precision and accuracy of the wellplate BPA SERS assay are discussed and the limits of the sensor in this platform was determined.

While both of the ferric magnetic probe cores were tested, the SERS signal of a stock solution of the assembled nanoparticles and their sub sequential response to the presence of competing BPA was analyzed in a microwell using the smaller and more stable Ag@Fe_2O_3 particles, as the Co doped particles fell out of solution too quickly and were too heavily influenced by magnetics within the Raman microscope stage. As shown by Figure 40a, the SERS signal of the reporter molecule MGITC increases by 25 orders of magnitude as it experiences an enhancement in the electric field intensity of its immediate environment due to the aptamer-binding induced particle aggregation, reaching a steady-state equilibrium after ~ 2 h. For both types for ferric probes, it was confirmed using DLS that this SERS enhancement was indeed the result of the formation of nanoparticle assemblies facilitated by the aptamer binding to BADGE (Figure 40b). The nanoclusters appear to have a relative hydrodynamic

diameter of 100-200 nm meaning the clusters are likely something like ~4 nanoparticles each. However, as shown in Figure 41, only the plain Fe core based assay was able to repeatably produce the same 'SERS On' behavior across three separate batches of assay nanoparticles.

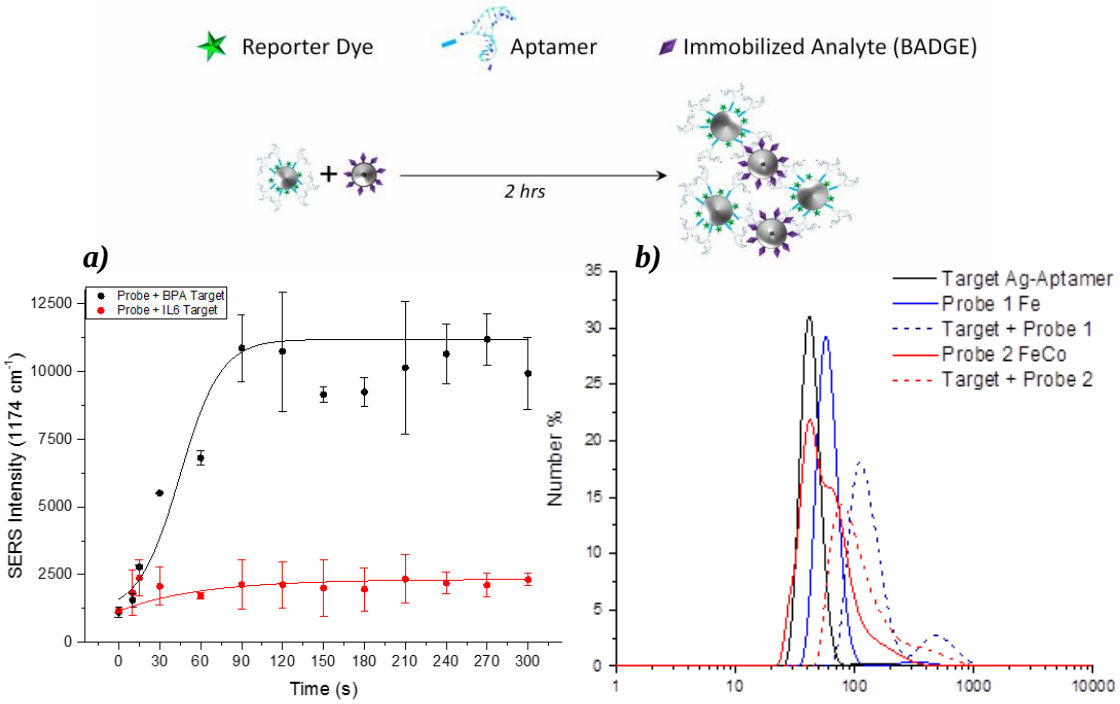

Figure 40. a) SERS spectral intensity from target nanoparticle, conjugated to either a BPA specific or a nonspecific aptamer sequence, monitored for 5 h after exposure to the Ag@Fe probe nanoparticles at a 1:1 molar ratio. b) Validation by DLS that SERS enhancement facilitated by nanoparticle assemblies for both probe types.

Additionally the UVV data showing the extinction spectra of the individual target and probe particles overlaid with the nanoparticle assembly is shown in Figure 41, and is consistent with the results of Mirkin et al[44] that indicate a cluster formation of ~4 nanoparticles (see Figure 35). Therefore, it is confirmed that Fe core particles are superior to FeCo core particles for liquid phase type assay analysis, and the assembled nanoclusters with the properties shown in Figure 41 will be the stock solution tested against BPA from here to the end of this dissertation.

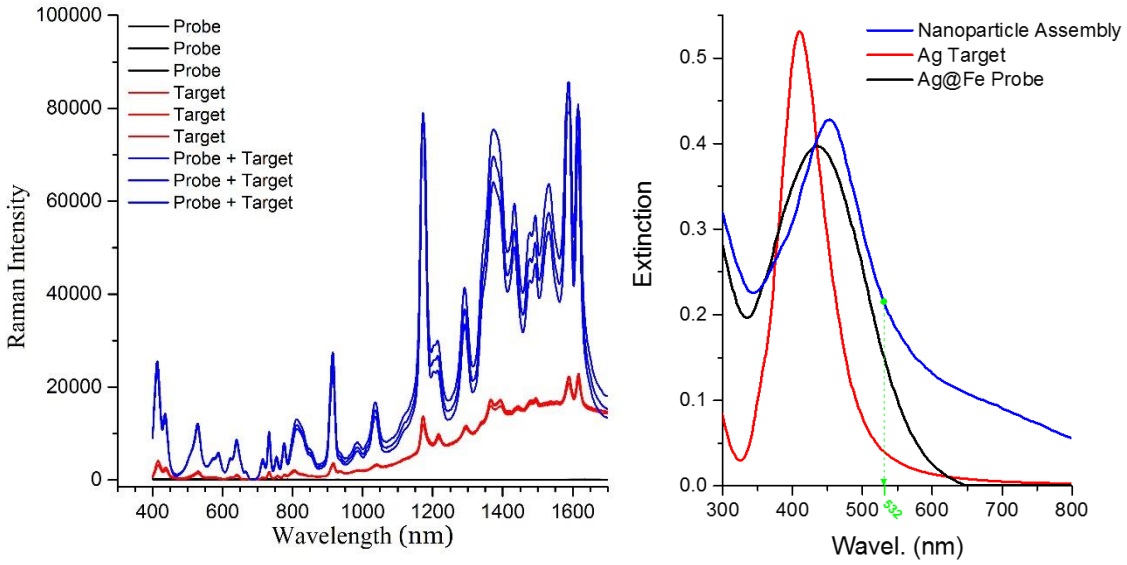

Figure 41. *Left:* Validation that the assay nanocluster is repeatable across three separate lots. *Right:* Verification of nanocluster formation by UV-vis, where red-shift implies aggregates have formed, and the excitation laser line is marked.

III.3 Monitoring the 'SERS Off' competitive binding assay in a traditional wellplate

To monitor competitive binding with SERS, 20 µL of the assay clusters were mixed with 10 µL of BPA (1 pM to 1 µM) in 0.1 M PBS (pH 7.4) and SERS measurements were taken every 30 s for 10 min. When free BPA is added to the assay nanoparticle assembly solution it competes with the BADGE immobilized on the surface of the probe particle for the aptamer binding sites on the target particle (Figure 42a). This dissociation is visualized by the SERS intensity of the peak at 1175 cm^{-1} (aromatic C–H bending vibrational mode,[142] Figure 42b) which decreases to a steady state over the course of ~3 min as competitive binding occurs (Figure 42c). This implies that the BPA aptamer immobilized on the target AgNPs must 'loosen' (increased net inter-particle distance) or is completely released from the BADGE on the probe MNPs in order to more favorably bind to free BPA. This causes a decrease in the solution SERS signal due to MGITC being displaced further from the nanoparticle surface

interface. Ten scans were averaged for each concertation and the experiment was repeated twice using two different batches of assay nanoparticles (Figure 42d). The signal response to BPA was quantifiable and repeatable as hypothesized and the performance metrics of the sensor are discussed later on within this subsection.

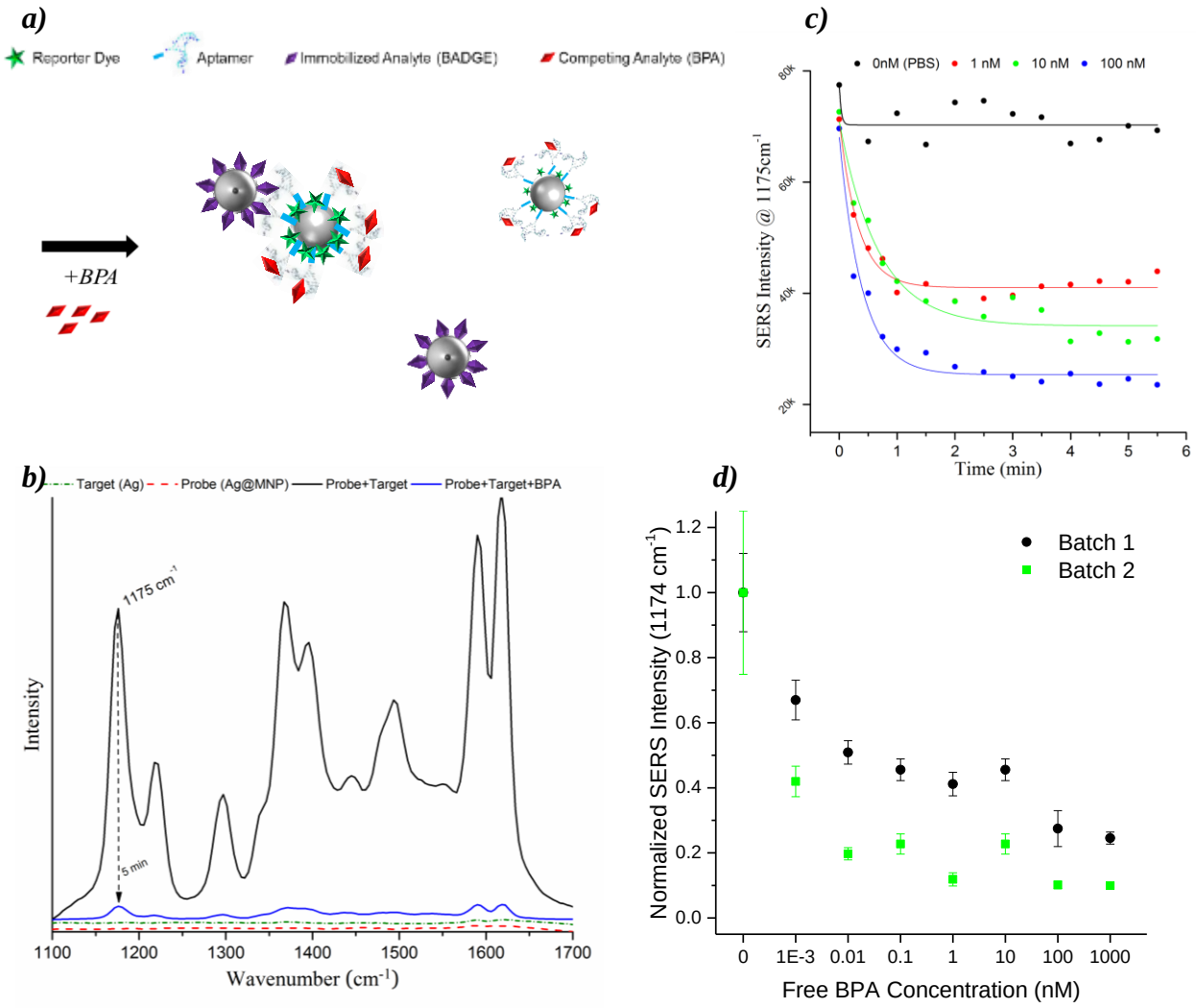

Figure 42. a) Schematic of nanocluster dissociation in the presence of the analyte BPA. b) Corresponding SERS spectra of the target and probe nanoparticles, and nanoclusters before and after the addition of BPA. c) Nanocluster assay response after exposure to 0-100 nM of the competing analyte BPA in free solution as a function of time. d) SERS peak Intensity at 1175 cm^{-1} as a function of concentration for two separate batches of assay particles.

II.3.i Effect of magnetic wash step on assay dynamic range

The physiologically relevant concentration range for BPA is reported as ranging from 0.05 to 150 ng/mL, or ~200 pM to 650 nM. From looking at the SERS response concentration dependence in Figure 42d, it is difficult to fit the points to a proper curve, and can been seen that the sensor does not quite cover this range yet, with sensitivity dropping outside a 95% confidence interval outside the window from 0- 10pM. An attempt to improve the dynamic range of the assay was made by removing excess, unbound target molecules *before* introducing free BPA into the system. This prevents BPA from the sample from being 'used up' by the aptamers on free target particles that were not captured by the magnetic probes, making it far more likely that the free BPA will compete with the aptamer badge complex.

It was determined by UV-vis shown in Figure 43a that ~ 30% of target nanoparticles from the original assembly solution were removed in the wash step. It is noted that there appears to be a 'blue shift' in the overall exaction profile of the assay. However if we look back at the profile for the magnetic probes and target particles separately in section III.2.i, it is observed that the washed particles simply are comprised of more probe particles than target, and thus are less influenced by the silver peak at ~400 nm. As shown in Figure 43b, washing not only significantly improved the assays dynamic range, but also yielded a more definitely defined sigmoidal response curve capable of being fit to a Hill sigmoidal curve, which represents binding avidity for assays with components with multiple binding sites: i.e. it is representative of cooperativity. The hill fit of the curve is shown and defined in Eq. 3. Comparting the performance of the sensor as set by the metrics defined in Table 4, it is noteworthy that washing the excess target away maintained a limit of detection in the pM range

as was seen with the unwashed assay. However the wash step significantly improved the upper bound of the analytical range, the limit of quantitation

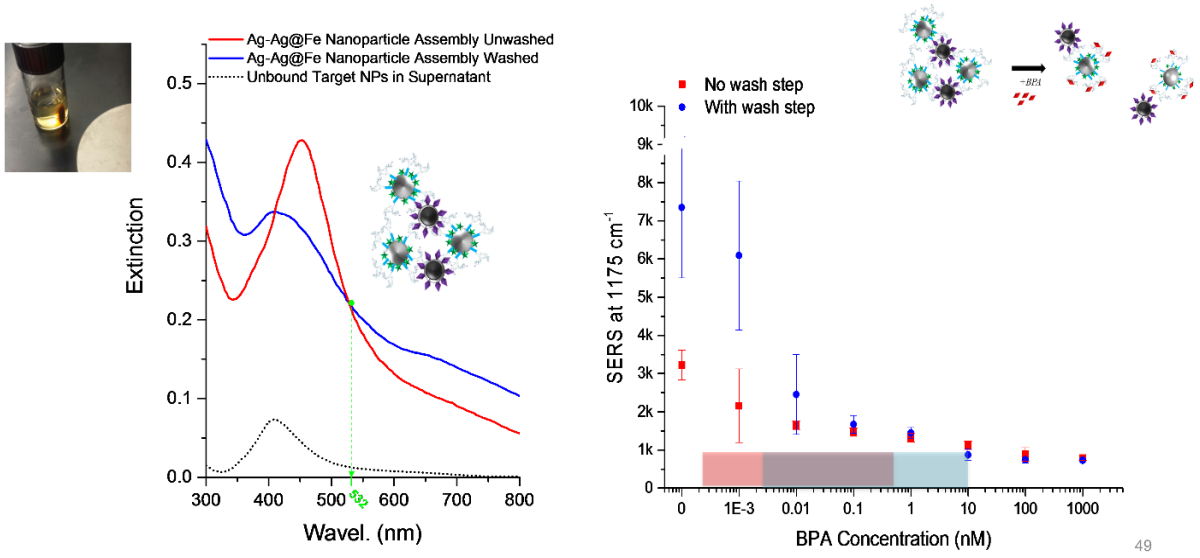

Figure 43. Image: assay nanoclusters being just prior to wash, where the yellow supernatant contains unbound target silver particles *a)* Comparison of extinction profiles of the assay nanoclusters before and after the magnetic washing step. *b)* Comparison of the sensors quantitative SERS response with and without the magnetic wash step, where the shaded boxes demonstrate the shift in the sensors dynamic range as a result of magnetic washing.

II.3.ii Off-chip SERS sensor performance metrics

The 10 collected SERS spectra for each of the concentrations tested were normalized to the 0 nM BPA blank sample to better conceptualize the percent SERS signal drop for each concentration. Their normalized SERS intensity as a function of concertation can be seen in Figure 44a, and can be through of as a fraction bound curve. For example for an input of 1000 nM BPA the figure shows that the SERS signal falls to ~20% of its initial signal intensity. When looking at this colloidal SERS assay's accuracy and precision across the detection range shown in Figure 44b (cut off at the previously determined LOQ of 10 nM), it becomes

apartment that the true LOQ is actually more like 10 pM, an order of magnitude below the lower limit of the physiological risk range (but close to the resting concentration of BPA in most adults). The Hill fit of the curve revealed a dissociation constant of 3.15 pM, far too close to the limit of detection and limit of the blank. Additionally the Hill cooperativity of n=0.93 implies the sensor is on the verge of noncooperative binding (when n=1), where the affinity of the target nanoparticle to free BPA is not dependent on whether or not they are already bound to the probe nanoparticles. Therefore this colloidal sensor may be able to provide a yes/no answer as to if a patient had a higher than normal BPA level, but it would not be able to precisely quantify the BPA level if it was above a specified threshold.

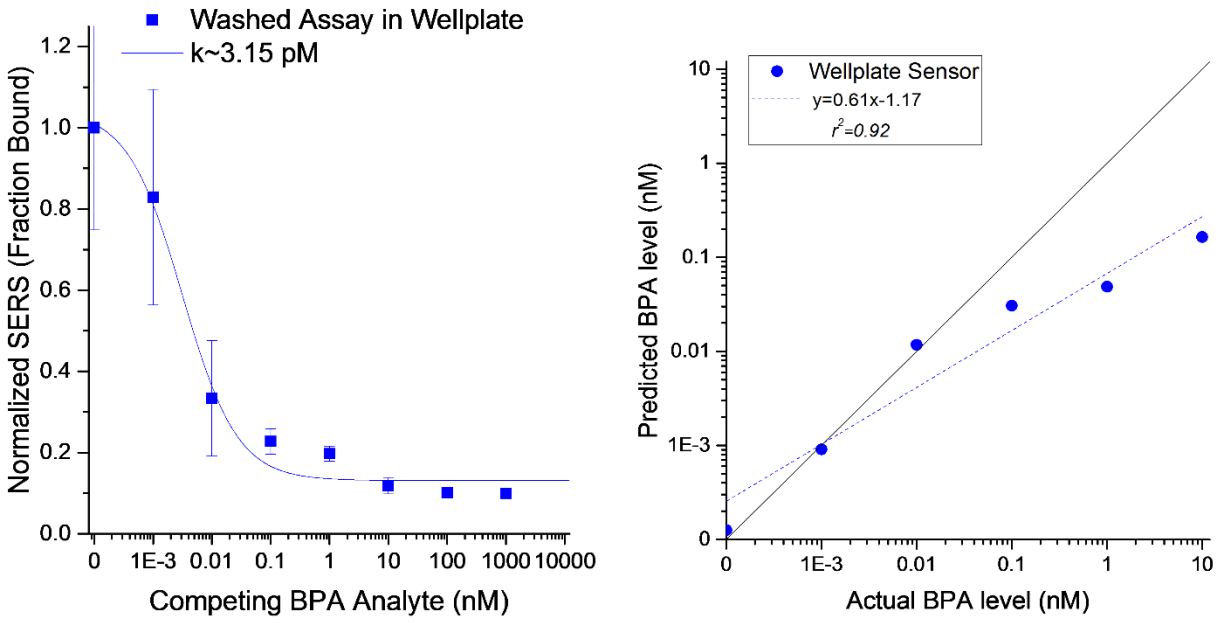

Figure 44. Sensor performance for the BPA completive binding assay analyzed in a standard well plate. Data is fit to a Hill1 curve with k=3.25 pM and n=0.93.

III.4 Final thoughts on off-chip SERS sensing

In this chapter, the successful design and characterization of a "SERS off" competitive binding assay using aptamers against the molecule BPA was performed. While further characterization revealed magnetic washing of the assay clusters shifted the sensor response closer to the desired full range from 200 pM -> 650 nM, the sensor performance could still only truly perform for the range of 87 pM -> 9 nM BPA, which is sufficient for yes/on sensing but too far below the physiological range for quantitiave results to be obtained clinically with this platform.[75, 128, 143] Also the wash step though useful for expanding and shifting the sensor's dynamic range, introduces an element of human error, requires several hours to pull down a few mLs of Ag@Fe particles, and could and should be replaced by a microfluidic equivalent, as discussed in Chapter IV.

CHAPTER IV

A MAGNETOFLUIDIC SERS-ON-A-CHIP DEVICE FOR HOUSING NANOPARTICLE ASSAYS

IV.1 Introduction to on-chip assay monitoring

A number of ferric micro- and nanoparticle-based SERS assays exist and have recently been studied for bringing human biomonitoring to the point-of-care.[33, 82, 136, 144-148] Magnetic particles are easy to localize using a permanent magnet placed at the side of a vial, bottom of a wellplate, nearby a microfluidic channel, or alternatively using a controllable embedded solenoid. This provides a simple way to exchange buffers, automate assay steps on chip, and reversibly concentrate or aggregate ferric nano- and micro-particles. For example, Jaebum Choo's group has utilized magnetic microbeads (analogous to commercially available TurboBeads) for a wide variety of SERS biosensing applications, including one embodiment using aptamer-coated gold nanoparticles (AuNPs) for detecting thrombin,[82] another using a solenoid microfluidic chip for trapping an AuNP competitive binding assay against the anthrax biomarker polyglutamic acid (PGA),[144] and an IgG immunoassay using antibody coated hollow gold nanoparticles (HGNs).[33] While these assays were successful and demonstrate the great potential in magnetic-based SERS assays, they fail to capitalize on the surface enhancement of the magnetic bead. While the Choo group has attempted coating their microbeads in silver,[145] it has been shown by others such as Park,[146] Carroll,[147] Guven,[148] and Donnelly[136] that using magnetic nanoparticles can significantly improve the SERS enhancement of these assays, and thus, improve upon the theoretical limit of detection capabilities of this approach.

IV.2 SERS mapping experiments to optimize packaging and resuspension of particles

As discussed in section II.4 simply holding magnetics near the walls of a PDMS chip does not provide sufficient reliability for SERS sensing, and is difficult to reproducibly aggregate particles without causing clogs. To overcome this, thin (~200nm) nickel pads capable of being magnetically activated were patterned on the surface of a glass slide under a PDMS microchannel. This method was adapted from Do et al[149] and allows the applied magnetic field to propagate down the array of Ni-pads and provide an even field distribution in the center of the channel. A schematic of the chip designed to house the BPA assay described on Chapter III is shown in Figure 45.

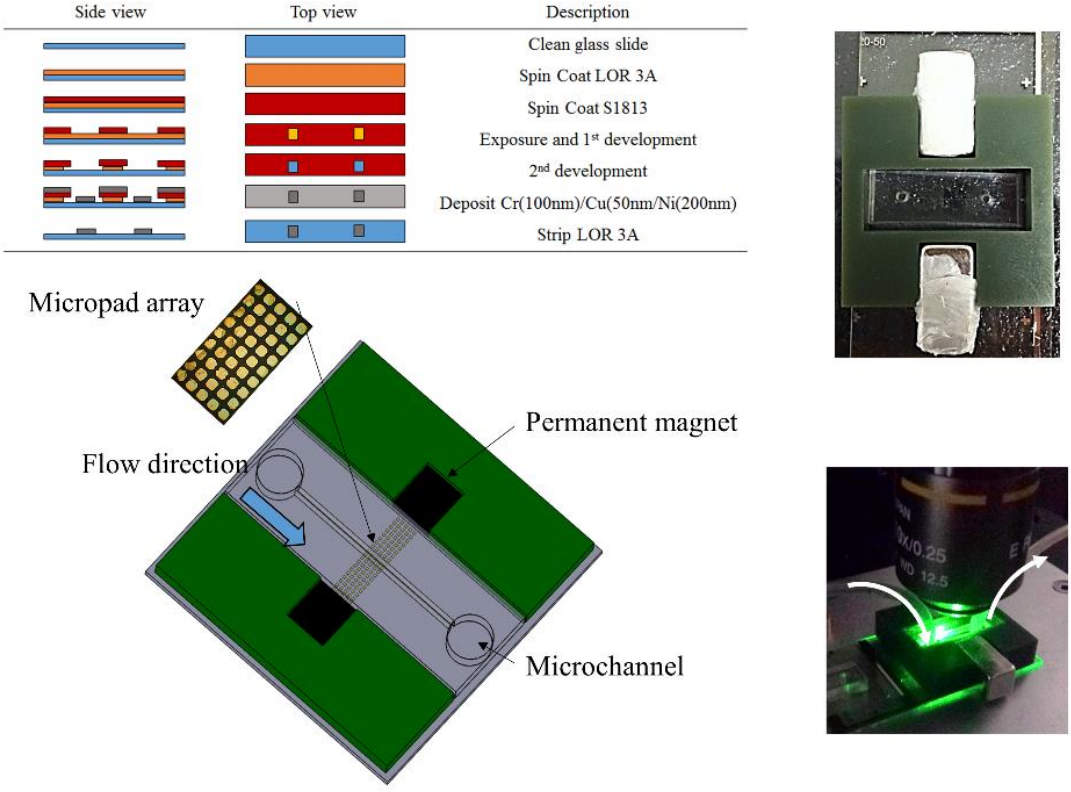

Figure 45. Schematic of the magnetofluidic chip design. Top left: table of fabrication process. Bottom left: top-down view of magnetofluidic chip. Right: Brightfield images of magnetofluidic chip.

Each magneto-fluidic SERS chip is composed of a 200 nm-thick nickel micromagnet array, PDMS microfluidic channel and two permanent neodymium magnets. As described by the table within Figure 45, the Ni-micromagnet array is deposited onto a glass microscope slide by photolithography using a methodology derived from Ilievski et al.[15] Glass slides are spin-coated with LOR 3A and S-1813 lift-off resists at 750 nm and 1.3 µm, respectively. After exposure and development, the pattern of the Ni-micromagnet array is visibly transferred onto the glass slides. Next, 100 nm-thick chromium and 50 nm-thick copper are continuously deposited on the pattern as the adhesion layer and then 200 nm-thick nickel is deposited as the 3rd and final 'magnetic response layer'. After deposition, the entire glass slide is placed into the chemical stripper of LOR 3A at 80 °C in order to remove the photoresist layer. It is noted that COMSOL models shown in Figure 46 revealed that at least two pads are necessary to evenly distribute the magnetic field in the channel.

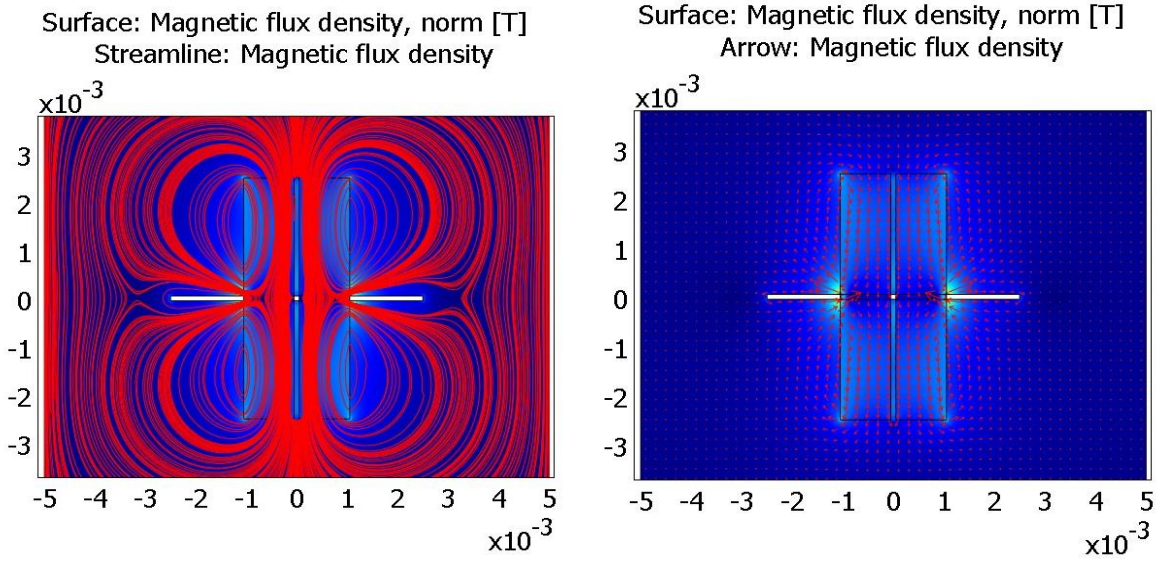

Figure 46. COMSOL models of the magnetic flux density streamline (left) and directionality (right) for the straight channel design A. These models indicate the necessity for at least two pads to be present to prevent favorability towards one pole, and to provide a focused field at the center of the channel, which is represented by the white horizontal line.

The 100 um-tall PMDS microfluidic channel are constructed using a silicon wafer mold via soft lithography. Uncured-PDMS solution (10:1) is poured over the silicon wafer mold and cured at 65 °C for 2 h as per typical soft lithography methods.[16] Finally, the PDMS microfluidic channel is bound to the glass slide patterned with the micromagnet array by reactive ion etching (i.e. plasma treatment), and inlet and outlet holes are removed using a biopsy punch. The nickel pads within the channel are not magnetically activated until the final 3D printed neodymium magnet holder is placed around the channel.

A 200 µL solution containing equal volumes of 225 pM of each of the target and probe nanoparticles in 0.1 M PBS was allowed to react overnight. The assay nanoclusters were then washed to remove any unbound target nanoparticles by holding a permanent magnet to the side of the sample vial and removing the supernatant, then resuspending in PBS. The 300 µL of the assay particles were allowed flow through the Ni-patterned magnetic channels using a 2 mL syringe and a pump rate of 10 µL/min. The chips were then left out overnight to dry for later use, and could be stored in this state for several months if packaged in sterile wrapping.

After reintroducing the dried assay particles to 0.1 M PBS, the SERS profile of the localized assembled nanoparticle clusters were mapped using WiTec Raman analysis software for chip designs A & B, and using Thermo-Scientific DXR Raman Omnic mapping software for chip design C. Both the WiTec and Thermo-Scientific Raman microscopes use a 10 x objective (NA 0.25), 600 lines/mm grating, and a 10 mW 532 nm laser, where all SERS measurements were collected with an integration time of 2 s (2 x 1 s total exposure) and a step size of 10 µm. Seventeen maps were collected for a total 3D mapping area of 3 x 300 x 170 µm (XYZ) for chip design A. Additionally 2D maps were scanned for areas of 75 µm x 75 µm (XY) for design B, and 70 µm x 350 µm (XY) & 70 µm x 70 µm (XZ) for chip design C.

Raman spectral maps of the MGITC peak at 1175 cm^{-1} were processed using Origin Pro 2015 graphing software.

In order to develop a more repeatable SERS analysis platform for assays relying on magnetic nanoparticles, two Ni-patterned glass slides and PDMS microchannel were initially developed (Figure 47). To optimize the magnetic collection rate and the SERS enhancement of the probe particles, both silver coated Fe_2O_3 and Fe_2CoO_4 nanoparticles bound to the Ag target particles were compared for two different Ni-pattern designs as shown in Figure 47: straight (chip design A - center images) and spotted (chip design B - right images).

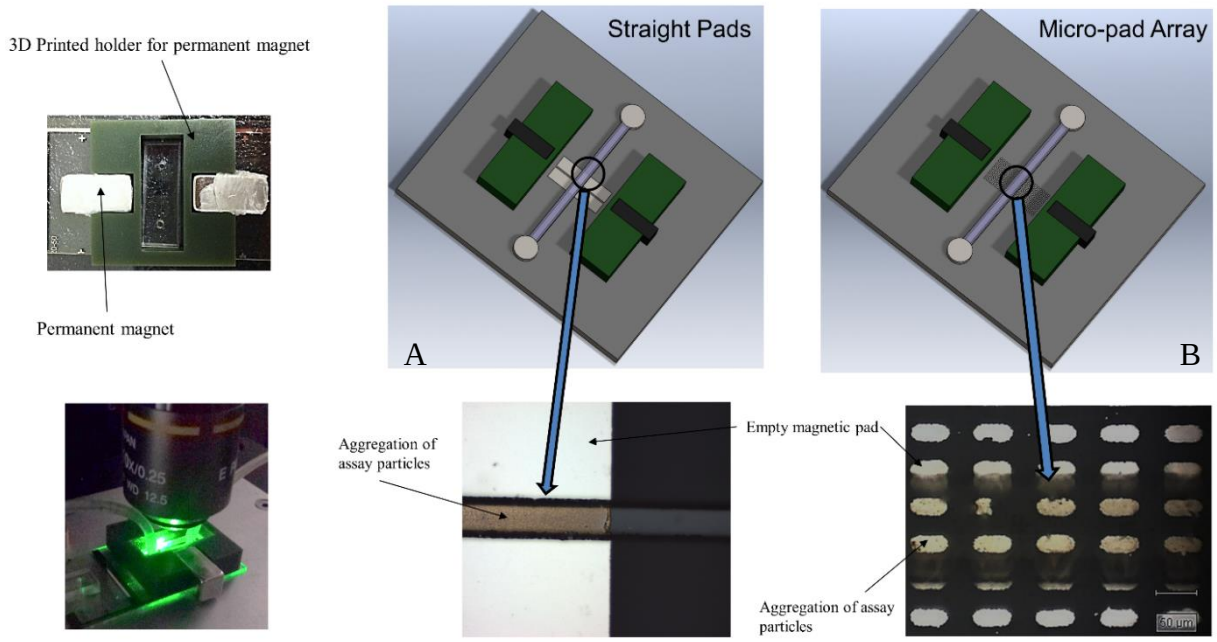

Figure 47. Magneto-fluidic chip designs: *Left:* Top-down and isometric images of the experimental setup for Raman mapping of the assay nanoparticle clusters within the magnetic microfluidic. *Center:* Schematic & brightfield images of the Ni-patterned detection regions through a 10x objective for chip design A. *Right:* Same as center for chip design B.

IV.2.i Design A: 2-pad sensing region - straight pattern

Using 3D Raman mapping, the straight channel (chip A) provided a more uniform nanoparticle organization with an apparent coefficient of variation of 23.6% across the entire channel when in focus with the Ni pads. However, only the assay with the less stable Co-doped Ag@Fe_2CoO_4 probe was magnetically trapped within chip design A. This was likely due to its rapid magnetic collection rate (on the order of minutes compared to hours required to pull down 2 mL in a glass scintillation vial) when compared to the 'plain' but stable ferric particles. To investigate, a depth profile of the straight channel after exposure to 200 µL of Co-doped ferric assay nanoparticle clusters was obtained in the form of 3D Raman spectroscopic maps (Figure 48).

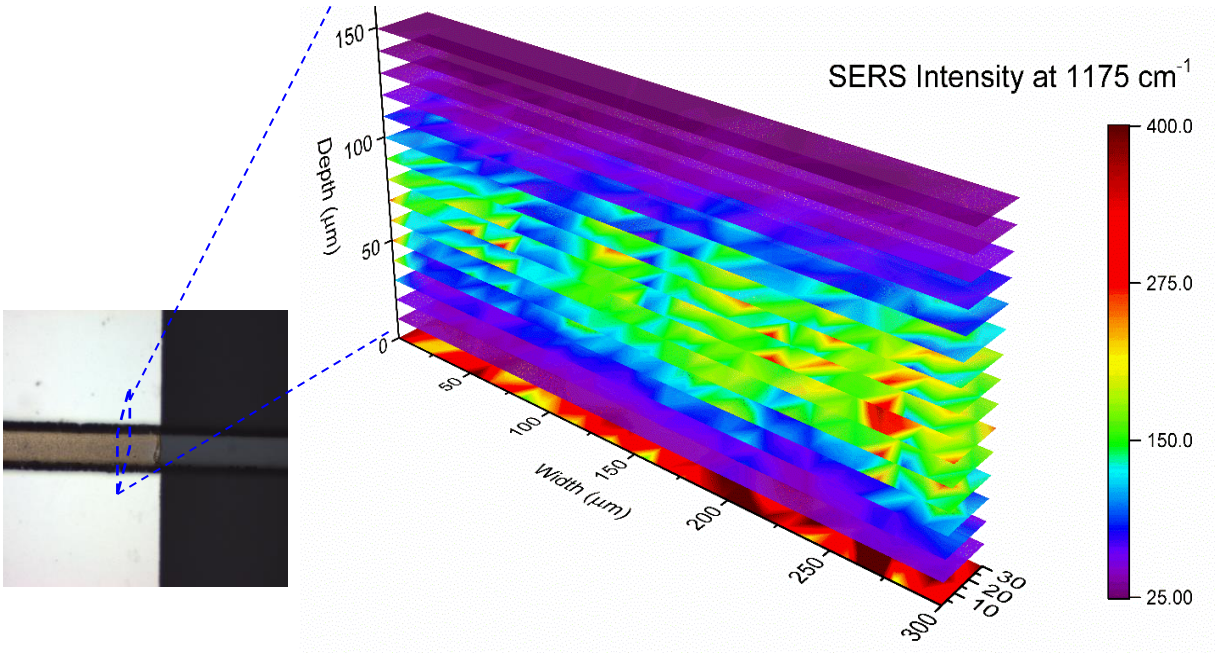

Figure 48. Chip design A depth profile: 17 stacked XY Raman intensity maps of the straight channel design filled with Ag@FeCo assay clusters, revealing that the majority of particles are located near the surface of the nickel pad.

The map in Figure 48 reveals that the large majority of particles are located at the *bottom* of the channel, near the surface of the deposited nickel. Unfortunately exposure to BPA competing analyte as high as 2 mg/mL (an order of magnitude above the physiological range) revealed no statistically relevant change in the SERS intensity in the channel. It is hypothesized that this is due to the magnetic field delivered to the pads being too strong at its surface and not reaching the full height of the channel with uniformity. This forces the particles too close together hindering competitive binding, or even causing irreversible mechanical aggregation. Additional error in the particle depth distribution could be due to the fact that only the polydisperse, unstable Ag@Fe_2CoO_4 probe assay was trapped within chip design A. While this design was simpler to pattern, and the Fe_2CoO_4 core being the much simpler choice in terms of synthesis, it was determined that this 'quick and easy' modality is not sufficient for monitoring molecular binding events with SERS. However, it may still be valuable as a simple solution for controlling magnetic nano (or micro) particles for assay wash steps. This design could be used to either automate washing steps and buffer exchanges, or automate the capture and enhancement of the spectra of specific components in a complex solution.

IV.2.ii Design B: 10-pad sensing region - oblong array

Chip design B, consisting of a 2 x 5 Ni-pad array, was able to trap the more stable Ag@Fe_2O_3 based assay. Chip B demonstrated a 10-fold improvement in the localized SERS enhancement (Figure 49) across the nickel pads when compared to chip A, and thus theoretically allows for lower limits of detection. In terms of quantification limits, looking at the raw peak intensity at 1175 cm^{-1} the coefficient of variation (%CV) across all 10 pads was at nearly 55%, though intensity maps in Figure 49 reveal this is mainly due a larger portion of particles located on top row of pads. This is likely a due to several incomplete nickel pads in the bottom row, which prevent the magnetic field from propagating uniformly across the pads. Unfortunately, depth profiles for design B were unable to be obtained as the small pad's field was still too concentrated near the surface, yielding enhanced assay signal only when in focus with the nickel pad as before.

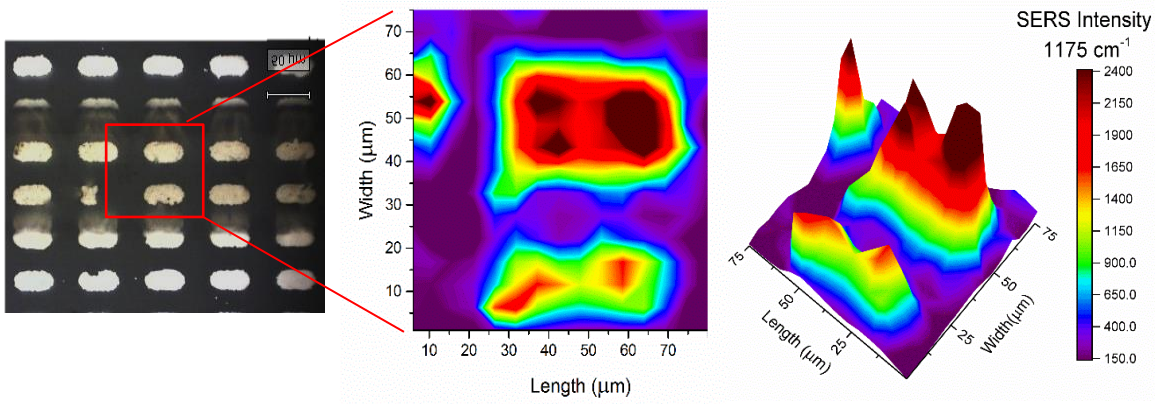

Figure 49. Chip design B Raman intensity profile: looking at the center column from the 2 x 5 array of Ni pads it is noticeable that particles favor the top row of pads, which are more uniform than the bottom row and thus provide a more uniform field.

IV.2.iii Design C: 5-pad sensing region - square array

To overcome the issues with chip designs A & B, a more optimized chip C nickel pad pattern was designed. Chip design C involves a 1 x 5 array of magnetically activated pads housed within the PDMS channel (Figure 50, left), which provides similar benefits as Chip B while avoiding the error induced by having two full rows of pads within the channel. This design allows the field to propagate in a manner that provides individual pad fields strong enough to trap the weakly-magnetic yet stable Ag@Fe_2O_3 based assay, while also providing uniform SERS enhancement in the Z-dimension. In other words, it is desired that the colloid is suspended in solution in the channel, and that particles are not irreversibly aggregated by the field pulling them too close together or onto the nickel surface, so that they may avoid steric hindrance when exposed to BPA.

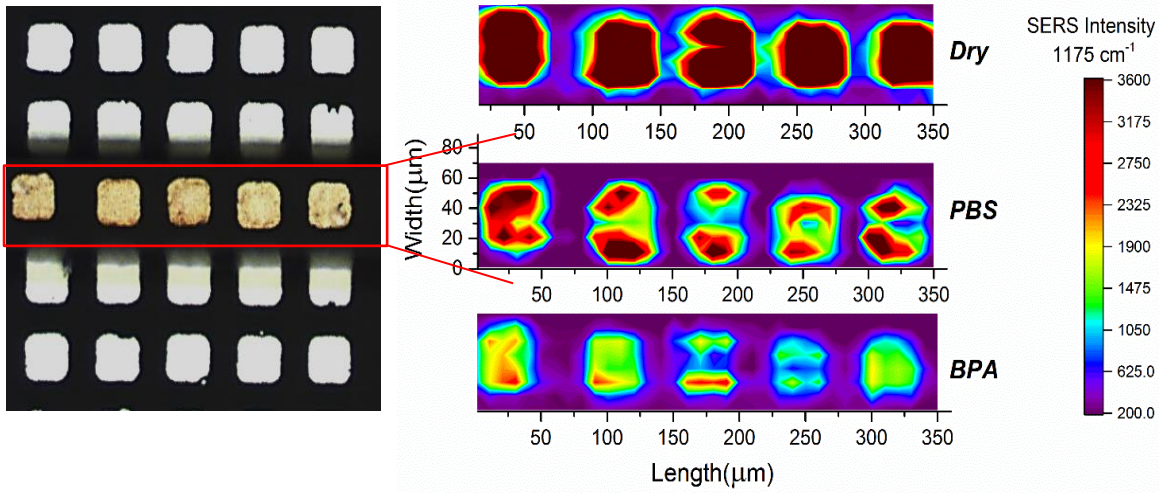

Figure 50. Chip design C Raman intensity profile: looking at the entire length of the 1 x 5 array of Ni pads. It is noticeable that SERS intensity of the particles is redistributed when buffer is introduces, indicating particle resuspension. Upon introduction to 2 mg/mL of BPA, the net SERS intensity over each pad decreased in response to competitive binding.

Top-down Raman intensity maps of chip loaded with the Fe_2O_3 based assay design C are also shown in Figure 50. When the channel is filled with dried assay particles, the chip demonstrated SERS enhancements up to 5 times higher than design B, and 30 times higher

than design A as demonstrated by comparing their averaged full spectra over the nickel patterns in Figure 51. However , for a more clear comparison across all three conditions, the map of the dried assay in Figure 50 is scaled to the maximum intensity of the PBS chip, which was 1.5 times higher than chip B and 9 times higher than chip A. The PBS filled channel, where the map was collected 10 µm above the pad surface, provides ample space for particle suspension and verifies that after filling the dried assay in the channel with PBS the particles are redispersed. This is further confirmed by an overall drop in the SERS intensity, which remained steady over 1 h after the full 300 µL of particles passed through the chip. Additionally, upon introduction of 2 mg/mL of BPA, a drastic drop in the SERS intensity at 1175 cm^{-1} was observed after 5 minutes, consistent with the behavior seen when testing the assay in the well plate and thus validating the chips capability for housing a molecularly mediated SERS assay.

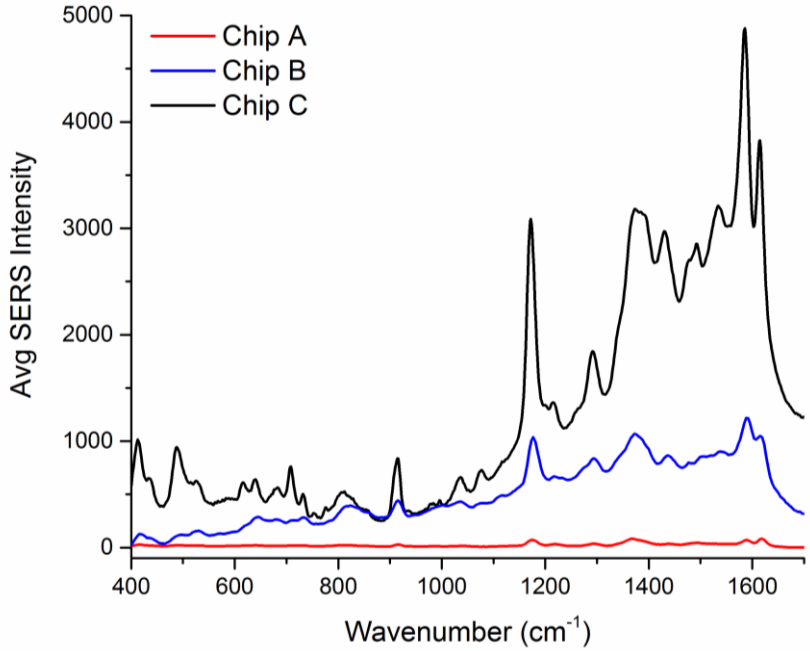

Figure 51. SERS spectra for the average across the entire Ni patterned area for all three chip designs. Here, it is observed that chip C provides a 30-fold enhancement compared to chip A, and a 3- fold enhancement compared to chip B.

To confirm that particles were not permanently bound to the nickel pads, depth profiles (XZ) of chip design C were collected with and without the syringe pump turned on at 10 µL/min (Figure 52). When the pump is on, the particles signal moves with the direction of flow. Although the %CV across the entire channel for design C is still ~50% as with design B, while investigating the signal variability across each individual pad it was discovered that the error could be reduced through individual normalization to the each of the five pads' maximum intensity at time t=0 (i.e. when the channel is filled with PBS). The improved standard error of the mean of the five chips yielded a %CV of ~25%, further improving upon the previous designs.

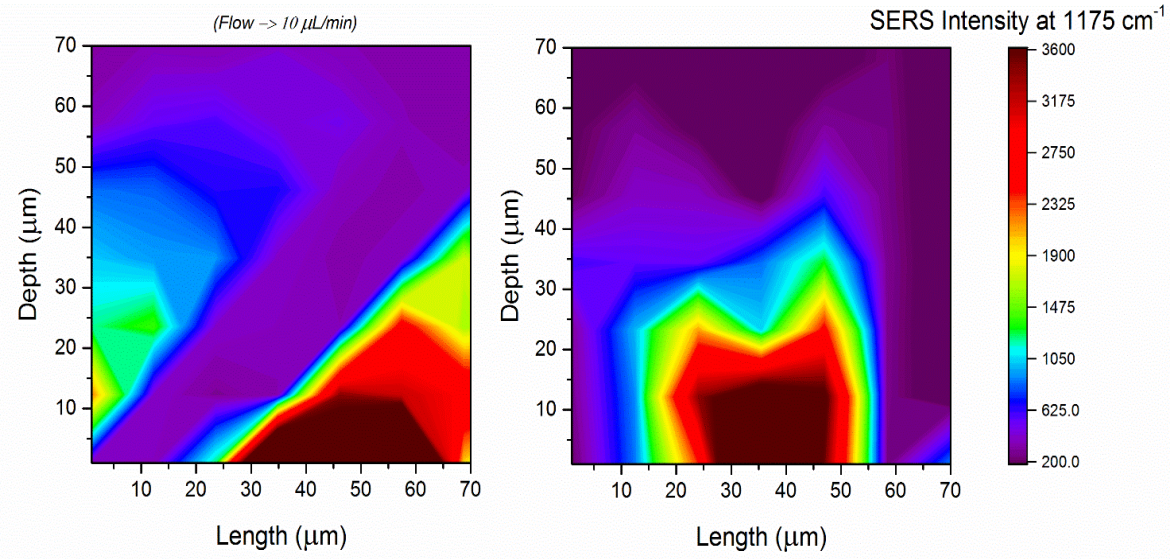

Figure 52. Chip design C Raman intensity depth profile: looking at the depth profile of the second pad in the array *Left*: Map shows that assay clusters are not bound to the surface and are able to move with the pump flow as a colloidal suspension. *Right:* Map shows assay cluster reorganize over the center of the pad when the pump is turned off.

IV.3 Final thoughts on SERS-on-a-chip platform final choice

Three magnetic microfluidic chip modalities were designed and tested with the two magnetic probe NP core types. It was found that the Ag@Fe_2O_3 particles were, on average, larger yet more uniform in size and more stable than Ag@Fe_2CoO_4. However, the addition of cobalt significantly improved the collection time of particles within the magnetic chips, and was also a much simpler synthesis method for the ferric core. Using 3D Raman mapping, the straight channel (chip A) design with the Ag@Fe_2O_3 particles intrinsically provided the most uniform nanoparticle organization, however particles were found to be localized mostly directly on the surface of the pad. While not suited for this application, this design is the simplest to produce, and could prove valuable for rapid prototyping of other magnetic nanoparticle assays.

While the nickel pad array channel chip design B was able to capture the desirable Ag@Fe_2O_3 particles and demonstrated a larger SERS enhancement, and thus a lower overall limit of detection, it had extreme variability between its 10 pads. For the chip C design, it was found that variability could be reduced to 25% through normalization to the maximum intensity within a pad. Additionally, it was demonstrated that this uniform signal could be obtained as far as 20 μm from the surface of the nickel pads, and was able to demonstrate the desired "SERS off" assay-competitive binding response to BPA. Moving forward Chip design C will be used along with the γ-Fe2O3 coated in silver as the probe nanoparticle in the following chapters and experiments.

CHAPTER V

MONITORING THE BPA APTAMER ASSAY IN A MAGNETOFLUIDIC SERS-ON-A-CHIP DEVICE

V.1 Introduction to the final experimental set up

A "turn-off" SERS assay platform methodology has been described in detail Chapters III and IV for the detection of small toxins using aptamer-mediated assembly of colloidal nanoparticles, where the assay is housed within a magnetofluidic chip. Briefly, colloidal SERS assay nanoclusters were formed through the mixing of probe (antigen) and target (aptamer-dye) nanoparticles and reaches an equilibrium after ~2 h. Particles were then washed by magnetic separation to remove any unbound target nanoparticles, a step that is a critical influence on the SERS sensor's dynamic range. It was determined that a 1x5 array of 200-nm thick 50-μm square nickel pads activated by permanent magnetics was optimal for a 70 μm wide PDMS channel. This design demonstrated SERS enhancements 300 times higher than those observed by the permanent magnets alone in Chapter II.

In the following chapter, the 3-5 min long BPA competitive binding event that was monitored by the SERS wellplate assay described in Chapter III will be monitored in the magnetofluidic chip C as described in Chapter IV, this time for a wide range of concentrations to define and compare the SERS sensor's performance metrics in and outside of the lab-on-a-chip device. It was previously determined that the probe nanoparticles have specific preference for the BPA aptamer target particles, and that the particles competitively bind with free BPA as well, implying that no nonspecific binding occurred. It's noteworthy that this approach has the potential to be translated to any aptamer/antigen pair, so long as the aptamer is PEGylated and thiolated and the antigen can be modified to be amine reactive, and provides the added

benefit of magnetic manipulation of the nanoparticle sensing network to remove any unbound nanoparticles or interferents from the sample that could potentially interfere with the Raman readout.

For the following experiments described, 200 µL of assay nanoclusters, consisting of prebound target (Ag) and probe (Ag@MNP) nanoparticles that were washed and packaged into magneto-fluidic SERS-on-a-chip design C and allowed to dry overnight. When ready to test, each SERS experiment was carried out according to the flow chart in Figure 53. First a SERS map is taken over the 5 pads when the particles are dry to ensure a sufficient number of assay particles were trapped, as damaged pads further down an array can prevent uniform field propagation. Second 0.1 PBS is introduces into the chip to resuspend the particles above the pads allowing for specific competitive binding to occur. Next, BPA at concentrations ranging from 1pM to 10 µM were introduced into the chip, and the SERS signal at the center of each pad was collected every 30 seconds for ~15 min. Last, the pump was turned off and a third and final map were collected. The percent signal drop before and after the addition of BPA obtained from the maps was compared to the results obtained for the wellplate assay in Chapter III. In a final experiment diluted whole blood was filtered using a lab on a chip device connected in cascade with the magnetofluidic chip to verify the sensors capability to function in complex media.

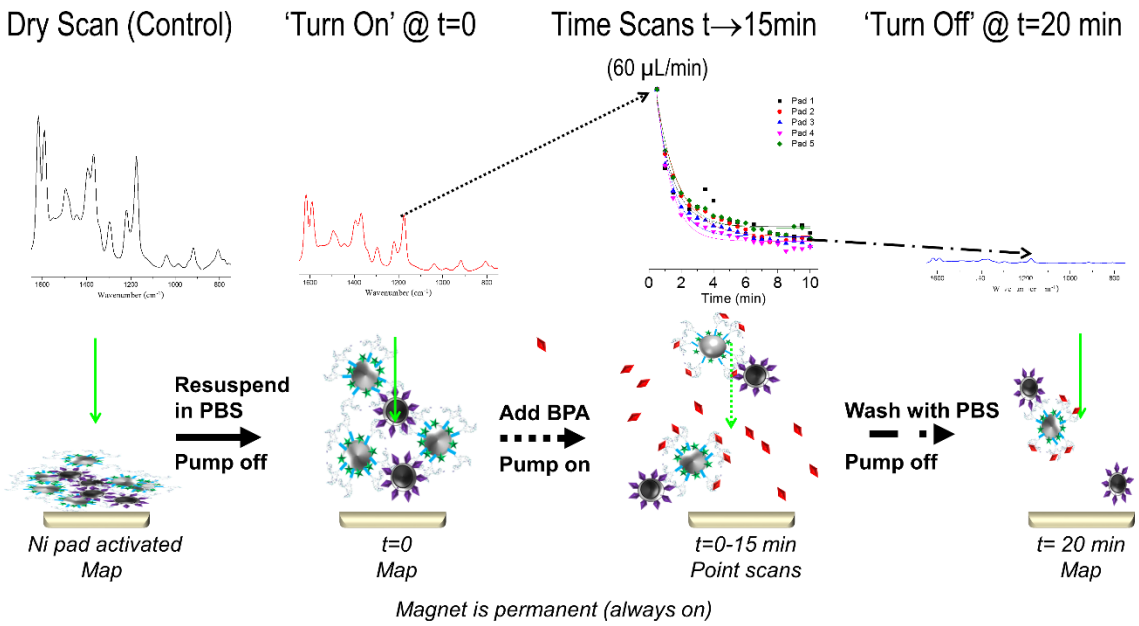

Figure 53. Process flow for testing the SERS assay in the magnetofluidic chip.

V.2 SERS-on-a-chip: monitoring the BPA aptamer assay in a magneto-fluidic chip

As an initial validation experiment, phenol kept at the same concentration as BPA (10 µM, 10x the physiological maximum) was also tested as a negative control in a magneto-fluidic chip to determine the assay's specificity to BPA. As shown in Figure 54, both the test and control chips observed a distinct drop in signal upon introduction of PBS into the channel, indicating that the particles redispersed in the z-dimension as expected. When phenol was added to the control chip, no statistically significant drop in SERS intensity was observed (Figure 54a). Additionally, after the introduction of competing analyte BPA, a measurable drop in SERS intensity was observed (Figure 54b), thus validating the sensors specificity.

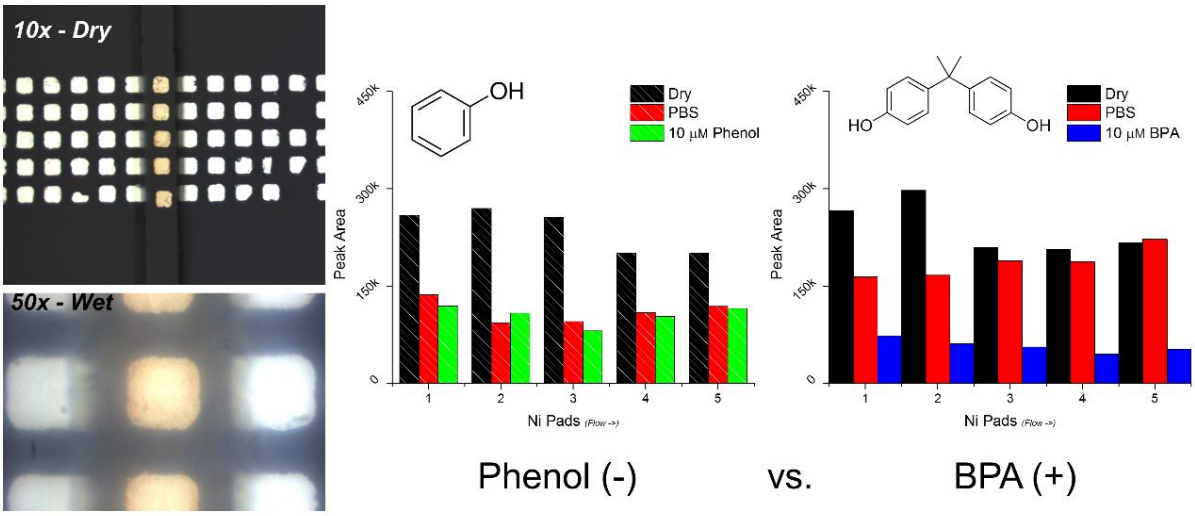

Figure 54. Control experiment demonstrating the BPA sensor specificity. Both the control (a) and test (b) chips exhibited particle resuspension after PBS entered the channel, but only the BPA test strip experienced a significant drop in SERS intensity after the analyte was introduced.

V.2.i Discussion on pad normalization & signal processing

It can be seen in the control experiment in Figure 54 and simply from brightfield images that there is an uneven distribution of particles across the five pads. Though all pads responded similarly to 0.02 ng/mL of BPA with a reaction time under 5 minutes as was predicted by the wellplate sensor in Chapter III, initial experiments revealed extreme variability in maximum achievable intensity across all 5 pads when looking at the raw SERS peak intensity (Figure 55a). This is likely due to the fact that more particles congregate over the magnetic pads closer to the channels inlet. However if each pad is normalized to the average pad SERS intensity *before* BPA is added (i.e. at t=0 when the channel is full of PBS only), then the variability in the SERS signal drop across the pads was comparable (Figure 55b).

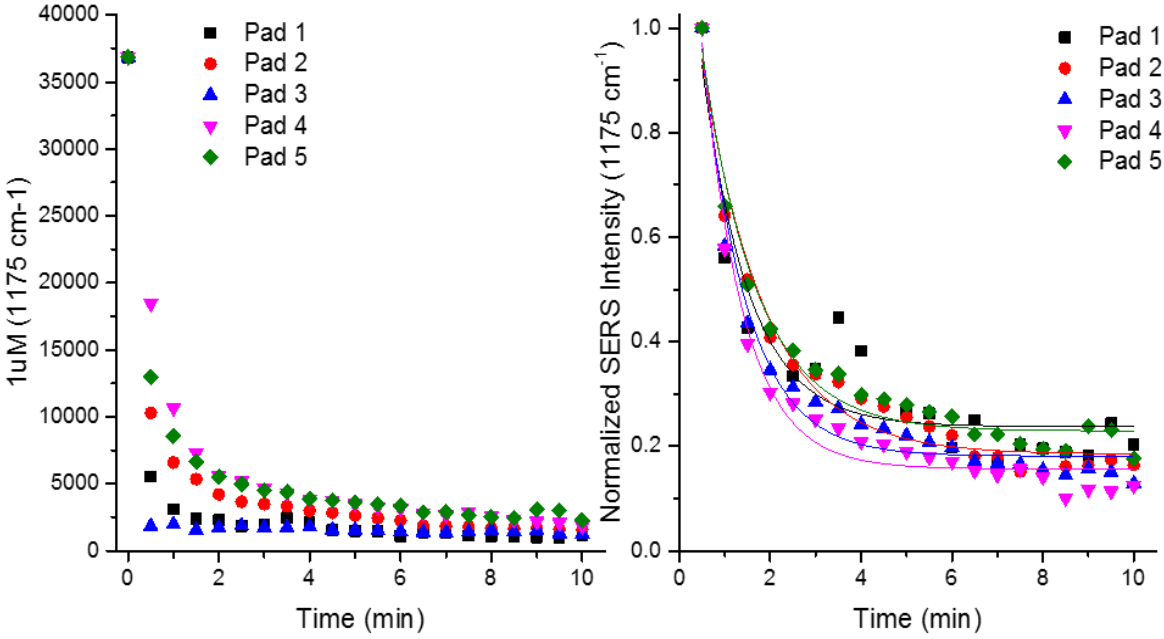

Figure 55: SERS as a function of time across the five pads in chip design C after exposure to 0.02 ng/mL BPA, where in the right image pads are normalized at t=0.

The SERS-on-a-chip device was tested against an expanded BPA concentration range (1 pM → 1 0μM) and SERS analysis using both peak intensity and peak area were explored. As shown in Figure 56, using the peak area of MGITC for the doublet surrounding the 1175 cm^{-1} peak previously used to characterize the wellplate yielded a much more defined dose-response curve than simply looking at the maximum peak intensity. A Hill fit was used, as defined in Eq. 3, where n=Hill coefficient, as it describes the cooperativity of binding involving ligands with multiple binding site, such as our aptamer and analyte coated nanoparticles.

$$y(x) = Start + (End - Start)\frac{x^n}{k^n + x^n}$$ **Equation 3**

A Hill1 cooperativity fit for this SERS off assay (Fraction bound vs. concentration Figure 56) is defined in Eq. 3 as follows: *Start*- the SERS intensity of a blank chip at t=0 (no BPA), *End*- the SERS intensity when the competing BPA concentration is 10x higher than BADGE concentration on the probes, ensuring saturation. SERS max (~1.0 fraction bound) controls the maximum rate achievable by the system. The dissociation constant used here is Michaelis constant *k*, and is the substrate concentration at which the reaction rate is half of SERS max (100% signal). This indicates the concentration that corresponds to half of the available binding sites being occupied was 2.31 nM, much closer to the center of the physiological range of 0.2 nM – 650 nM than the previous result of 3.15 pM with the wellplate method. This is likely due to the fact that the magnetic field brings the assay nanoclusters into even closer proximity, meaning that the assay nanoclusters couple more plasmons amongst other nanoclusters in the colloid, giving them a much higher SERS signal at the t=0 starting point, allowing for better analytical sensitivity. Further, the cooperativity coefficient for the chip sensor was n=0.26, which implies negative cooperativity in that once one target nanoparticle is bound to the magnetic probe, its affinity for other target nanoparticles decreases.

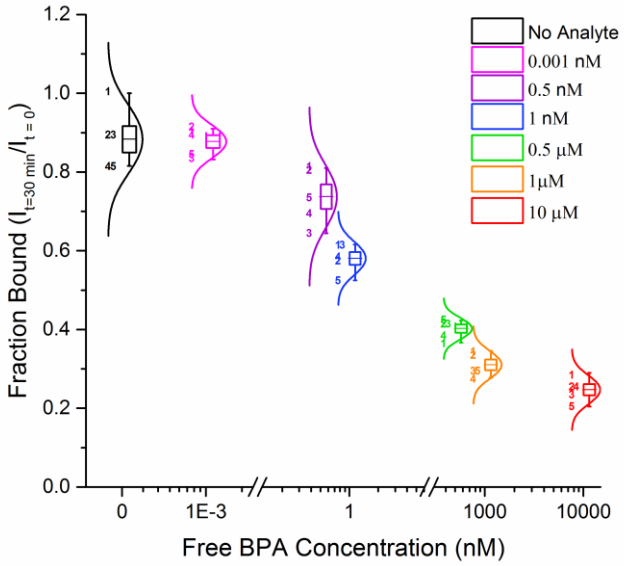

Figure 56. Box and whisker plots for visualizing quantitative resolution. Boxes represent the SERS signal distribution across the five pads for each tested concentration, with the Gaussian distribution overlaid. Pad numbers 1->5 at the left of the boxes represent the mean of n=25 scans over each pad area. The sensor is capable of differentiating between the three regions separated by the break marks with 95% confidence, but not between concentrations within the bracketed sections.

The box and whisker plots shown in Figure 56 allow for visualization of two key sensor characteristics: 1) the pad distribution which demonstrated that the 1st pad (inlet side) has the largest average signal and the 5th the least (outlet side), and 2) the quantitative resolution. From this figure it can be said that the SERS sensor's ability to differentiate between concentrations of BPA is limited to the three regions separated by the breaks. Specifically, the SERS nanocluster assay housed within the magneto-fluidic chip is able to distinguish between - It can perhaps be seen more clearly by observing the overlapping tails of the Gaussian distributions at each concentration compared to those surrounding it. Therefore, without any further analysis this chip could be configured with an algorithm to distinguish 'low' 'medium' and 'high' levels of BPA, but is not yet known if it is truly quantitative.

V.2.ii On-chip SERS sensor precision and accuracy (1 pM → 1 µM)

To better evaluate the on-chip SERS sensor's performance and the quality of the fit, we use the inverse of the Hill equation derived as shown in Eq. 4 to generate 'predicted' concentrations (x values) corresponding to the measured average SERS response across each pad. Inverse of the Hill function, where $f = x_{predicted}$ and is the predicted concentration for a measured SERS response $y(x_{actual})$. The number of cooperative binding site *n* and the binding affinity *k* are derived from the Hill1 fit in Eq. 3. These predicted values were then plotted vs the actual concertation of BPA that corresponded to each and plotted in Figure 57. The seven concentration data set for each of the 5 pads were first linearly fit separately to determine if there were any outliers (determined by Pearson correlation coefficient of 0.7), if the sensor was performing precisely and accurately (slope ~m=1), and establish a way to determine

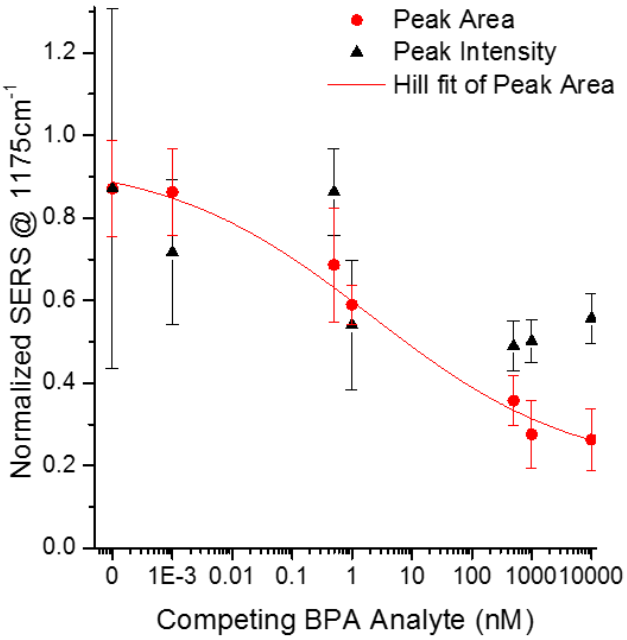

Figure 57. Comparison of SERS response curves using peak intensity vs peak area analysis. The peak area response is fit to a Hill1 curve as defined in Eq. 2 with k= 2.31 nM and n=0.26.

uncertainty of the input range. As can be seen by comparing their linear fit parameters, the center pad (Pad 3) was most accurate and precise, where pad 5 demonstrated the most variability.

$$x_{predicted} = f(y) = \left(\frac{k^n(-Start+y)}{End-y}\right)^{\frac{1}{n}} \qquad \textbf{Equation 4}$$

This same data set was averaged for each concentration and their mean's used to fit the linear regression for the chip sensor as a whole, as represented by box and whisker plots in Figure 58b. The fit is within a 99% confidence interval of the ideal x=y fit, and further demonstrates the versatility of the device. The diamond shaped box plots heave a breakpoint at the median value, and the mean is plotted as a bullet point for clarity as these were used to generate the linear fit 0.99x-0.09. Further, the linear fits from Figure 58a were used to generate a measure of uncertainty in the estimation of the actual BPA concentration.

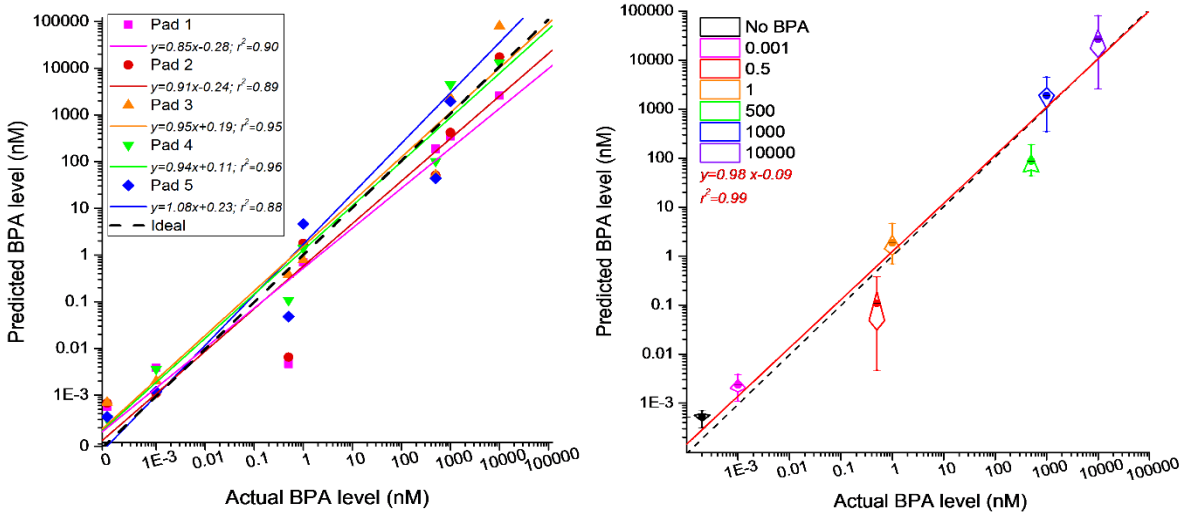

Figure 58 SERS sensor performance representing the quality of the Hill fit and the accuracy of the device. *Left* Mean values of SERS intensity across each pad plotted as a function of concentration. *Right* Box and whisker plots representing the mean and standard deviation of the plot on the left, with the red line representing the fit of the pad averages.

Together these figures reflect the combined precision and accuracy of the sensor as can be visualized in Figure 59. The overlapping shadow boxes represent regions of the input or output that cannot be easily distinguished from those surrounding it. I other words the illustrative shadows show how close the input values can be to each other and still be statistically distinguished (precision) or how close a readout measurement can be to the next and still predict a different predicted concentration (accuracy).

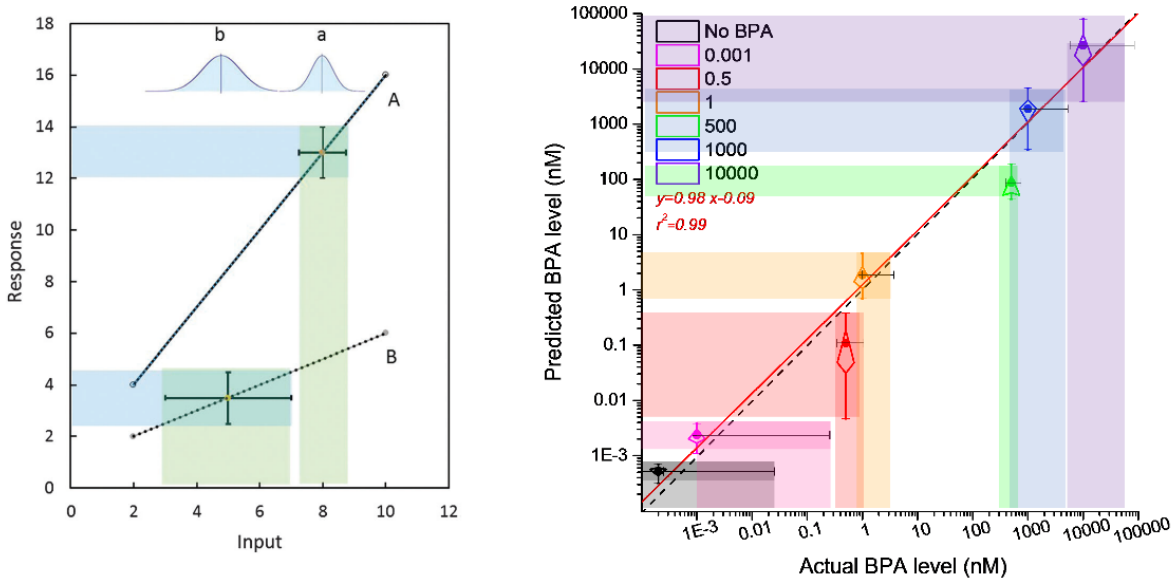

Figure 59. Illustration of analytical sensitivity (slope) and quantitative resolution (box shadow overlap) for the magneto-fluidic SERS sensor.

V.3 Comparison of off- and on-chip SERS sensor performance metrics

It can be observed by the direct comparison in Figure 60 that housing the assay within a magneto-fludic sensor chip significantly affected the assays response kinetics when overlaid with the response from the wellplate platform discussed in Chapter III. The dynamic range tested was expanded to fully encompass the full range observable in human serum and urine (~0.05-150 ng/mL)[74], marked by the green shadowbox in Figure 60, in order to test if a single

SERS sensor's dynamic range would be viable across multiple sample types. Both sensing curves were fit to a Hill plot, which were used to generate the predicted vs actual curves in Figure 60.

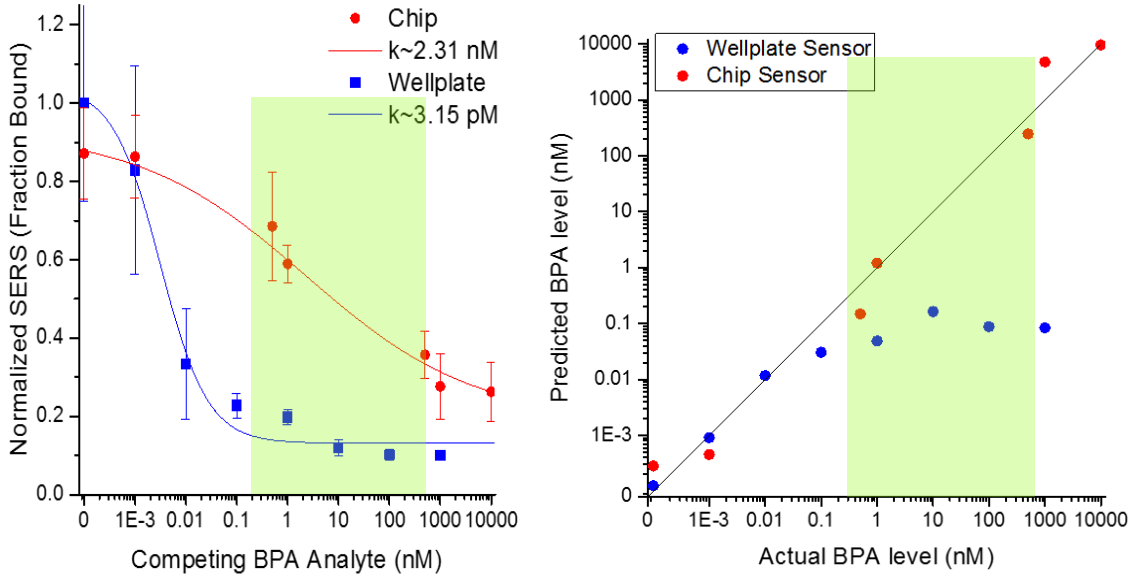

Figure 60 Comparison of sensor precision for the BPA completive binding assay when analyzed in a standard well plate vs housed within the magneto-fluidic chip. Physiological range is highlighted in green.

To truly analyze this SERS BPA competitive binding assay's ability to transition to the point of care, statistical figures of merit must meet the same performance requirements as in the clinic. Specifically we will define three metrics used to determine the true analytical sensing range of the assay for each of the two platforms. These ranges and the limits defining them will then be compared to the work of others and the current need. Last it will be discussed how each of these parameters can be tuned in the future through altering assay components or measurement methodologies.

The first and perhaps most important metric simply determines the concentration required to definitely say 'yes BPA is present', and is better known as the Limit of the Blank

(LoB). The LoB is the largest concentration of BPA that could be mistaken for a negative (no response, blank) test result. This metric is a measure of the combined system background noise including instrument noise from the Raman microscope, pipetting errors, etc. For this assay it is defined as the SERS off response with outside a 95% confidence window of the blank's response ($1.645\sigma_0 \rightarrow \alpha=0.05$) The LoB of the blank was slightly higher (5.2 pM) with the assay in the magneto-fluidic chip than was observed in the wellplate (3.1 pM), which is correct despite the standard error of the blank being larger for the wellplate due to the fact that the 1 pM response was more difficult to distinguished from the blank when the assay was housed in the chip. This is likely due to the particles being in closer proximity when in a magnetic field, making it difficult for low levels of BPA to displace enough target particles to significantly drop the SERS response.

Table 4. Performance metrics of the SERS competitive binding assay for BPA

	Definition	**384 Wellplate**		**Fluidic Chip**	
Limit of the Blank	*Lowest concentration that can be distinguished from blank distribution with 95 % confidence* LoB = $f(1\text{-}1.645\sigma_0)$	0.003 nM	0.07 ng/mL	0.005 nM	0.12 ng/mL
Limit of Detection	*Lowest concentration that can be distinguished from LOB distribution with 95 % confidence* LoD= $f(1\text{-}(\text{LoB} + 1.645\sigma_0))$	0.087 nM	1.97 ng/mL	0.725 nM	16.6 ng/mL
Limit of Quantitation	*Response of a sample with more than sufficient BPA to be a true positive* LoQ= $f(1\text{-}10\sigma_0)$	9.10 nM	0.21 µg/mL	190 nM	4.35 µg/mL
Dynamic Range	*Analytical sensing range of each SERS platform*	**0.003 → 9.10 nM**		**0.725 → 190 nM**	
Human Exposure Range	*Typical BPA levels found in human serum & urine*	**0.200 pM→ 650 nM (~0.05→150 ng/mL)**			
Michaelis Constant (K)	*BPA concentration producing half occupation*	0.00315		2.3100	

The next metric analyzed and perhaps the most commonly reported is the limit of detection (LoD), defined as the lowest detectable concentration that can be statistically distinguished from the LoB, or more commonly simplified as 3.29x standard deviation away from the blank.[150] This tells us the lower bound of the assay's dynamic range, or the lowest input required to initiate a definitive response from the SERS sensor. Again, the wellplate had a lower LoD at only 87 pM, on par with current trends for SERS sensors targeting small molecules, but several orders of magnitude below the average 'normal' BPA concentration of ~2 nM.[74] The chip demonstrated a LoD of 725pM, only about 3x higher than the lowest concentration reported in human serum.[128]

The last metric considered is the limit of quantitation (LoQ): the concentration that results in a response 10x greater than the standard deviation of the blank. In other words, this is the concentration that provides 10x more than enough target to warrant a true positive response. This is the upper bound of the detection range as concetrations higher than this would yield a true positive no matter what and fall outside the 95% confidence interval. It is observed by comparing the values in Table 4 with the plots in Figure 60 that these calculations are in agreement with the breakpoints of the sigmoidal Hill fits.

Combining these results we find that the SERS competitive binding assay has an analytical detection range of 87 pM → 9.1 nM when in a traditional wellplate and 725 pM → 190 nM when housed within a magneto-fluidic chip. Both these ranges fall within but slightly short of the full physiological range of 200 pM→ 650 nM (~0.05→150 ng/mL). The LoB, LoD, and LoQ are all related and thus if one change the others are affected as well. Addressing issues with nonspecific binding through aptamer choice or size of PEG may also help improve

the range, along with alterations to the number of ligands per particle as discussed in previous chapters.

V.4 Bringing SERS-on-a-chip to the point-of-care

V.3.i An inertial blood filtration chip

Blood, saliva, mucus, sweat, sputum, and other biological fluids are often hindered in their ability to be used in point-of-care (POC) diagnostics because their assays require some form of off-site sample preparation to effectively separate biomarkers from larger components such as cells. The rapid isolation, identification, and quantification of proteins and other small molecules circulating in the blood plasma from larger interferent molecules is therefore a particularly important factor for optical blood diagnostic tests, mainly due to spectroscopic interference from hemoglobin-rich red blood cells. In this work we present a sequential spiral PDMS microfluidic device for rapid (~1 min) on-chip blood cell separation.

The chip shown in Figure 61 utilizes Dean-force induced migration via two 5-loop Archimedean spirals in series. The chip was characterized in its ability to filter solutions containing 10 μm fluorescent beads and blood solutions doped with Alexa-labelled albumin. Through these experiments, both cellular and small molecule behaviors in the chip were assessed. The results exhibit an average RBC separation efficiency of 97.8% at a rate of 5.2 million cells per second as determined by absorbance measurements and a calibration curve developed with a haemocytometer. It was verified through monitoring fluorescently labelled albumin that the chip is capable of retaining 95% of plasma components, and assumed the other 5% is lost to adsorption onto the PDMS channel walls. This chip is uniquely suited for integration within a larger point-of-care diagnostic system for the testing of blood plasma, and

the use of multiple filtering spirals allows for the tuning of filtering steps, making this device and the underlying technique applicable for a wide range of separation applications.

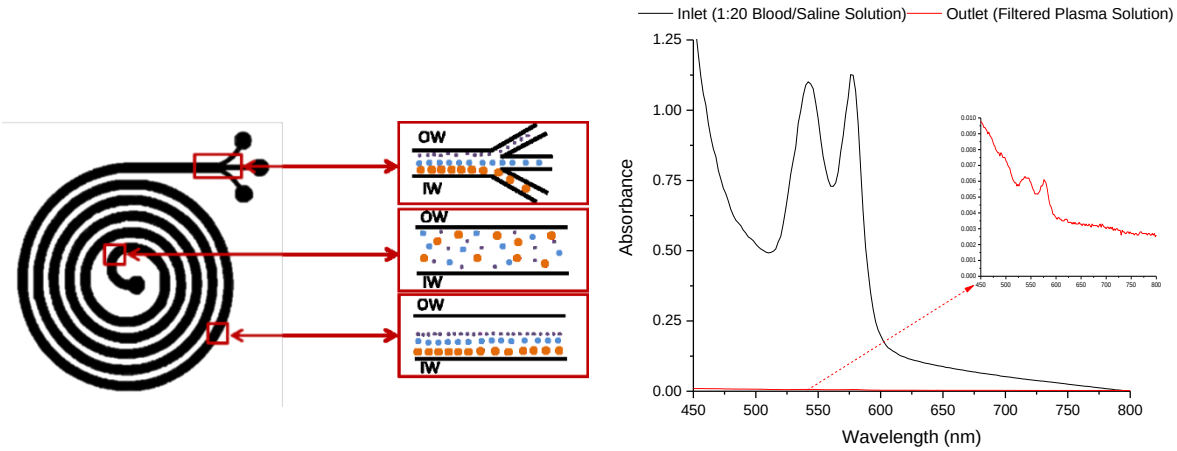

Figure 61. *Left:* Schematic demonstrating different phases of particle separation across the filter channel *Right:* UV-Vis of the channel's inlet and outlet solutions, demonstrating sufficient removal of interferent cellular components.

V.3.ii On-chip detection of BPA in filtered blood using SERS

In a final experiment the assay performance in complex media such as serum or plasma was tested using two cascaded lab-on-a-chip devices: a sample preparation chip and a SERS analysis chip. For the sample prep chip an inertial filtration chip as described in the previous section was used to filter diluted whole blood with and without BPA 0.02 ng/mL added. The plasma outlet of these chips were connected to the inlets of separate magneto-fluidic analysis chips that were preloaded with the BPA SERS nanocluster particles preloaded as described in V.I. The experiment was conducted in the same manner as depicted in Figure 53, except here scans were taken with the pump off, hence the longer reaction time seen in Figure 62, left. Raman maps were taken of the pads before and after exposure to BPA as shown in Figure 62,

right. It was observed that there was a net SERS signal decrease in response to BPA as respected, even in the presence of many potential interferents from the blood plasma.

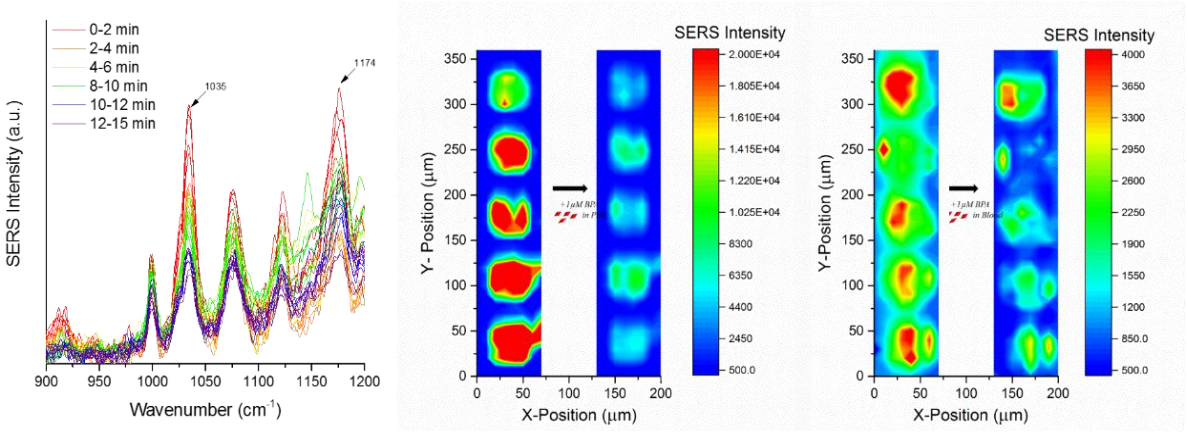

Figure 62. Sensor response to 1 µM BPA in PBS compared to 1 µM BPA doped into whole blood that has been filtered by an inertial microfluidic chip connected in cascade to the analysis chip.

The average SERS intensity across the entire Ni magnetic region before (t=0) and after (t=15) exposure to BPA are shown in Figure 63 with the ~10-15 most prominent Raman peaks labeled. When comparing these with the spectra from the 'clean' assay particles in PBS (Malachite Green Label only) as shown in Figure 63, and as listed in Table 5 it was observed that several new peaks emerged. In order to properly assign the new peaks present from the plasma sample. Table 5 shows the assignment of specific vibrational modes to the observed SERS peaks. This reveals that the new peaks, specifically those located at 1035 cm^{-1}, 1078 cm^{-1}, 1121 cm^{-1}, and 1261 cm^{-1} can be attributed to smaller blood components of blood capable of reaching the nanoparticle surface past the PEG layer, such as glucose, lipids, amino acids, etc. This implies the particles may benefit from a more sterically stabilizing polymer such as PVP

or even a hard silica shell for encapsulation, though there exists a tradeoff between added particle thickness due to stabilizers and decreased SERS enhancements.

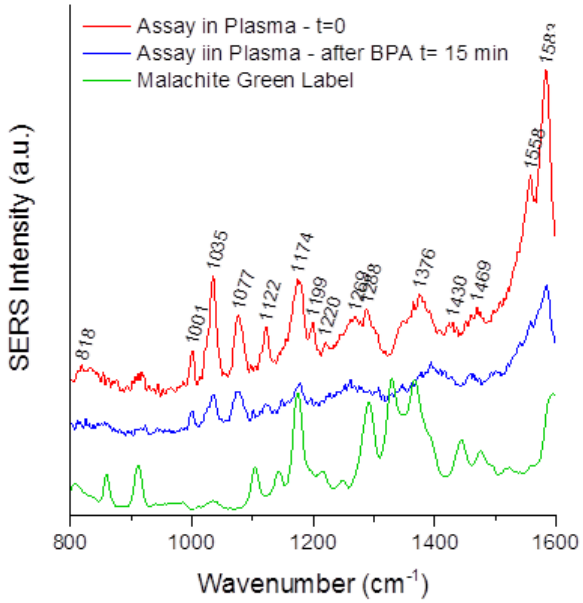

Figure 63. Stacked SERS spectra with peak assignments of the assay in plasma, in plasma doped with BPA, and in PBS.

Table 5. Peak assignment table for Raman modes visible before and after the introduction of plasma and of BPA-doped plasma

MGITC on Target NP	*Assay in Plasma*	*Assay in Plasma + BPA*	*SERS Assay or Plasma Component*	*Vibrational mode*
808	818	825	MGITC	benzene θ_{1g} (out of plane C-H)[151]
912	1001	1000	MGITC	benzene θ_{1v} (in plane) [151]
-	1035	1035	Phenylalanine	C-H in-plane bending mode [152]
-	1077	1078	Glucose /triglycerides/lipids	C-C [153]
1143	1122	1121	Proteins	C-N Strech (protien backbone) [154]
1174	1174	1178	MGITC	benzene ν_9 (in plane C-H) [151]
-	1199	-	MGITC	N-C stretch [151]
1215	1220	-	MGITC	NR_2 bend [13]
-	1269	1261	Lipids, amide III, collagen	CH2 In-plate deform, ν(CN), δ(NH) [49, 153, 155]
1292	1288	1307	MGITC	in-plane C-C & C-C-H [151]
1366	1376	1394	MGITC	N-ϕ stretch [151]
1444	1430	-	MGITC	NR_2 bend [151]
1476	1469	1459	MGITC	NR_2 rock [151]
	1558	-	Amino Acid (Tryptophan)	ν (C=C) [49, 155]
1594	1583	1584	MGITC	in-plane ring stretch &bend [151]

Though the 1175 cm^{-1} MGITC peak still dropped in intensity upon exposure to BPA as expected and as shown by Figure 64, the experiment setup required that the chips be connected by delicate tubing (Figure 64a) and was difficult to reproduce. Therefore for future work we developed an integrated chip (Figure 64b) that combines the sample prep and analysis chips. However initial testing has revealed that the drastic difference in optimal flow rates for each chip will prove to be a significant hurdle to overcome in future iterations of the device.

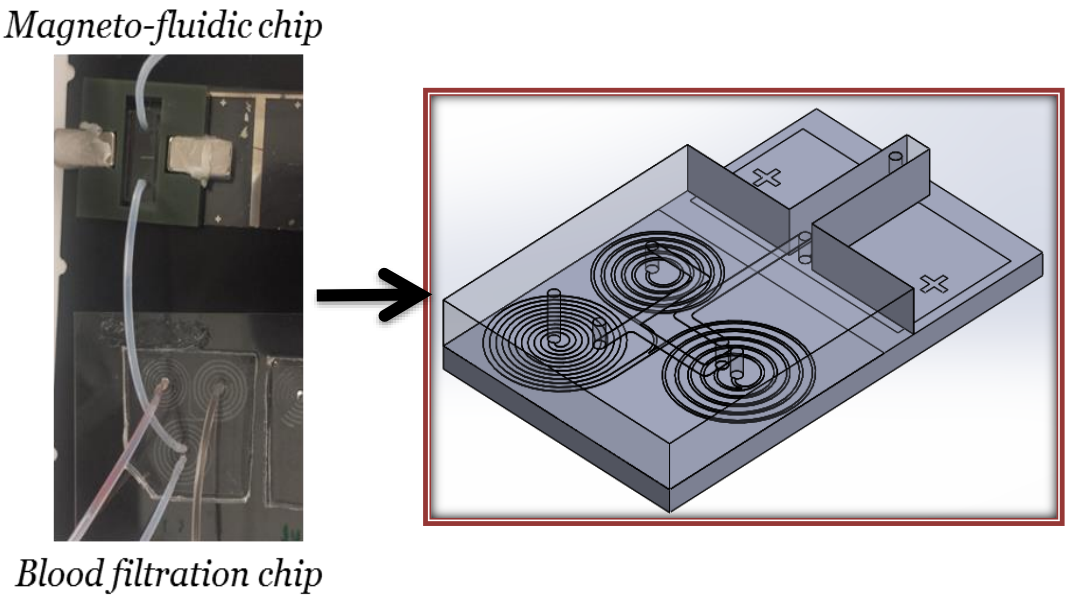

Figure 64. Next generation SERS-on-a-chip device will integrate the filtration and analysis chips, bringing this technology one step closer to the point-of-care

CHAPTER VI

SUMMARY & CONCLUDING REMARKS

The results and discussions presented throughout this dissertation lead to a couple of major themes to consider when designing platform point-of-care biosensing techniques that utilize colloidal SERS. Specifically, a bisphenol-A "turn off" competitive binding assay relying on aptamer-mediated assembly of SERRS active plasmonic and magnetic nanoparticles was analyzed in a traditional wellplate. It was determined that the analytical range of the SERS assay in the wellplate was 87 pM → 9.1 nM with a Michaelis constant of 3.25 pM between the target and probe particles. Housing this assay within a magneto-fluidic SERS analysis chip for automated sample processing and quantification shifted the Michaelis constant to 2.31 nM and the analytical range to 725 pM → 190 nM, which is much closer to the physiological range for BPA levels found in the serum and urine.

This assay has the potential to be translated to virtually any biomarker by utilizing aptamers: short synthetic ssDNA strands capable of binding to non-DNA targets. This technology can potentially be made sensitive to other analytes by simply exchanging the aptamer - making the platform "programmable" The enablement of technologies like this help push medicine to become increasingly personalized, predictive, and preventative by moving away from initial symptom based diagnostics and towards fast, quantifiable monitoring. Moving towards a lab-on-a-chip system like the magneto-fluidic assay chip presented here offers many advantages such as automated measurement, low sample and reagent volumes, minimal sample preparation, portability, disposability, and user-friendly interfaces. Thus the chip platform can potentially be used for a number of applications in situations where rapid blood or other biofluid diagnostics are of critical necessity, such as, for example, for

biomarkers for preeclampsia, dengue fever, radiation exposure, blood toxins, or myocardial infarction. Its versatility, low manufacturing cost, and portability also make it a promising technology for global health implications, ambulatory settings, as well as natural disaster relief worldwide. The enablement of technologies like this help push medicine to become increasingly personalized, predictive, and preventative by moving away from initial symptom based diagnostics and towards fast, quantifiable monitoring.

VI.1 The Future? Translatable methodologies & dual modality SERS

While many of the techniques discussed in this subchapter have made significant strides towards translating colloidal SERS to the point-of-care, they still face a number of hurdles. Much work is yet to be done in order to validate that these techniques can actually be applied for multiple biomarker types and applications. One of the most recent and relevant emerging methods for truly universal sensing was demonstrated by He, Li, and Hu with an aptamer recognition-induced target-bridged SERS assay based on magnetic chitosan (MCS) and silver/chitosan nanoparticle (Ag@CS NPs) binding.[156] A single aptamer target nanoparticle was used for the detection of three different types of protein, benefiting from the highly specific affinity of aptamers and biocompatibility of chitosan (CS). MCS coated in various antibodies or aptamer act as capture probes in the triple sandwich assay format shown. The sandwich complexes of aptamer (antibody)/protein/aptamer were first mixed with complex biological mediate and separated from biological samples after the reaction proceeded by magnetic manipulation with a permanent magnet under a glass slide. SERS signals were collected after washing the complexes and the protein concentrations indirectly correlated with the number of Raman report molecules left after washing. To demonstrate the translatability

of this method, three different proteins: thrombin, platelet derived growth factor (PDGF) and immunoglobulin E (lgE) were investigated. The CS shell demonstrated enhanced stability for longer shell life and prevention of signal drift due to loss of Raman reporter.

Like all colloidal nanoparticle assays, this method avoids slow diffusion limited kinetics problems observed for solid SERS substrate. The feasibility of this method for use at the point-of-care was demonstrated with PDGF BB in clinical serum samples, with an LOD of 3.2 pg/mL. The prediction results obtained from human serum of healthy patient's vs cancer patients using the proposed SERS method correlated with traditional ELISA results while the SERS method expanded the linear range. Another emerging trend in colloidal SERS is the utilization of dual optical modality approaches. For example many colloidal SERS assays also intrinsically exhibit a colorimetric response and dual sensing can facilitate simple yes/no readouts [157-158]. Researchers have also combined SERS with fluorescence to provide additional visual confirmation of binding results in a multiplexed format [159].

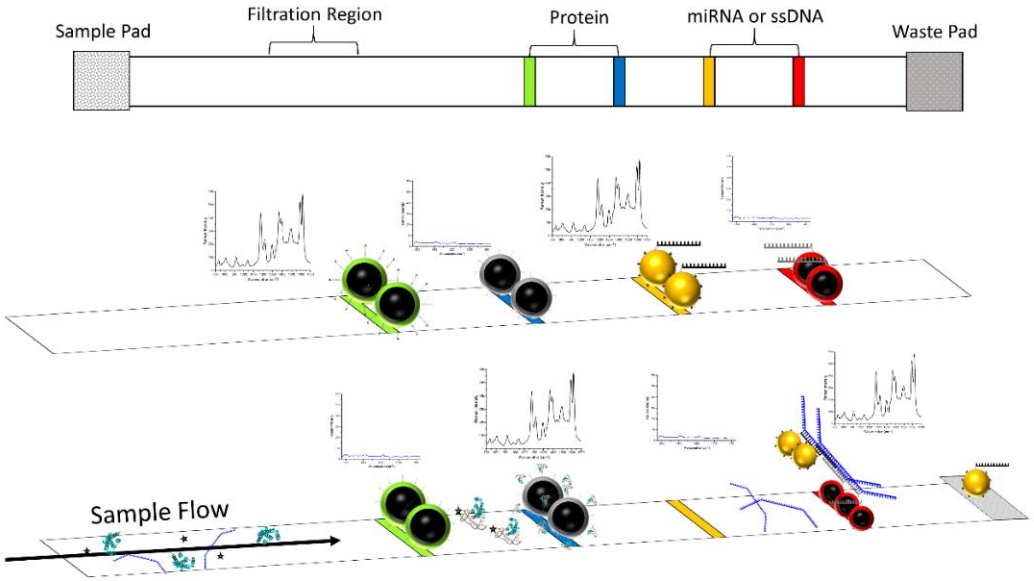

Figure 65. Cartoon depicting an imagined integration of molecularly mediated SERS assays and magnetic nanoparticles with low-cost paperfluidic lateral flow devices .

Combining these finding with our own findings it is proposed that future iterations of these magnetic nanoparticle-aptamer SERS sensors be translated from the PDMA platform onto a disposable paperfluidic lateral flow assay platform. This concept is depictured in Figure 65, and one could imagine a barcode type readout with both a colorimetric response with quick yes/no answers, as well as the ability to take a SERS measurement for a more quantitative result. This cartoon in Figure 65 also depicts slight variations on the competitive assay scheme used for small molecule to demonstrate that the platform technology could modified for monitoring proteins (green/blue) or oligonucleotides (yellow/red). As more analytical methodologies like these emerge and combine, the benefits of SERS for clinical chemistry at the point-of-care will be expended even further.

REFERENCES

1. Marks, H.; Mabbott, S.; Jackson, G. W.; Graham, D.; Cote, G. L. In *SERS active colloidal nanoparticles for the detection of small blood biomarkers using aptamers*, SPIE BiOS, SPIE: 2015; pp 93381C-5.

2. Marks, H.; Mabbott, S.; Huang, P.-J.; Jackson, G. W.; Kameoka, J.; Graham, D.; Cote, G. L., Comparison of Fe2O3 and Fe2CoO4 core-shell plasmonic nanoparticles for aptamer mediated SERS assays. In *SPIE BiOS*, SPIE: 2016; Vol. 9722, pp 97220N-8.

3. Marks, H. L.; Pishko, M. V.; Jackson, G. W.; Coté, G. L., Rational Design of a Bisphenol A Aptamer Selective Surface-Enhanced Raman Scattering Nanoprobe. *Analytical Chemistry* **2014,** *86* (23), 11614-11619.

4. Chen, S.-Y.; Lazarides, A. A., Quantitative Amplification of Cy5 SERS in 'Warm Spots' Created by Plasmonic Coupling in Nanoparticle Assemblies of Controlled Structure. *The Journal of Physical Chemistry C* **2009,** *113* (28), 12167-12175.

5. Goodman, C., Lewin *Laboratory Medicine: A National Status Report*; Centers for Disease Control and Prevention (CDC): 2008; pp 67-69.

6. Gubala, V.; Harris, L. F.; Ricco, A. J.; Tan, M. X.; Williams, D. E., Point of care diagnostics: status and future. *Anal Chem* **2012,** *84* (2), 487-515.

7. Nichols, J.; Ehrmeyer, S.-r.; Greenberg, N.; mett-Stabler, C. A. H.-.; Master, D. S.; Valdes, R. *Laboratory Medicine: Advancing Quality in Patient Care*; American Association for Clinical Chemistry (AACC): 2015; p 18.

8. Rohr, U.-P.; Binder, C.; Dieterle, T.; Giusti, F.; Messina, C. G. M.; Toerien, E.; Moch, H.; Schäfer, H. H., The value of in vitro diagnostic testing in medical practice: a status report. *PLoS ONE* **2016,** *11* (3), e0149856.

9. Kessler, R.; Glasgow, R. E., A proposal to speed translation of healthcare research into practice: dramatic change is needed. *Am J Prev Med* **2011,** *40* (6), 637-44.

10. Yager, P.; Domingo, G. J.; Gerdes, J., Point-of-care diagnostics for global health. *Annu Rev Biomed Eng* **2008,** *10*, 107-44.

11. Myers, F. B.; Lee, L. P., Innovations in optical microfluidic technologies for point-of-care diagnostics. *Lab on a Chip* **2008,** *8* (12), 2015-2031.

12. Woolley, C. F.; Hayes, M. A., Emerging technologies for biomedical analysis. *Analyst* **2014,** *139* (10), 2277-88.

13. Sohn, A. J.; Hickner, J. M.; Alem, F., Use of Point-of-Care tests (POCTs) by US primary care physicians. *J Am Board Fam Med* **2016,** *29* (3), 371-6.

14. Poste, G., Bring on the biomarkers. *Nature* **2011,** *469*, 156-157.

15. Adams, D. A.; Buus-Frank, M., Point-of-care technology: The i-STAT system for bedside blood analysis. *Journal of Pediatric Nursing* **1995,** *10* (3), 194-198.

16. Chin, C. D.; Laksanasopin, T.; Cheung, Y. K.; Steinmiller, D.; Linder, V.; Parsa, H.; Wang, J.; Moore, H.; Rouse, R.; Umviligihozo, G., Microfluidics-based diagnostics of infectious diseases in the developing world. *Nature Medicine* **2011,** *17* (8), 1015-1019.

17. Green, S. F., The cost of poor blood specimen quality and errors in preanalytical processes. *Clinical Biochemistry* **2013,** *46* (13), 1175-1179.

18. Plebani, M., Errors in clinical laboratories or errors in laboratory medicine? *Clinical Chemical Laboratory Medicine* **2006,** *44* (6), 750-759.

19. Horvath, A. R.; Lord, S. J.; StJohn, A.; Sandberg, S.; Cobbaert, C. M.; Lorenz, S.; Monaghan, P. J.; Verhagen-Kamerbeek, W. D.; Ebert, C.; Bossuyt, P. M.; Test evaluation working group of the European Federation of Clinical Chemistry Laboratory, M., From biomarkers to medical tests: the changing landscape of test evaluation. *Clin Chim Acta* **2014,** *427*, 49-57.

20. Granger, J. H.; Schlotter, N. E.; Crawford, A. C.; Porter, M. D., Prospects for point-of-care pathogen diagnostics using surface-enhanced Raman scattering (SERS). *Chem Soc Rev* **2016,** *45* (14), 3865-82.

21. Gellner, M.; Schutz, M.; Salehi, M.; Packeisen, J.; Strobel, P.; Marx, A.; Schmuck, C.; Schlucker, S., SERS microscopy: plasmonic nanoparticle probes and biomedical applications. *Proc Spie* **2010,** *7757*.

22. Butler, H. J.; Ashton, L.; Bird, B.; Cinque, G.; Curtis, K.; Dorney, J.; Esmonde-White, K.; Fullwood, N. J.; Gardner, B.; Martin-Hirsch, P. L.; Walsh, M. J.; McAinsh, M. R.; Stone, N.; Martin, F. L., Using Raman spectroscopy to characterize biological materials. *Nat. Protocols* **2016,** *11* (4), 664-687.

23. Ru, E. C. L.; Etchegoin, P. G., *Raman spectroscopy and related optical techniques*. Elsevier: Oxford, 2009.

24. Wilson, E. B.; Decius, J. C.; Cross, P. C., *Molecular Vibrations: The Theory of Infrared and Raman Vibrational Spectra*. Dover Publications: 1955.

25. Willets, K. A.; Van Duyne, R. P., Localized surface plasmon resonance spectroscopy and sensing. 2007; Vol. 58, pp 267-297.

26. Kneipp, K.; Kneipp, H.; Manoharan, R.; Hanlon, E. B.; Itzkan, I.; Dasari, R. R.; Feld, M. S., Extremely large enhancement factors in surface-enhanced Raman scattering for molecules on colloidal gold clusters. *Applied Spectroscopy* **1998,** *52* (12), 1493-1497.

27. Moskovits, M., Surface-enhanced spectroscopy. *Reviews of Modern Physics* **1985,** *57* (3), 783-826.

28. Rechberger, W.; Hohenau, A.; Leitner, A.; Krenn, J. R.; Lamprecht, B.; Aussenegg, F. R., Optical properties of two interacting gold nanoparticles. *Optics Communications* **2003,** *220* (1-3), 137-141.

29. Kneipp, K.; Kneipp, H.; Itzkan, I.; Dasari, R. R.; Feld, M. S., Surface-enhanced Raman scattering and biophysics. *J. Phys.: Condens. Matter* **2002,** *14*, R597-R624.

30. Etchegoin, P. G.; Lacharmoise, P. D.; Le Ru, E. C., Influence of photostability on single-molecule surface enhanced Raman scattering enhancement factors. *Anal. Chem.* **2009,** *81*, 682-688.

31. Wang, Y. L.; Schlucker, S., Rational design and synthesis of SERS labels. *Analyst* **2013,** *138* (8), 2224-2238.

32. Benford, M.; Wang, M.; Kameoka, J.; Good, T.; Cote, G. In *Functionalized nanoparticles for measurement of biomarkers using a SERS nanochannel platform*, 2010.

33. Chon, H.; Lim, C.; Ha, S. M.; Ahn, Y.; Lee, E. K.; Chang, S. I.; Seong, G. H.; Choo, J., On-Chip Immunoassay Using Surface-Enhanced Raman Scattering of Hollow Gold Nanospheres. *Analytical Chemistry* **2010,** *82* (12), 5290-5295.

34. Lee, P. C.; Meisel, D., Adsorption and surface-enhanced Raman of dyes on silver and gold sols. *Journal of Physical Chemistry* **1982,** *86* (17), 3391-3395.

35. Rohr, T. E.; Cotton, T.; Fan, N.; Tarcha, P. J., Immunoassay employing surface-enhanced Raman spectroscopy. *Anal Biochem* **1989,** *182* (2), 388-98.

36. Nie, S.; Emory, S. R., Probing single molecules and single nanoparticles by surface-enhanced Raman scattering. *Science* **1997,** *275* (5303), 1102-1106.

37. Cassar, R. N.; Graham, D.; Larmour, I.; Wark, A. W.; Faulds, K., Synthesis of size tunable monodispersed silver nanoparticles and the effect of size on SERS enhancement. *Vibrational Spectroscopy* **2014,** *71*, 41-46.

38. Walton, B. M.; Huang, P. J.; Kameoka, J.; Cote, G. L., Use of a micro- to nanochannel for the characterization of surface-enhanced Raman spectroscopy signals from unique functionalized nanoparticles. *Journal of biomedical optics* **2016,** *21* (8), 85006.

39. Liu, X.; Atwater, M.; Wang, J.; Huo, Q., Extinction coefficient of gold nanoparticles with different sizes and different capping ligands. *Colloids and Surfaces B: Biointerfaces* **2007,** *58* (1), 3-7.

40. Zhang, Q.; Xie, J.; Yu, Y.; Lee, J. Y., Monodispersity control in the synthesis of monometallic and bimetallic quasi-spherical gold and silver nanoparticles. *Nanoscale* **2010,** *2* (10), 1962-75.

41. Storhoff, J. J.; Lazarides, A. A.; Mucic, R. C.; Mirkin, C. A.; Letsinger, R. L.; Schatz, G. C., What Controls the Optical Properties of DNA-Linked Gold Nanoparticle Assemblies? *J Am Chem Soc* **2000,** *122* (19), 4640-4650.

42. Mirkin, C. A.; Letsinger, R. L.; Mucic, R. C.; Storhoff, J. J., A DNA-based method for rationally assembling nanoparticles into macroscopic materials. *Nature* **1996,** *382* (6592), 607-609.

43. Cao, Y. C.; Jin, R.; Mirkin, C. A., Nanoparticles with Raman Spectroscopic Fingerprints for DNA and RNA Detection. *Science* **2002,** *297* (5586), 1536-1540.

44. Ross, M. B.; Ashley, M. J.; Schmucker, A. L.; Singamaneni, S.; Naik, R. R.; Schatz, G. C.; Mirkin, C. A., Structure–Function Relationships for Surface-Enhanced Raman Spectroscopy-Active Plasmonic Paper. *The Journal of Physical Chemistry C* **2016,** *120* (37), 20789-20797.

45. Rygula, A.; Majzner, K.; Marzec, K. M.; Kaczor, A.; Pilarczyk, M.; Baranska, M., Raman spectroscopy of proteins: a review. *Journal of Raman Spectroscopy* **2013,** *44* (8), 1061-1076.

46. Xiao, S. J.; Wieland, M.; Brunner, S., Surface reactions of 4-aminothiophenol with heterobifunctional crosslinkers bearin both succinimidl ester and maleimide for biomolecular immobilization. *J Colloid Interf Sci* **2005,** *290* (1), 172-183.

47. Vo-Dinh, T., Nanobiosensing using plasmonic nanoprobes. *IEEE Journal on Selected Topics in Quantum Electronics* **2008,** *14* (1), 198-205.

48. Chou, I. H.; Benford, M.; Beier, H. T.; Coté, G. L.; Wang, M.; Jing, N.; Kameoka, J.; Good, T. A., Nanofluidic biosensing for β-amyloid detection using surface enhanced raman spectroscopy. *Nano Letters* **2008,** *8* (6), 1729-1735.

49. Feng, S.; Wang, W.; Tai, I. T.; Chen, G.; Chen, R.; Zeng, H., Label-free surface-enhanced Raman spectroscopy for detection of colorectal cancer and precursor lesions using blood plasma. *Biomed. Opt. Express* **2015,** *6* (9), 3494-3502.

50. Wang, J.; Lin, D.; Lin, J.; Yu, Y.; Huang, Z.; Chen, Y.; Lin, J.; Feng, S.; Li, B.; Liu, N.; Chen, R., Label-free detection of serum proteins using surface-enhanced Raman spectroscopy for colorectal cancer screening. *Journal of biomedical optics* **2014,** *19* (8), 087003-087003.

51. Schutz, M.; Kustner, B.; Bauer, M.; Schmuck, C.; Schlucker, S., Synthesis of Glass-Coated SERS Nanoparticle Probes via SAMs with Terminal SiO2 Precursors. *Small* **2010,** *6* (6), 733-737.

52. Kustner, B.; Gellner, M.; Schutz, M.; Schoppler, F.; Marx, A.; Strobel, P.; Adam, P.; Schmuck, C.; Schlucker, S., SERS Labels for Red Laser Excitation: Silica-Encapsulated SAMs on Tunable Gold/Silver Nanoshells. *Angew Chem Int Edit* **2009,** *48* (11), 1950-1953.

53. Schlucker, S., SERS Microscopy: Nanoparticle Probes and Biomedical Applications. *Chemphyschem* **2009,** *10* (9-10), 1344-1354.

54. Jehn, C.; Kustner, B.; Adam, P.; Marx, A.; Strobel, P.; Schmuck, C.; Schlucker, S., Water soluble SERS labels comprising a SAM with dual spacers for controlled bioconjugation. *Phys Chem Chem Phys* **2009,** *11* (34), 7499-7504.

55. Donnelly, T.; Faulds, K.; Graham, D., Investigation of Silver Nanoparticle Assembly Following Hybridization with Different Lengths of DNA. *Particle & Particle Systems Characterization* **2016,** *33* (7), 404-411.

56. Mabbott, S.; Thompson, D.; Sirimuthu, N.; McNay, G.; Faulds, K.; Graham, D., From synthetic DNA to PCR product: detection of fungal infections using SERS. *Faraday discussions* **2016,** *187*, 461-472.

57. Simpson, J.; Craig, D.; Faulds, K.; Graham, D., Mixed-monolayer glyconanoparticles for the detection of cholera toxin by surface enhanced Raman spectroscopy. *Nanoscale Horizons* **2016,** *1* (1), 60-63.

58. Gracie, K.; Lindsay, D.; Graham, D.; Faulds, K., Bacterial meningitis pathogens identified in clinical samples using a SERS DNA detection assay. *Analytical Methods* **2015,** *7* (4), 1269-1272.

59. Gracie, K.; Correa, E.; Mabbott, S.; Dougan, J. A.; Graham, D.; Goodacre, R.; Faulds, K., Simultaneous detection and quantification of three bacterial meningitis pathogens by SERS. *Chemical Science* **2014,** *5* (3), 1030-1040.

60. Mahmoudi, M.; Sant, S.; Wang, B.; Laurent, S.; Sen, T., Superparamagnetic iron oxide nanoparticles (SPIONs): development, surface modification and applications in chemotherapy. *Advanced Drug Delivery Reviews* **2011,** *63* (1), 24-46.

61. Büchner, T.; Drescher, D.; Merk, V.; Traub, H.; Guttmann, P.; Werner, S.; Jakubowski, N.; Schneider, G.; Kneipp, J., Biomolecular environment, quantification, and intracellular interaction of multifunctional magnetic SERS nanoprobes. *Analyst* **2016,** *141* (17), 5096-5106.

62. Tekin, H. C.; Gijs, M. A. M., Ultrasensitive protein detection: A case for microfluidic magnetic bead-based assays. *Lab on a Chip - Miniaturisation for Chemistry and Biology* **2013,** *13* (24), 4711-4739.

63. Ramadan, Q.; Gijs, M. A. M., Simultaneous sample washing and concentration using a "trapping-and- releasing" mechanism of magnetic beads on a microfluidic chip. *Analyst* **2011,** *136* (6), 1157-1166.

64. Kumar, G. V. P.; Rangarajan, N.; Sonia, B.; Deepika, P.; Rohman, N.; Narayana, C., Metal-coated magnetic nanoparticles for surface enhanced Raman scattering studies. *Bulletin of Materials Science* **2011,** *34* (2), 207-216.

65. Wang, C.; Li, P.; Wang, J.; Rong, Z.; Pang, Y.; Xu, J.; Dong, P.; Xiao, R.; Wang, S., Polyethylenimine-interlayered core-shell-satellite 3D magnetic microspheres as versatile SERS substrates. *Nanoscale* **2015,** *7* (44), 18694-18707.

66. Zhang, X.; Zhu, Y.; Yang, X.; Zhou, Y.; Yao, Y.; Li, C., Multifunctional Fe3O4@TiO2@Au magnetic microspheres as recyclable substrates for surface-enhanced Raman scattering. *Nanoscale* **2014,** *6* (11), 5971-5979.

67. Sun, L. J.; He, J.; An, S. S.; Zhang, J. W.; Ren, D., Facile one-step synthesis of Ag@Fe3O4 core-shell nanospheres for reproducible SERS substrates. *J Mol Struct* **2013,** *1046*, 74-81.

68. Wang, J.; Wu, X.; Wang, C.; Shao, N.; Dong, P.; Xiao, R.; Wang, S., Magnetically Assisted Surface-Enhanced Raman Spectroscopy for the Detection of Staphylococcus aureus Based on Aptamer Recognition. *ACS Applied Materials & Interfaces* **2015,** *7* (37), 20919-20929.

69. Ge, M.; Wei, C.; Xu, M.; Fang, C.; Yuan, Y.; Gu, R.; Yao, J., Ultra-sensitive magnetic immunoassay of HE4 based on surface enhanced Raman spectroscopy. *Analytical Methods* **2015,** *7* (16), 6489-6495.

70. Ngo, H. T.; Gandra, N.; Fales, A. M.; Taylor, S. M.; Vo-Dinh, T., Sensitive DNA detection and SNP discrimination using ultrabright SERS nanorattles and magnetic beads for malaria diagnostics. *Biosensors and Bioelectronics* **2016,** *81*, 8-14.

71. Guarrotxena, N.; Liu, B.; Fabris, L.; Bazan, G. C., Antitags: Nanostructured Tools for Developing SERS-Based ELISA Analogs. *Advanced Materials* **2010,** *22* (44), 4954-4958.

72. Bhardwaj, V.; Srinivasan, S.; McGoron, A. J., On-chip surface-enhanced Raman spectroscopy (SERS)-linked immuno-sensor assay (SLISA) for rapid environmental-surveillance of chemical toxins. *Advanced Environmental, Chemical, and Biological Sensing Technologies Xii* **2015,** *9486*.

73. Chon, H.; Wang, R.; Lee, S.; Bang, S.-Y.; Lee, H.-S.; Bae, S.-C.; Hong, S. H.; Yoon, Y. H.; Lim, D. W.; Choo, J., Clinical validation of surface-enhanced Raman scattering-based immunoassays in the early diagnosis of rheumatoid arthritis. *Analytical and Bioanalytical Chemistry* **2015,** *407* (27), 8353-8362.

74. Vandenberg, L. N.; Maffini, M. V.; Sonnenschein, C.; Rubin, B. S.; Soto, A. M., Bisphenol-A and the Great Divide: A Review of Controversies in the Field of Endocrine Disruption. *Endocrine Reviews* **2009,** *30* (1), 75-95.

75. Melzer, D.; Osborne, N. J.; Henley, W. E.; Cipelli, R.; Young, A.; Money, C.; McCormack, P.; Luben, R.; Khaw, K. T.; Wareham, N. J.; Galloway, T. S., Urinary bisphenol A concentration and risk of future coronary artery disease in apparently healthy men and women. *Circulation* **2012,** *125* (12), 1482-1490.

76. J, K., *Immunology*. W.H. Freeman: New York, 1997; Vol. 3rd.

77. Barahona, F.; Bardliving, C. L.; Phifer, A.; Bruno, J. G.; Batt, C. A., An aptasensor based on polymer-gold nanoparticle composite microspheres for the detection of malathion using surface-enhanced raman spectroscopy. *Industrial Biotechnology* **2013,** *9* (1), 42-50.

78. Li, M.; Zhang, J. M.; Suri, S.; Sooter, L. J.; Ma, D. L.; Wu, N. Q., Detection of Adenosine Triphosphate with an Aptamer Biosensor Based on Surface-Enhanced Raman Scattering. *Analytical Chemistry* **2012,** *84* (6), 2837-2842.

79. Oh, S.; Kim, M.; Kim, Y.; Jung, H.; Yoon, T. S.; Choi, Y. J.; Kang, C. J.; Moon, M. J.; Jeong, Y. Y.; Park, I. K.; Lee, H. H., Organic memory device with self-assembly monolayered aptamer conjugated nanoparticles. *Appl Phys Lett* **2013,** *103* (8).

80. Pagba, C. V.; Lane, S. M.; Cho, H.; Wachsmann-Hogiu, S., Direct detection of aptamer-thrombin binding via surface-enhanced Raman spectroscopy. *Journal of biomedical optics* **2010,** *15* (4), 047006.

81. Wen, G. Q.; Liang, A. H.; Jiang, Z. L., Functional Nucleic Acid Nanoparticle-Based Resonance Scattering Spectral Probe. *Plasmonics* **2013,** *8* (2), 899-911.

82. Yoon, J.; Choi, N.; Ko, J.; Kim, K.; Lee, S.; Choo, J., Highly sensitive detection of thrombin using SERS-based magnetic aptasensors. *Biosensors & Bioelectronics* **2013,** *47*, 62-67.

83. Yuan, Q.; Lu, D. Q.; Zhang, X. B.; Chen, Z.; Tan, W. H., Aptamer-conjugated optical nanomaterials for bioanalysis. *Trac-Trend Anal Chem* **2012,** *39*, 72-86.

84. Jayasena, S. D., Aptamers: An emerging class of molecules that rival antibodies in diagnostics. *Clinical Chemistry* **1999,** *45* (9), 1628-1650.

85. Chung, E.; Jeon, J.; Yu, J.; Lee, C.; Choo, J., Surface-enhanced Raman scattering aptasensor for ultrasensitive trace analysis of bisphenol A. *Biosensors and Bioelectronics* **2015,** *64*, 560-565.

86. Liu, J., Adsorption of DNA onto gold nanoparticles and graphene oxide: surface science and applications. *Phys Chem Chem Phys* **2012,** *14* (30), 10485-10496.

87. Gupta, P. K.; Brown, J.; Biju, P. G.; Thaden, J.; Deutz, N. E.; Kumar, S.; Hauer-Jensen, M.; Hendrickson, H. P., Development of high-throughput HILIC-MS/MS methodology for plasma citrulline determination in multiple species. *Analytical Methods* **2011,** *3* (8), 1759-1768.

88. Blakely, W. F.; Salter, C. A.; Prasanna, P. G., Early-response biological dosimetry--recommended countermeasure enhancements for mass-casualty radiological incidents and terrorism. *Health Phys* **2005,** *89* (5), 494-504.

89. Budworth, H.; Snijders, A. M.; Marchetti, F.; Mannion, B.; Bhatnagar, S.; Kwoh, E.; Tan, Y.; Wang, S. X.; Blakely, W. F.; Coleman, M.; Peterson, L.; Wyrobek, A. J., DNA Repair and Cell Cycle Biomarkers of Radiation Exposure and Inflammation Stress in Human Blood. *PLoS ONE* **2012,** *7* (11), e48619.

90. Garty, G.; Karam, A.; Brenner, D. J., Infrastructure to support ultra high throughput biodosimetry screening after a radiological event. *International Journal of Radiation Biology* **2011,** *87* (8), 754-765.

91. Joiner, M. C.; Thomas, R. A.; Grever, W. E.; Smolinski, J. M.; Divine, G. W.; Konski, A. A.; Auner, G. W.; Tucker, J. D., Developing point of care and high-throughput biological assays for determining absorbed radiation dose. *Radiotherapy and Oncology* **2011,** *101* (1), 233-236.

92. Brengues, M.; Paap, B.; Bittner, M.; Amundson, S.; Seligmann, B.; Korn, R.; Lenigk, R.; Zenhausern, F., Biodosimetry on small blood volume using gene expression assay. *Health Physics* **2010,** *98* (2), 179-185.

93. Banyan Banyan Biomarkers. http://www.banyanbio.com/index.php (accessed July 30, 2010).

94. Teasdale, G., Assessment of Coma and Impaired Consciousness: A Practical Scale. *The Lancet* **1974,** *304* (7872), 81-84.

95. Gupta, A. K., *Notes in Neuroanaesthesia and Critical Care*. Greenwich Medical Media LTD: London, 2001.

96. Wilson, J. T. L., Structured Interviews for the Glasgow Outcome Scale and the Extended Glasgow Outcome Scale: Guidelines for Their Use. *Journal of Neurotrauma* **1998,** *15*, 573- 585.

97. Benford, M. E. Development of a Surface Enhanced Raman Spectroscopy Platform Technology to Detect Cardiac Biomarkers of Myocardial Infarction. Texas A&M, College Station, Tx, 2013.

98. Wang, M.; Benford, M.; Jing, N.; Coté, G.; Kameoka, J., Optofluidic device for ultra-sensitive detection of proteins using surface-enhanced Raman spectroscopy. *Microfluidics and Nanofluidics* **2009,** *6* (3), 411-417.

99. Januzzi, J. L., *Cardiac Biomarkers in Clinical Practice*. Jones & Bartlett Learning: 2010.

100. Wu, A. H. B., *Cardiac Markers*. Humana Press: 2003.

101. Patel, M. R.; Chen, A. Y.; Peterson, E. D.; Newby, L. K.; Pollack Jr, C. V.; Brindis, R. G.; Gibson, C. M.; Kleiman, N. S.; Saucedo, J. F.; Bhatt, D. L.; Gibler, W. B.; Ohman, E. M.; Harrington, R. A.; Roe, M. T., Prevalence, predictors, and outcomes of patients with non-ST-segment elevation myocardial infarction and insignificant coronary artery disease: Results from the Can Rapid risk stratification of Unstable angina patients Suppress ADverse outcomes with Early implementation of the ACC/AHA Guidelines (CRUSADE) initiative. *American Heart Journal* **2006,** *152* (4), 641-647.

102. Baaske, P.; Wienken, C. J.; Reineck, P.; Duhr, S.; Braun, D., Optical thermophoresis for quantifying the buffer dependence of aptamer binding. *Angewandte Chemie International Edition* **2010,** *49* (12), 2238-2241.

103. Morris M, B. P., Langst G, Jackson GW In *Binding analytics of DNA aptamers to small molecules determined by microscale thermophoresis (MST).* Southwest Regional Meeting of the American Chemical Society, Baton Rouge, LA, Baton Rouge, LA, 2012.

104. Faulds, K.; Jarvis, R.; Smith, W. E.; Graham, D.; Goodacre, R., Multiplexed detection of six labelled oligonucleotides using surface enhanced resonance Raman scattering (SERRS). *Analyst* **2008,** *133* (11), 1505-1512.

105. Gellner, M.; Kompe, K.; Schlucker, S., Multiplexing with SERS labels using mixed SAMs of Raman reporter molecules. *Analytical and Bioanalytical Chemistry* **2009,** *394* (7), 1839-1844.

106. Jadzinsky, P. D.; Calero, G.; Ackerson, C. J.; Bushnell, D. A.; Kornberg, R. D., Structure of a thiol monolayer-protected gold nanoparticle at 1.1 angstrom resolution. *Science* **2007,** *318* (5849), 430-433.

107. Love, J. C.; Estroff, L. A.; Kriebel, J. K.; Nuzzo, R. G.; Whitesides, G. M., Self-assembled monolayers of thiolates on metals as a form of nanotechnology. *Chem Rev* **2005,** *105* (4), 1103-1169.

108. Barriet, D.; Yam, C. M.; Shmakova, O. E.; Jamison, A. C.; Lee, T. R., 4-mercaptophenylboronic acid SAMs on gold: Comparison with SAMs derived from thiophenol, 4-mercaptophenol, and 4-mereaptobenzoic acid. *Langmuir* **2007,** *23* (17), 8866-8875.

109. Orendorff, C. J.; Gole, A.; Sau, T. K.; Murphy, C. J., Surface-enhanced Raman spectroscopy of self-assembled monolayers: Sandwich architecture and nanoparticle shape dependence. *Analytical Chemistry* **2005,** *77* (10), 3261-3266.

110. Zhou, J.; Ralston, J.; Sedev, R.; Beattie, D. A., Functionalized gold nanoparticles: Synthesis, structure and colloid stability. *J Colloid Interf Sci* **2009,** *331* (2), 251-262.

111. Ulman, A., Formation and structure of self-assembled monolayers. *Chem Rev* **1996,** *96* (4), 1533-1554.

112. Zhang, H.; He, H. X.; Wang, J.; Liu, Z. F., Atomic force microscopy evidence of citrate displacement by 4-mercaptopyridine on gold in aqueous solution. *Langmuir* **2000,** *16* (10), 4554-4557.

113. Jana, N. R.; Ying, J. Y., Synthesis of Functionalized Au Nanoparticles for Protein Detection. *Advanced Materials* **2008,** *20* (3), 430-434.

114. Jokerst, J. V.; Lobovkina, T.; Zare, R. N.; Gambhir, S. S., Nanoparticle PEGylation for imaging and therapy. *Nanomedicine* **2011,** *6* (4), 715-728.

115. McKenzie, F.; Ingram, A.; Stokes, R.; Graham, D., SERRS coded nanoparticles for biomolecular labelling with wavelength-tunable discrimination. *Analyst* **2009,** *134* (3), 549-556.

116. Moran, C. H.; Rycenga, M.; Zhang, Q.; Xia, Y. N., Replacement of Poly(vinyl pyrrolidone) by Thiols: A Systematic Study of Ag Nanocube Functionalization by Surface-Enhanced Raman Scattering. *Journal of Physical Chemistry C* **2011,** *115* (44), 21852-21857.

117. Papp, S.; Patakfalvi, R.; Dekany, I., Formation and stabilization of noble metal nanoparticles. *Croat Chem Acta* **2007,** *80* (3-4), 493-502.

118. Israelachvili, J., *Intermolecular and Surface Forces, Third Edition*. Academic Press: 2010.

119. Marimuthu, A.; Christopher, P.; Linic, S., Design of plasmonic platforms for selective molecular sensing based on surface-enhanced Raman spectroscopy. *Journal of Physical Chemistry C* **2012,** *116* (17), 9824-9829.

120. Varsányi, G.; Láng, L.; Kovner, M. A., *Assignments for Vibrational Spectra of Seven Hundred Benzene Derivatives*. Institute of Physics Publishing: 1974.

121. Ma, W. Q.; Fang, Y.; Hao, G. L.; Wang, W. G., Adsorption behaviors of 4-mercaptobenzoic acid on silver and gold films. *Chinese Journal of Chemical Physics* **2010,** *23* (6), 659-663.

122. Wells, M.; Dermody, D. L.; Yang, H. C.; Kim, T.; Crooks, R. M.; Ricco, A. J., Interactions between organized, surface-confined monolayers and vapor-phase probe molecules: Structure/reactivity relationship between three surface-confined isomers of mercaptobenzoic acid and vapor-phase decylamine. *Langmuir* **1996,** *12* (8), 1989-1996.

123. Michota, A.; Bukowska, J., Surface-enhanced Raman scattering (SERS) of 4-mercaptobenzoic acid on silver and gold substrates. *Journal of Raman Spectroscopy* **2003,** *34* (1), 21-25.

124. Jo, M.; Ahn, J. Y.; Lee, J.; Lee, S.; Hong, S. W.; Yoo, J. W.; Kang, J.; Dua, P.; Lee, D. K.; Hong, S.; Kim, S., Development of single-stranded DNA aptamers for specific bisphenol a detection. *Oligonucleotides* **2011,** *21* (2), 85-91.

125. Jasse, B.; Chao, R. S.; Koenig, J. L., Laser Raman scattering in uniaxially oriented atactic polystyrene. *Journal of Polymer Science: Polymer Physics Edition* **1978,** *16* (12), 2157-2169.

126. Sears, W. M.; Hunt, J. L.; Stevens, J. R., Raman scattering from polymerizing styrene. I. Vibrational mode analysis. *The Journal of Chemical Physics* **1981,** *75* (4), 1589-1598.

127. Anema, J. R.; Brolo, A. G.; Felten, A.; Bittencourt, C., Surface-enhanced Raman scattering from polystyrene on gold clusters. *Journal of Raman Spectroscopy* **2010,** *41* (7), 745-751.

128. Markham, D. A.; Waechter, J. M., Jr.; Wimber, M.; Rao, N.; Connolly, P.; Chuang, J. C.; Hentges, S.; Shiotsuka, R. N.; Dimond, S.; Chappelle, A. H., Development of a method for the determination of bisphenol A at trace concentrations in human blood and urine and elucidation of factors influencing method accuracy and sensitivity. *Journal of Analytical Toxicology* **2010,** *34* (6), 293-303.

129. Völkel, W.; Bittner, N.; Dekant, W., Quantitation of bisphenol A and bisphenol A glucuronide in biological samples by high performance liquid chromatography-tandem mass spectrometry. *Drug Metabolism and Disposition* **2005,** *33* (11), 1748-1757.

130. Moreno, M. J.; D'Arienzo, P.; ManclúS, J. J.; Montoya, A., Development of monoclonal antibody-based immunoassays for the analysis of bisphenol A in canned vegetables. *Journal of Environmental Science and Health - Part B Pesticides, Food Contaminants, and Agricultural Wastes* **2011,** *46* (6), 509-517.

131. Graham, D.; Stevenson, R.; Thompson, D. G.; Barrett, L.; Dalton, C.; Faulds, K., Combining functionalised nanoparticles and SERS for the detection of DNA relating to disease. *Faraday Discuss* **2011,** *149*, 291-9; discussion 333-56.

132. Guerrini, L.; Graham, D., Molecularly-mediated assemblies of plasmonic nanoparticles for Surface-Enhanced Raman Spectroscopy applications. *Chemical Society Reviews* **2012,** *41* (21), 7085-7107.

133. Qu, G.; Zhang, G.; Wu, Z.; Shen, A.; Wang, J.; Hu, J., A "turn-off" SERS assay of heparin with high selectivity based on heparin-peptide complex and Raman labelled gold nanoparticles. *Biosensors & bioelectronics* **2014,** *60*, 124-9.

134. Wu, Z.; Liu, Y.; Zhou, X.; Shen, A.; Hu, J., A "turn-off" SERS-based detection platform for ultrasensitive detection of thrombin based on enzymatic assays. *Biosensors & bioelectronics* **2013,** *44*, 10-5.

135. Moghaddam, A.; Løbersli, I.; Gebhardt, K.; Braunagel, M.; Marvik, O. J., Selection and characterisation of recombinant single-chain antibodies to the hapten Aflatoxin-B1 from naive recombinant antibody libraries. *Journal of Immunological Methods* **2001,** *254* (1-2), 169-181.

136. Donnelly, T.; Smith, W. E.; Faulds, K.; Graham, D., Silver and magnetic nanoparticles for sensitive DNA detection by SERS. *Chemical Communications* **2014**.

137. Kumar, G.; Rangarajan, N.; Sonia, B.; Deepika, P.; Rohman, N.; Narayana, C., Metal-coated magnetic nanoparticles for surface enhanced Raman scattering studies. *Bull Mater Sci* **2011,** *34* (2), 207-216.

138. Mandal, M.; Kundu, S.; Ghosh, S. K.; Panigrahi, S.; Sau, T. K.; Yusuf, S. M.; Pal, T., Magnetite nanoparticles with tunable gold or silver shell. *J Colloid Interf Sci* **2005,** *286* (1), 187-194.

139. Leopold, N.; Lendl, B., A new method for fast preparation of highly surface-enhanced Raman scattering (SERS) active silver colloids at room temperature by reduction of silver nitrate with hydroxylamine hydrochloride. *The Journal of Physical Chemistry B* **2003,** *107* (24), 5723-5727.

140. Yguerabide, J.; Yguerabide, E. E., Light-Scattering Submicroscopic Particles as Highly Fluorescent Analogs and Their Use as Tracer Labels in Clinical and Biological Applications: I. Theory. *Analytical Biochemistry* **1998,** *262* (2), 137-156.

141. Zhang, X.; Servos, M. R.; Liu, J., Fast pH-assisted functionalization of silver nanoparticles with monothiolated DNA. *Chem. Commun.* **2012,** *48* (81), 10114-10116.

142. Power, A. C.; Betts, A. J.; Cassidy, J. F., Non aggregated colloidal silver nanoparticles for surface enhanced resonance Raman spectroscopy. *Analyst* **2011,** *136* (13), 2794-2801.

143. Rezg, R.; El-Fazaa, S.; Gharbi, N.; Mornagui, B., Bisphenol A and human chronic diseases: Current evidences, possible mechanisms, and future perspectives. *Environment International* **2014,** *64*, 83-90.

144. Gao, R.; Ko, J.; Cha, K.; Jeon, J. H.; Rhie, G.-e.; Choi, J.; Choo, J., Fast and sensitive detection of an anthrax biomarker using SERS-based solenoid microfluidic sensor. *Biosensors and Bioelectronics* **2015,** *72*, 230-236.

145. Han, B.; Choi, N.; Kim, K. H.; Lim, D. W.; Choo, J., Application of Silver-Coated Magnetic Microspheres to a SERS-Based Optofluidic Sensor. *Journal of Physical Chemistry C* **2011,** *115* (14), 6290-6296.

146. Park, H. Y.; Schadt, M. J.; Wang, L.; Lim, I. I. S.; Njoki, P. N.; Kim, S. H.; Jang, M. Y.; Luo, J.; Zhong, C. J., Fabrication of magnetic core @ shell Fe oxide @ Au nanoparticles for interfacial bioactivity and bio-separation. *Langmuir* **2007,** *23* (17), 9050-9056.

147. Carroll, K. J.; Glaspell, G. P.; McDowall, N.; Brown Iii, L. W.; Zhang, K.; Pradhan, A. K.; Anderson, J.; Carpenter, E. E. In *Surface enhanced Raman utilizing magnetic core gold shell nanoparticles*, Nanotech 2010, NSTI, Ed. 2010; pp 395-398.

148. Guven, B.; Basaran-Akgul, N.; Temur, E.; Tamer, U.; Boyaci, I. H., SERS-based sandwich immunoassay using antibody coated magnetic nanoparticles for Escherichia coli enumeration. *Analyst* **2011,** *136* (4), 740-748.

149. Do, J.; Choi, J. W.; Ahn, C. H., Low-cost magnetic interdigitated array on a plastic wafer. *IEEE Transactions on Magnetics* **2004,** *40* (4 II), 3009-3011.

150. Granger, J. H.; Schlotter, N. E.; Crawford, A. C.; Porter, M. D., Prospects for point-of-care pathogen diagnostics using surface-enhanced Raman scattering (SERS). *Chemical Society Reviews* **2016**.

151. Lueck, H. B.; Daniel, D. C.; McHale, J. L., Resonance Raman study of solvent effects on a series of triarylmethane dyes. *Journal of Raman spectroscopy* **1993,** *24* (6), 363-370.

152. Huang, N.; Short, M.; Zhao, J.; Wang, H.; Lui, H.; Korbelik, M.; Zeng, H., Full range characterization of the Raman spectra of organs in a murine model. *Opt. Express* **2011,** *19* (23), 22892-22909.

153. Malini, R.; Venkatakrishna, K.; Kurien, J.; M. Pai, K.; Rao, L.; Kartha, V. B.; Krishna, C. M., Discrimination of normal, inflammatory, premalignant, and malignant oral tissue: A Raman spectroscopy study. *Biopolymers* **2006,** *81* (3), 179-193.

154. Maier, J. S.; Treado, P. J.; Cohen, J.; Neiss, J. Digitizing biology. 2007.

155. Feng, S.; Huang, S.; Lin, D.; Chen, G.; Xu, Y.; Li, Y.; Huang, Z.; Pan, J.; Chen, R.; Zeng, H., Surface-enhanced Raman spectroscopy of saliva proteins for the noninvasive differentiation of benign and malignant breast tumors. *International journal of nanomedicine* **2015,** *10*, 537.

156. He, J.; Li, G.; Hu, Y., Aptamer recognition induced target-bridged strategy for proteins detection based on magnetic chitosan and silver/chitosan nanoparticles using surface-enhanced Raman spectroscopy. *Analytical Chemistry* **2015,** *87* (21), 11039-11047.

157. Heydari, E.; Thompson, D.; Graham, D.; Cooper, J. M.; Clark, A. W. In *An engineered nano-plasmonic biosensing surface for colorimetric and SERS detection of DNA-hybridization events*, SPIE Bios, International Society for Optics and Photonics

2015; pp 93400O-93400O-6.

158. Krpetić, Ž.; Guerrini, L.; Larmour, I. A.; Reglinski, J.; Faulds, K.; Graham, D., Importance of nanoparticle size in colorimetric and SERS-based multimodal trace detection of Ni(II) ions with functional gold nanoparticles. *Small* **2012,** *8* (5), 707-714.

159. Jang, H.; Hwang, E. Y.; Kim, Y.; Choo, J.; Jeong, J.; Lim, D. W., Surface-Enhanced Raman Scattering and Fluorescence-Based Dual Nanoprobes for Multiplexed Detection of Bacterial Pathogens. *Journal of Biomedical Nanotechnology* **2016,** *12* (10), 1938-1951.